

**LIGHT-MATTER INTERACTION FROM ATOMISTIC  
RARE-EARTH CENTERS IN SOLIDS TO MASSIVE  
LEVITATED OBJECTS**

by

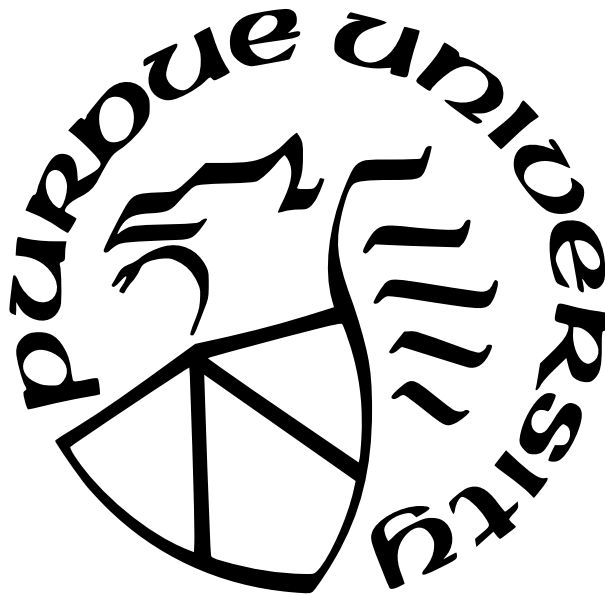
**Xiaodong Jiang**

**A Dissertation**

*Submitted to the Faculty of Purdue University*

*In Partial Fulfillment of the Requirements for the degree of*

**Doctor of Philosophy**



School of Electrical and Computer Engineering

West Lafayette, Indiana

May 2022

**THE PURDUE UNIVERSITY GRADUATE SCHOOL  
STATEMENT OF COMMITTEE APPROVAL**

**Dr. Mahdi Hosseini, Chair**

School of Electrical and Computer Engineering

**Dr. Tongcang Li**

Department of Physics and Astronomy

School of Electrical and Computer Engineering

**Dr. Pramey Upadhyaya**

School of Electrical and Computer Engineering

**Dr. Hadiseh Alaeian**

School of Electrical and Computer Engineering

Department of Physics and Astronomy

**Approved by:**

Dr. Dimitrios Peroulis



## ACKNOWLEDGMENTS

I am deeply thankful to the people who have helped and supported me along the journey of my Ph.D.. I started my PhD in Prof. Mahdi Hosseini's lab which was just built by the time I joined. A lot of new equipment needed to be set up and different ideas were waiting to be implemented.

First and foremost, I would like to express my special thanks to Dr. Mahdi Hosseini, my PhD advisor, I could not really ask for better advisors than you. Every time I knocked on your door and asked for your help and support because of the difficulties in my research projects, you were always available and patient to explain the scientific theories in simple words. You are not only my supervisor but also my life mentor and a wonderful friend. Your broad knowledge and wisdom in science made me inspired to be an independent researcher. I also thank you for the books that you recommended, they are very helpful to improve my reading and writing skills. There are no words that can exactly express my gratitude for what you have done for me, but I just want to let you know how grateful I am to you.

I would also like to thank all of my lab mates, Dongmin Pak, Arindam Nandi, and Haechan An for all of your help, discussions, and support, which made my research and life at Purdue a wonderful time. I also thank Sami Alajlouni for lending me the cryogenic experimental tool. Many thanks to my committee members Dr. Mahdi Hosseini, Dr. Tongcang Li, Dr. Pramey Upadhyaya, and Dr. Hadiseh Alaeian for their great and insightful advice and comments on my thesis. I also appreciate all the Birck staff for maintaining Birck Nanotechnology Center as an amazing place to accomplish my PhD research projects. And lastly, my appreciation also goes out to the funding support from Purdue, NSF, and AFOSR.

I want to give my sincere and deep gratitude to my parents for their tremendous support and unconditional love throughout my Ph.D.. I also want to give my genuine thanks to my fiancée, Yusong Jin, for her love, understanding, never-ending support, and encouragement. Without your companion, my life would be much different.

# TABLE OF CONTENTS

LIST OF TABLES . . . . .	8
LIST OF FIGURES . . . . .	9
ABSTRACT . . . . .	14
1 INTRODUCTION AND MOTIVATION . . . . .	16
1.1 Light-matter Interaction for Coherent Light Storage . . . . .	17
1.1.1 Coherent Light Storage in Atoms . . . . .	17
1.1.2 Coherent Light Storage with Optomechanics . . . . .	20
1.1.3 Integrated Solid-state Photonics . . . . .	22
1.2 Light-matter Interaction for Sensing . . . . .	23
1.2.1 Superconducting Levitation . . . . .	24
1.2.2 Trapping and Noise in Superconducting Levitation . . . . .	26
Thermal Noise . . . . .	26
Gas Collisions . . . . .	26
Seismic Noise . . . . .	27
Noise from Eddy Currents . . . . .	27
Noise from Magnetic Hysteretic Losses . . . . .	28
Mode Coupling . . . . .	28
Nonlinear Dissipation . . . . .	29

2	RARE-EARTH IONS SCALABLE INTEGRATION WITH SILICON PHOTONICS USING LITHIUM NIOBATE HOST . . . . .	31
2.1	Introduction . . . . .	31
2.2	Implantation of Er and Yb Ions into Lithium Niobate Crystals . . . . .	32
2.3	Optical Characterization of Yb-implanted Bulk LN Crystals . . . . .	34
2.4	Fabrication of Si and SiN Finger-type Microresonators . . . . .	36
2.5	Inregration of Er-implanted LN Crystal with Si-SiN Microresonators . . . . .	37
2.6	Optical Characterization of Integrated Er:LN-Si-SiN Photonic Device . . . . .	39
2.7	Summary . . . . .	43
3	OPTOMECHANICAL FREQUENCY COMB FOR LIGHT STORAGE . . . . .	44
3.1	Introduction . . . . .	44
3.2	Optomechanical Interaction in a Cavity . . . . .	45
3.3	Optomechanical Frequency Comb for Storing Light Information . . . . .	52
3.4	Merit of Proposed Optomechanical Memory System . . . . .	58
3.5	Potential Realization of Proposed Optomechanical Comb Memory . . . . .	59
3.6	Summary . . . . .	59
4	SUPERCONDUCTING LEVITATION OF A MG-SCALE CAVITY MIRROR . . . . .	61
4.1	Introduction . . . . .	61
4.2	Hybrid Superconductor Levitation Platform . . . . .	62
4.3	Theoretical Calculation of Superconductor Levitation based on Frozen-image Model . . . . .	62

4.4	Experimental Characterization of Superconductor-levitated Mirror . . . . .	66
4.5	AC Magnetic Field Sensing Using Levitation Mirror . . . . .	68
4.6	Fabry-Pérot Cavity Built Based on Superconducting Levitated Mirror . . . .	71
4.7	Summary . . . . .	74
5	DRIVEN NONLINEAR DAMPING AND MODE COUPLING IN A SUPERCONDUCTING LEVITATED MAGNET . . . . .	76
5.1	Introduction . . . . .	76
5.2	Theoretical Calculation of Vibrational Modes of Levitated Magnetic Mirror .	77
5.3	Experimental Setup and Measurement . . . . .	80
5.4	Displacement Noise Calibration of Levitated Magnetic Mirror . . . . .	81
5.5	Vibrational Spectra Comparison between Experimental and Theoretical Calculation . . . . .	84
5.6	Superconducting Levitated Magnetic Mirror as a Duffing Resonator . . . . .	86
5.7	Magnetic Inhomogeneity of Levitated Magnetic Mirror . . . . .	86
5.8	Effect of Magnetic Mirror's Orientation . . . . .	89
5.9	Quality Factor (Q) Measurement . . . . .	90
5.10	Nonlinear Energy Dissipation . . . . .	93
5.11	Cooling Theory . . . . .	94
5.12	Vibrational Noise Reduction Caused by Nonlinear Damping and mode Coupling	98
5.13	Potential Application for Superconducting levitated HR mirror . . . . .	102
5.14	Summary . . . . .	105

6	SUMMARY AND FUTURE WORK . . . . .	107
6.1	Current Work Summary . . . . .	107
6.1.1	On-chip Integration of Er-implanted Lithium Niobate Crystal with Silicon Photonics . . . . .	107
6.1.2	Optomechanical Frequency Comb Memory . . . . .	108
6.1.3	Superconducting Levitation of a mg-Scale Cavity Mirror . . . . .	108
6.1.4	Driven Nonlinear Damping and Mode Coupling in a Superconducting Levitated Magnetic Mirror . . . . .	109
6.2	Future Work Plan . . . . .	110
6.2.1	Reducing Vibrational Noise of Superconducting Levitated Magnetic Mirror . . . . .	110
6.2.2	Applying Passive and Active Cooling Methods to Improve Sensitivity	111
6.2.3	Building a Cavity Based on Superconducting Levitated Mirror to Im- prove Sensitivity . . . . .	111
6.2.4	Toward Precision Sensing Gravity with Levitated Mirror . . . . .	112
	REFERENCES . . . . .	114
	PUBLICATIONS . . . . .	134

## LIST OF TABLES

- 4.1 Comparison of different magnetometers. SQUID: superconducting quantum interference device; SERF: spin-exchange relaxation-free atomic magnetometers; NV Center: nitrogen-vacancy center; MEMS: micro-electromechanical systems. . 70

## LIST OF FIGURES

1.1	AFC quantum memory principles. Shaped inhomogeneous broadening by selectively pumping the atoms from ground state $ g\rangle$ to the metastable state $ aux\rangle$ . The linewidth of each frequency peak in AFC is $\gamma$ and the neighboring peaks are spaced by $\Delta$ . The input mode is fully absorbed and excites the AFC modes coherently. One control field is used to transfer the stored coherent information to the spin state $ s\rangle$ and the other is applied to convert the spin state information back into optical coherence. . . . .	19
2.1	(a) Er ions' distribution in Er-implanted LN crystals based on the SRIM calculation. (b) Er ions' distribution in Er-implanted LN crystals based on the SRIM calculation. The two insets show the schematic energy level diagrams of Yb and Er ions in LN crystals, respectively. . . . .	33
2.2	(a) Experimental setup of detecting PL emission from an ensemble of Yb and Er ions implanted in LN crystals. (b) Excitation and collection through a lensed fiber and the angle of the fiber is altered while photoluminescence decay is recorded . . . . .	34
2.3	(a) The photoluminescence lifetime (red circle) and peak intensity (dark-purple rectangle) as a function of the collection angle of the lensed fiber from the axis normal to the sheet of implanted Yb ions in the LN crystal at room temperature (300 K). The blue data points show the decay time measurement at 4 K. (b) The photoluminescence spectrum of Yb ions implanted in the LN crystal plotted with the increasing pump powers from 20 mW (bottom blue line) to 140 mW (top red line) where a different intensity offset is used for each pump power. . . . .	35
2.4	The scanning electron microscopy (SEM) image of the U-groove and the top-view optical microscopy image of Si-SiN waveguides and finger-type resonators. . . . .	36
2.5	(a) The cross-sectional view of the Er:LN crystal integrated with Si-SiN waveguides and resonators. (b) Comsol simulation of the optical mode in the cross section of the structure showing enhanced mode confinement at 1.5 $\mu$ m in the 50 nm thick Si layer near the crystal. . . . .	38
2.6	(a) A schematic of the device showing the Er:LN crystal directly integrated with Si-SiN waveguides and resonators. A simplified layout of the experimental setup is also shown on the left used to detect the emission photons from Er ions in the LN crystal through the Si-SiN waveguide. SPD: single photon detector; D.M.: dichroic mirror (b) Top-view optical microscopy image of Si-SiN finger-shape resonators directly bonded to the Er:LN crystal (c) The transmission of 1550 nm (dark-red curve) and 980 nm (blue curve) light coupled into the middle resonator of the integrated Er:LN-Si-SiN device. The light-blue curve shows the transmission of the middle resonator at 1536 nm before integrating Er:LN crystal with this resonator. . . . .	40

2.7	(a) PL decays of Er ions from the integrated Er:LN-Si-SiN device compared to the Er:LN bulk crystal through evanescent coupling. (b) Cavity transmission signal for two different free spectral ranges (FSRs) of the cavity at 1520 nm and 1540 nm. (c) The total PL counts after the pump is switched off and PL lifetime as a function of frequency detuning of the pump from an optical cavity resonance near 980 nm. The solid line is Lorentzian functions with the linewidth of 17 GHz. (d) The linewidth of the cavity at different FSRs near 1.5 $\mu\text{m}$ for the hybrid finger-type resonator of integrated Er:LN-Si-SiN device.	41
3.1	Broadband data pulse (probe) and “read” and “write” control pulses with multiple frequency comb lines, as depicted in (a), create a controllable optomechanical frequency comb. The interaction scheme and equivalent energy level structure are depicted in (b) for the optomechanical system. (c) Optomechanical interaction between a broadband input pulse and the mechanical oscillators in an array is tailored by the control pulses. . . . .	46
3.2	Amplitude of the optical ( $A_{opt}$ ) and mechanical ( $A_{mech}$ ) excitations are plotted as a function of the normalized time. A probe pulse (black curve) impinging on the cavity together with a write laser create mechanical excitations that echo after a time of $2\pi/\Delta$ . The photon-phonon echo intensities from the subset of ensemble with mechanical oscillators as low as eleven (solid purple), seven (solid green) and five (solid red) are shown (left axis). The corresponding collective mechanical excitations are indicated with dashed lines (right axis). A normalized optomechanical coupling rate of $g_0^2/\kappa\gamma_m = 10^{-3}$ , thermalization rate $\gamma_m/\kappa = 0.001$ , mechanical dephasing/rephasing rate $\Delta/\kappa = 0.05$ , center mechanical resonant frequency $\omega_m/\kappa = 10$ , and the total number of mechanical oscillators $M = 100$ are used in this simulation. . . . .	53
3.3	The storage efficiency (open circle) and the signal-to-noise ratio (filled circle) of the optomechanical array memory as a function of (a) the normalized center frequency ( $\omega_m$ ) of the mechanical excitations as $m_s = 11$ , (b) the control cooperativity, $C_c = 4g_0^2 n_c / \kappa \gamma_m$ , where $n_c$ is varied, for inhomogenous broadening $\Delta\omega = 1\% \omega_m$ (open circle) and $\Delta\omega = 0.5\% \omega_m$ (open square) as $m_s = 11$ , (c) the number of mechanical oscillators ( $m_s$ ), which are addressed by the control field out of $M = 100$ total oscillators, and have frequency spacing of $\Delta = 0.05\kappa$ , and (d) the storage efficiency as a function of the normalized optomechanical spectral width $\Delta\omega_m/\omega_m$ and frequency spacing $\Delta/\kappa$ of the tailored optomechanical spectrum, where $m_s = 11$ and $C_c = 0.4$ are used for the simulation while the other parameters are the same as the ones used in Fig. 3.2 . . . . .	55



4.1	Experimental setup for a cavity mirror magnetically levitated and optically probed. The vibration of a magnetic mirror levitated above a superconductor (SC) disk is monitored using a quadrant detector (quad. det.). Also, the levitated mirror together with the fixed HR mirror (reflectivity of $\sim 98\%$ and radius of 25cm) form an optical cavity. The current controller controls AC and DC current in the coil down to a few hundreds of $nA$ in order to calibrate the response of the mirror to the external magnetic field. . . . .	63
4.2	The model describes the frozen and diamagnetic images based on the interaction between the levitated magnetic mirror and the SC disk, which is used to calculate the mechanical modes. . . . .	64
4.3	The calculated values of resonant frequencies of the levitated mirror . . . .	66
4.4	The vibration spectra of the levitated mirror captured by the quadrant detector by subtracting the left-right (horizontal) or top-bottom (vertical) pixels. At a deflection angle of about $45^\circ$ the calculated values of frequencies approximately match the measured values indicated by the shaded regions on the spectrum plot. . . . .	68
4.5	The peak vibrational intensity (normalized to the background noise) or signal to noise ration (SNR) is plotted at different applied modulation frequencies. Inset shows the measured peak vibrational intensity normalized to the electronic noise (i.e., SNR) as a function of the applied magnetic field for the modulation frequency of $f \simeq 90\text{Hz}$ . . . . .	69
4.6	Theoretical calculation of trapping frequency ( $f_y = f_{trap}$ ), optical stiffness and trapping potential ( $U_{trap}$ in the inset) for a mirror of mass 30mg and cavity of finesse (input power) of 400 (0.25W). . . . .	72
4.7	Intensity of the reflected light from the fixed cavity mirror as a function of the experiment time and the displacement along the cavity axis (y axis). Inset shows the signal close up in a shorter time window (dashed box). . . . .	73
5.1	Frozen image model diagram. . . . .	77
5.2	Experimental setup for a magnetic mirror (a magnetic ring attached to a dielectric mirror) levitated above a superconductor disk and optically probed in vacuum conditions ( $10^{-8}$ Torr). A coil with excitation current, $I_{exc}$ , can excite and drive the levitated magnet. . . . .	80
5.4	The setup for calibrating the displacement of the levitated magnetic mirror using the piezoelectric transducer. $V_+ - V_-$ is the driving voltage applied to the transducer. . . . .	83
5.5	Calibration of displacement of the levitated magnetic mirror using the piezoelectric transducer . . . . .	83

5.6	(a) The quadrant photodetector sensitivity $S_x$ and $S_y$ as a function of the radio of light spot radius ( $w$ ) and quadrant detector radius ( $R$ ) [205]. (b) The displacement noise spectrum measured for the magnetic levitated mirror . . .	84
5.7	The theoretical (blue) and experimental (red) vibrational noise spectra of the levitated magnetic mirror. The modes whose resonances could be observed (shaded green areas) match theoretical predictions within 10%. The theoretical spectrum is plotted with an arbitrary offset and excitation. . . . .	85
5.8	(a) Nonlinear frequency response of oscillation along $z$ axis at different modulation frequencies near $\omega_z$ . The black curve shows the fitting result using Duffing equation. (b) Ring down measurement of pulsed-resonant excitation at $\omega_z$ shows an asymmetric oscillation with respect to the zero axis, which is caused by the related asymmetric trapping potential . . . . .	87
5.9	Calibration of magnetic fluctuation along $z$ axis, $\delta B$ . . . . .	88
5.10	Observation of multi-mode cooling at different magnetic modulation voltages (proportional to $\Delta B$ ) introduced by the driving coil at $\omega_z = 90\text{Hz}$ . The vibrational spectra are vertically shifted for different modulation amplitudes for clarity. Simultaneous cooling of modes at 148Hz and 164Hz can be seen.	90
5.11	Noise power spectrum measured with resolution bandwidth of 0.001 Hz. . . .	91
5.12	(a) Spectrum of the high-Q coupled mode $\omega_{v(x,\theta)}$ measured with a resolution bandwidth of 0.001Hz. (b) The fitted linewidth as a function of the external modulation frequency with a constant modulation amplitude $\Delta B = 28\mu\text{T}$ shows the effect of external excitation on mechanical Q. The dotted line here is a guide to the eye. . . . .	92
5.13	The calculated static dissipated energy per unit volume ( $\delta E_0$ ) as a function of magnetic field fluctuation ( $\delta B$ ) induced by the magnetic mirror oscillating along the $z$ axis. Inset shows the calculated mechanical linewidth at $\omega_z$ for different values of $\eta$ . . . . .	93
5.14	(a) and (b) Cooling of mechanical vibrations at $\omega_{q(y,\alpha)} \simeq 138\text{Hz}$ , via resonant excitation of $\omega_z$ and $\omega_{u(x,\theta)}$ modes, respectively. Inset shows the cooled modes when different magnetic excitation amplitudes ( $\Delta B$ ) are applied. (c) The normalized vibrational intensity noise of $\omega_{q(y,\alpha)}$ as a function of modulation frequency for the fixed $\Delta B = 56\mu\text{T}$ applied to the driving coil. The dotted line is a guide to the eye. . . . .	98
5.15	Observation of multi-mode cooling at different magnetic modulation voltages (proportional to $\Delta B$ ) introduced by the driving coil at $\omega_z = 90\text{Hz}$ . The vibrational spectra are vertically shifted for different modulation amplitudes for clarity. Simultaneous cooling of modes at 148Hz and 164Hz can be seen.	99

- 5.16 (a) The vibrational spectrum with heating and cooling modes indicated at  $\omega_z$  and  $\omega_{q(y,\alpha)}$ , respectively. Inset shows the cooling mode ( $\omega_{q(y,\alpha)}$ ) for different external magnetic modulation amplitudes ( $\Delta B$ ) induced by the current modulation in the coil. (b) The measured linewidth of  $\omega_{q(y,\alpha)}$  mode as a function of  $\Delta B$ . The inset shows the normalized noise power of  $\omega_{q(y,\alpha)}$  mode as a function of  $\Delta B$ . The line in the inset is a guide to the eye. . . . . 101
- 5.17 Schematics of coherent levitation of a mirror on an optical spring self-locked to the laser frequency. A combination of magneto-optical levitation, laser cooling and cavity restoring force creates a scattering-free tweezer for the mirror. A micro-disk mirror with magnetic coating is trapped in x-y directions using a superconducting disk while optical force of an intra-cavity field coherently traps the mirror in the  $z$  direction. . . . . 104

# ABSTRACT

A harmonic oscillator is a ubiquitous tool in various disciplines of engineering and physics for sensing and energy transduction. The degrees of freedom, low noise oscillation, and efficient input-output coupling are important metrics when designing sensors and transducers using such oscillators. The ultimate examples of such oscillators are quantum mechanical oscillators coherently transducing information or energy. Atoms are oscillators whose degrees of freedom can be controlled and probed coherently by means of light. Elegant techniques developed during the last few decades have enabled us to use atoms, for example, to build exquisite quantum sensors such as clocks with the precision of  $<1$  second error over the lifetime of the universe, to store and transduce information of various forms and also to develop quantum processors. Similar to atoms, mechanical oscillators can also be controlled ultimately to their single vibrational quanta and be used for similar sensing and transduction applications.

In this thesis, we explore both atomic and mechanical systems and develop a toolbox to build an effective atom-light interface and light-oscillator interface for controlling such atomic and mechanical oscillators and use them in sensing and storage applications. Primarily, we study two disparate platforms: 1) rare-earth ions in solids integrated into photonic chips as a compact and heterogeneous platform and 2) nanoscopic and macroscopic oscillators interfaced with light and magnetic field to isolate them from environmental noise.

Rare earth (RE) ions in crystals have been identified as robust optical centers and promising candidates for quantum communication and transduction applications. Lithium niobate (LN), a novel crystalline host of RE ions, is considered as a viable material for photonic system integration because of its electro-optic and integration capability. This thesis first experimentally reports the activation and characterization of LN crystals implanted with Yb and Er ions and describes their scalable integration with a silicon photonic chip with waveguide and resonator structures. The evanescent coupling of light emitted from Er ions with optical modes of waveguide and microcavity and modified photoluminescence (PL) of Er ions from the integrated on-chip Er:LN-Si-SiN photonic device with quality factor of  $10^4$  have been observed at room temperature. This integrated platform can ultimately enable

developing quantum memory and provide a path to integrate more photonic components on a single chip for applications in quantum communication and transduction.

Optomechanical systems are also considered as candidates for light storage and sensing. In this thesis, we also present results of the theoretical study of coherent light storage in an array of nanomechanical resonators. The majority of the thesis is focusing on an optomechanical sensing experiment based on levitation. An oscillator well isolated from environmental noise can be used to sense force, inertia, torque, and magnetic field with high sensitivity as the interaction with these quantities can change the amplitude or frequency of the oscillator’s vibration, which can be accurately measured by light. It has been proposed that such levitated macroscopic objects could be used as quantum sensors and transducers at their quantum ground states. They are also proposed as a platform to test fundamental physics such as detecting gravitational waves, observing macroscopic quantum entanglement, verifying the spontaneous collapse models, and searching for dark matter.

In particular, we consider superconducting levitation of macroscopic objects in vacuum whose positions are measured by light. We build an optomechanical platform based on a levitated small high reflective (HR)-coated mirror above a superconductor disk. We use this levitated mirror at ambient conditions to detect the magnetic field with a sensitivity on the order of  $pT/\sqrt{Hz}$ . Moreover, the levitated mirror is used as the end mirror of a Fabry–Pérot cavity to create an optical resonance that could be used to study coherent radiation pressure forces. The platform provides a sensitive tool to measure the various forces exerted on the mirror and it offers the possibility of the coherent optical trapping of macroscopic objects and precision gravity sensing. Moreover, we study the nonlinear dissipation and mode coupling of a levitated HR-coated magnetic mirror above a superconducting disk in vacuum conditions. We observe that by exciting one vibrational mode of the mirror, the vibrational noise of another mode can be significantly suppressed by a factor of 60. We attribute this unique noise suppression mechanism to the mode coupling and nonlinear dissipation caused by the driven magnetic inhomogeneity of the levitated object. Such a suppression mechanism can enable cooling certain modes independent of their detection and position in the spectrum, which may be promising for precision sensing applications.

# 1. INTRODUCTION AND MOTIVATION

The interaction between light and matter is of fundamental importance for various applications. Both classical and quantum mechanical pictures of light or photons as the carrier of information and their interaction with the environment need to be well understood. Light is being currently considered as a perfect information carrier due to its high speed, less interaction with the environment, and large information capacity. Atoms and mechanical oscillators can interact with light to control and process optical information. They can provide an efficient interface for light to develop optical memories or sensors. For example, state-of-the-art engineering of classical and quantum optical systems and mechanical oscillators have resulted in the groundbreaking discovery of gravitational waves by the Laser Interferometer Gravitational-Wave Observatory (LIGO). Most recent results from LIGO suggest a displacement noise level better than  $10^{-17}m/\sqrt{Hz}$  [1]. On the other hand, that atoms strongly interact with photons has been reported to enhance the quantum communication rate [2].

More broadly, scalable light-matter interaction in solids has becoming increasingly critical since it allows to develop solid-state photonic devices for applications in optical communication and signal processing [3], [4], nonlinear-frequency conversion [5]–[7], on-chip lasers and optical sensors [8], [9], and nano/micro-photonic circuits [10]–[12]. Scalable interaction helps to increase the light-matter interaction rate and efficiency, which could enable the large-scale photonic signal processing on chips. At the macroscopic scale, the light-matter interaction through the trapped matters isolated from the environment has also attracted significant attention for application in sensing of fundamental physics quantities such as force, acceleration, and inertia [13], [14]. The levitated macroscopic platforms, in particular, show great potential in sensing gravitational waves and observing the macroscopic quantum entanglement [15].

In this thesis, both atomic and mechanical systems have been explored and a toolbox has been developed to build effective atom-light and light-oscillator interfaces that may be used for the applications such as coherent light storage and sensing of fundamental physics. The structure of this thesis is organized as follows:

In chapter 2, an integrated silicon photonic device with erbium-ions-implanted lithium niobate crystal has been demonstrated and the optical properties of rare-earth ions ( $Yb^{3+}$  and  $Er^{3+}$ ) implanted into lithium niobate (LN) crystals have been characterized.

In chapter 3, by controlling the collective dynamics in an optomechanical array, an optomechanical system for the broadband and scalable coherent light storage has been studied, theoretically.

In chapter 4, an optomechanical platform based on a levitated mirror above a superconductor disk has been studied. A Fabry-Pérot cavity that uses the levitated mirror as its cavity end mirror was built and characterized. In addition, the levitated mirror is used as an AC magnetic field sensor and the sensitivity reaches the pico tesla (pT) scale.

In chapter 5, we study the nonlinear interactions between vibrational modes of a levitated magnetic mirror above a superconducting disk in vacuum conditions. We observe that by exciting one vibrational mode of the mirror, the vibrational oscillations of another mode can be significantly suppressed. This suppression mechanism is associated with the mode coupling and nonlinear dissipation of the levitated mirror in the presence of an external drive.

In chapter 6, we summarize the results discussed in this thesis, and propose the future work plans to improve and enhance the sensitivity of the superconducting levitated magnetic mirror in sensing. They mainly include such as reducing the seismic noise, applying active feed back cooling, and building a stable optical cavity based on the levitated mirror. We also propose that the potential application toward precision sensing gravity with the levitated magnetic mirror.

## **1.1 Light-matter Interaction for Coherent Light Storage**

### **1.1.1 Coherent Light Storage in Atoms**

Quantum repeaters are proposed as a way to increase quantum communication distance and enhance the distribution of entanglement [16], [17]. One of the building blocks of quantum repeaters is quantum memory that is used to store light and synchronize the entangled photons arriving at different nodes [18]. Quantum memories can be realized by controlling

the coherent light storage at the single-photon level. Atoms can be used to build quantum memories where by mapping optical information to atomic excitations, light can be practically stopped. There are different approaches towards coherent light storage in atoms including electromagnetically induced transparency (EIT) and photon echoes [19], [20]. This mapping of information from the light field to atomic excitations is referred to as the storage process, which is usually accompanied by a subsequent retrieval of the stored information.

There is a set of important parameters generally being used to evaluate the quality of quantum memory including fidelity, storage efficiency, storage time, bandwidth, and multimode capacity. Fidelity defines how close the retrieved light optical quantum state  $|\Phi_{out}\rangle$  is to the input optical quantum state  $|\Phi_{in}\rangle$ . Storage efficiency is the ratio of retrieved optical power to input optical power. Storage time is determined by atoms' coherence time and quantifies how long a memory can store quantum information. For quantum applications, a minimum storage time of  $\mu\text{s}$  to  $1\text{s}$  for quantum repeaters is required for quantum repeaters and several GHz of bandwidths is also desirable. Multimode capacity indicates how many qubits can be stored in parallel in a memory. Materials with large inhomogeneous broadening for light storage attract much attention as they can store multiple optical modes. The multimode capacity can be quantified by the product of storage time to bandwidth for a coherent atomic memory.

Both single atoms and an ensemble of atoms can be used to store light in a quantum memory. Single atoms optically trapped in cavities [21], [22], single electrically trapped ions in vacuum chambers [23], single nitrogen-vacancy (NV) center in diamond [24] and quantum dots [25] are examples of single-atom memories.

Atomic ensemble-based coherent light memories are also promising because they can store multiple modes which enables storage of different types of quantum states such as squeezed light states. They include cold or ultra-cold atomic gases [26]–[28], warm atomic vapors [29], rare-earth-doped crystals [30], [31] and microcavity-coupled NV center ensemble [32]. To control the mapping in and out of the atomic states, different protocols have been proposed and tested. One typical protocol used in solid-state atomic memories is called atomic frequency comb (AFC) that is proposed in 2009 by Afzelius, et al [33]. It is an efficient multimode storage protocol based on the spectral shaping of inhomogeneously



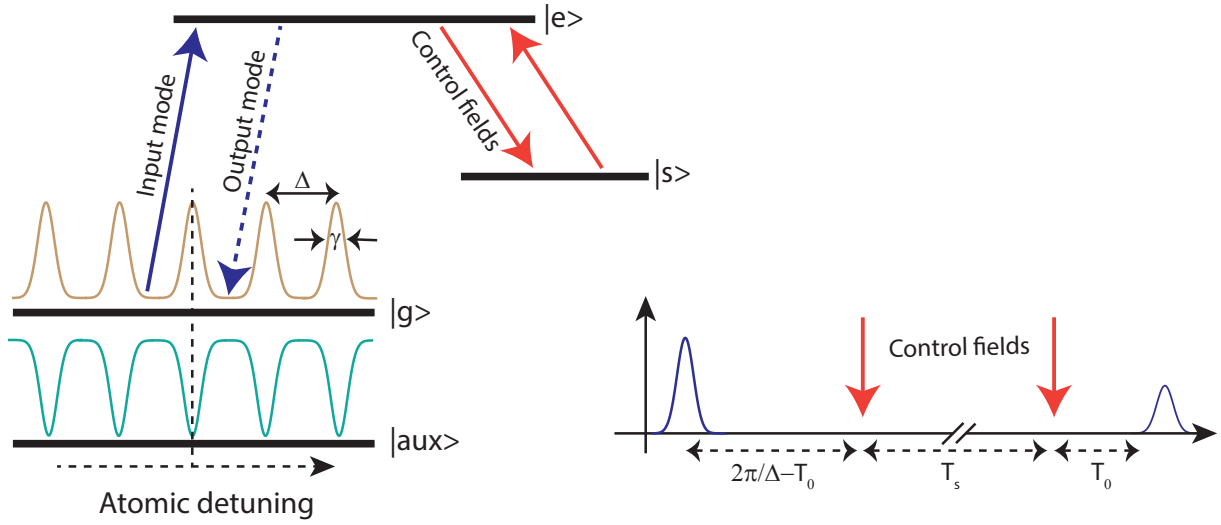


**Figure 1.1.** AFC quantum memory principles. Shaped inhomogeneous broadening by selectively pumping the atoms from ground state  $|g\rangle$  to the metastable state  $|aux\rangle$ . The linewidth of each frequency peak in AFC is  $\gamma$  and the neighboring peaks are spaced by  $\Delta$ . The input mode is fully absorbed and excites the AFC modes coherently. One control field is used to transfer the stored coherent information to the spin state  $|s\rangle$  and the other is applied to convert the spin state information back into optical coherence.

broadened atomic transitions. The inhomogeneously broadened absorption spectra in the atomic ensemble between the ground state  $|g\rangle$  and excited state  $|e\rangle$  is spectrally shaped so that the atomic density function includes a series of narrow absorption peaks equally spaced in frequency. The shaped absorption frequency profile, formed by selectively pumping the atoms from the ground state  $|g\rangle$  to a metastable state  $|aux\rangle$ , is called atomic frequency comb, as shown in Fig. 1.1.

When the input pulse (probe) is initially absorbed by AFC modes coherently, atoms of different frequencies are excited all in-phase. But the relative phase quickly changes due to atoms' frequency difference. Atomic excitations will be in-phase again after a time of  $2\pi/\Delta$  because of the periodic comb structure of AFC. The rephasing process causes the absorbed input mode to re-emit, which forms the echo that includes the stored information of input light. This is called the retrieval process. Since the spin states of atoms have relatively

large coherence times, the stored information on excited states  $|e\rangle$  is usually transferred to the spin state  $|s\rangle$  by applying a classical control field. A subsequent control field is used to convert the information from  $|s\rangle$  back to  $|e\rangle$  for the on-demand information retrieval. Using the AFC protocol, high-fidelity storage of 97% of quantum optical states has been achieved [34].

### 1.1.2 Coherent Light Storage with Optomechanics

The field of optomechanics is about the interaction between light and mechanical oscillators. Studying optomechanics enables us to use light to manipulate and measure the states of mechanical oscillators. In recent years, optomechanical systems have been demonstrated to be promising platforms for sensing, quantum information processing, and storage [35]–[37]. The mechanical resonator itself can be used to store coherent optical information as long-lifetime mechanical excitations [38]–[41]. The length and mass of the optomechanical system can vary from a few kilometers and tens of kilograms to nanometer and  $10^{21}$  gram. For example, the suspended mirror in LIGO optomechanical system weighs 40kg and its optical cavity length is around 4km [42].

Radiation pressure, as the core concept of optomechanics, is defined as the force per unit area from light, which carries momentum and transfers its momentum to the objects during its absorption or reflection. This concept was first proposed in the 17th century to explain the phenomenon that the tail of the comet is pointing away from the sun [43]. The momentum,  $p$ , that a single photon carries is given by

$$p = \hbar\omega/c \tag{1.1}$$

where  $\hbar$  is the reduced Plank constant,  $c$  is the light speed in vacuum and  $\omega$  is the angular frequency of light. One of the interesting applications of radiation pressure is "optical tweezers" which was demonstrated to trap dielectric particles using the focused laser light in 1970 by Arthur Ashkin [44]. In addition, radiation pressure can also be used for trapping atoms. When light is reflected by a perfect reflector, twice of the light momentum ( $p = 2\hbar\omega/c$ ) is

transferred to the reflector. For a perfect absorber, the momentum transferred by light is equal to its original momentum ( $p = \hbar\omega/c$ ).

Assuming an incident laser beam with a power of  $P$  is impinging normal to a surface with absorptivity of  $A$  and reflectivity of  $R$  and  $N$  photons are hitting on the surface during a time of  $t$ , then the number of photons per unit time hitting on the surface can be calculated as:

$$\frac{dN}{dt} = \frac{P}{\hbar\omega} \quad (1.2)$$

Therefore, the radiation pressure force exerted by the laser beam on the surface,  $F$ , is described as:

$$F = \frac{dN}{dt} p(2R + A) = \frac{P(2R + A)}{c} \quad (1.3)$$

This equation shows that the fluctuations from an electromagnetic field can be transferred to the oscillator and vice versa. Such an interface can be used to coherently map field excitations to/from mechanical vibrations. It has been reported that a silica microsphere with a diameter of 30um can be used as a single-mode coherent optomechanical memory to store the optical information with a storage efficiency of around 9% and storage time of  $3.5\mu s$  [38]. A chip-integrated coherent photonic-phononic memory based on the interaction between photons and phonons from an acoustic hypersound wave has been demonstrated to operate at a few different wavelengths with negligible cross-talk [45]. Thermal noise will wash out quantum coherence mapped onto the mechanical oscillator. So for quantum operations, the oscillator needs to be kept as its quantum ground state. Classical storage of bright coherent light does not require ground-state cooling. Another factor limiting the storage time for optomechanical memories is the intrinsic dissipation from the mechanical resonator itself. It has been shown that by applying an additional optical field, one can modify the dynamics of optomechanical interactions using parametric feedback increasing lifetime by an order of magnitude [36].

### 1.1.3 Integrated Solid-state Photonics

One widely investigated material for the integrated solid-state photonic systems is fused silica due to its remarkable advantages such as low propagation loss in the tele-communication band, easy coupling with single-mode optical fibers, low-temperature dependence, and low birefringence.

Moreover, silicon-based integrated photonic systems have also been largely reported such as silicon-on-insulator [46], [47], silicon nitride ( $\text{Si}_3\text{N}_4$ ) [48], [49] and silicon carbide (SiC) integrated optical devices [50]. Silicon-based integrated platforms are promising mainly because their development could benefit from the current mature fabrication technologies. Using silicon nitride resonators with a quality factor larger than  $10^5$ , a photon pair generation rate with more than 15000 per second has been demonstrated [48]. But there are also some limitations about silicon-based integrated photonic solid-state platforms such as relatively low mode-matching with optical fibers and high propagation losses because silicon has a relatively large absorption coefficient from the visible to infrared wavelengths.

There are other photonic integrated systems which are built on lithium niobate (LN) [51]–[54], silicon carbide [7], gallium arsenide [55], indium phosphide [56] and silicon oxynitride [57]–[59] for quantum applications. LN crystal, the so-called “silicon of photonics”, has been considered as an interesting material for the development of integrated on-chip quantum optical devices due to its strong nonlinearity, large electro-optic coefficient, large piezoelectric effect, and well-established fabrication technique for optical waveguides. LN-based reconfigurable waveguide quantum circuits have been reported for the generation and manipulation of entanglement of photons [51]. Also, a broadband ( $\sim 5\text{GHz}$ ) waveguide coherent light memory based on thulium-doped lithium niobate has been developed at low temperature [52]. Very recently, centimeter-long thin-film lithium niobate-on-insulator integrated photonic waveguides and micro-ring resonators implanted with rare-earth Yb ions have also been demonstrated [53]. Integration of active optical centers such as rare-earth ions with solid-state photonics opens doors to new functionalities and applications. LN material as a crystalline host for rare-earth ions offers additional advantages in terms of the optical and coherent properties of ions.

## 1.2 Light-matter Interaction for Sensing

Light-matter interaction has been widely applied for sensing various physical quantities ranging from magnetic and electrical fields to time, frequency, and temperature [60]. For example, NVs in a diamond as solid-state sensors have been shown a sensitivity of  $pT/\sqrt{Hz}$  in sensing magnetic field [61]. Optomechanical systems using the interaction between light and mechanical oscillators have also been investigated for sensing of displacement, force, and mass [62]. An integrated optomechanical displacement sensor has been recently shown a sensitivity of  $45fm/\sqrt{Hz}$  [63]. A SiN trampoline resonator based on optomechanical interaction has been demonstrated as a force sensor with a sensitivity of  $20aN/\sqrt{Hz}$  [64].

To reach the low-noise vibration regime with optomechanical systems, it is important to minimize the thermalization and decoherence processes by reducing the coupling between these systems and the thermal reservoir. Till now, this has required the use of cryogenic operations [65] or a complicated process of fabricating nanostructures exhibiting phononic bandgap characteristics [66]. Since Ashkin discovered that using one focused laser beam can stably trap the dielectric particles in trapping potentials due to the gradient force [44], levitated optomechanics has gained remarkable attention. As a result, new optomechanical platforms have been built to study quantum mechanics at the macroscopic scale. The main advantage of levitated optomechanical systems over conventional clamped ones is their potentially excellent isolation from the environment. The mechanical oscillations of the systems can be largely decoupled from the surroundings to achieve ultra-high mechanical quality factors. For example, a levitated silica nanoparticle with a radius of 50nm in an optical cavity using optical tweezers has been reported to have a quality factor as large as  $10^{12}$  under vacuum conditions ( $10^{-10}$  Torr) [67]. It also has been demonstrated that laser-cooling an optically trapped nanoparticle in the cavity into its quantum ground state of motion at room temperature is possible [68]. It has been shown that in this system the phonon occupation number could be as low as  $n=0.43$  that is corresponding to a temperature of  $12.2\mu K$  and ground-state probability of 0.7. It has been theoretically suggested that the optically trapped dielectric microspheres or microdisks could be used to detect the gravitational wave at a frequency above 100kHz [69]. So optical trapping of nanoparticles and even macroscopic

objects is being considered to remove the dissipation from clamping losses while the trapped particles or objects act as mechanical oscillators. However, this conventional optical trapping technique suffers from the scattering-induced heating on the trapped nano-/micro-scale objects.

Other than the levitated resonators using optical trapping, there are other levitated systems such as magnetic traps [70], [71] and Paul traps [72] that do not rely on the focused laser beam to get the objects trapped and therefore could reach the lowest noise level limit. One example of magnetic traps is superconductor levitation. When a material transforms its normal state to its superconducting state which is usually achieved at low temperatures, the material will actively exclude the magnetic fields from its interior, which is called the Meissner effect. Superconducting levitation using magnetic force enables trapping larger objects and macroscopic particles with resonant frequencies of less than 1kHz. Superconducting levitation can also be used to achieve complete passive trapping, which can in principle reduce the unwanted noise introduced by the trapping itself.

### 1.2.1 Superconducting Levitation

A superconductor is a material that conducts electricity with zero electrical resistance and prevents the external magnetic field from penetrating. There are two different types of superconductors, one is type-I and the other is type-II. The Type-I superconductors completely obey the Meissner effect while type-II superconductors could allow the penetration of the external magnetic flux if the external magnetic field is larger than their critical fields. This is called an intermediate/mixed state or vortex state. The Type-I superconductors are in general metal and metalloids, which have relatively low critical temperatures ( $<10\text{K}$ ) and critical magnetic fields ( $<1\text{T}$ ). Type-II superconductors are typically metal alloys, which exhibit much higher critical temperature ( $>90\text{K}$ ) and critical magnetic fields ( $>10\text{T}$ ).

It is known that levitating a magnet over a superconductor is possible due to the expulsion of the magnetic fields from the inside of the superconductor below its critical temperature. This is so-called "superconducting levitation". When a magnet is placed near a superconductor that is in its superconducting state, the supercurrents will be induced on the

superconductor surface and this can be modeled by considering the images of each magnetic pole of the magnet inside the superconductor. Thus, the magnet can be levitated over the superconductor because of the repulsive force between the magnet and its image inside the superconductor. In principle, both levitating a magnet over a superconductor and levitating a superconductor in a given magnetic field can be realized. A magnetically trapped resonator has been reported as a well environmentally-isolated system [14] due to its passive trapping mechanism whereas other trapping systems need active fields for stabilization [70]. Because of this, superconducting levitation has been applied to observe macroscopic quantum superposition states [73], [74], fundamental physics parameter sensing such as force and inertia and acceleration [13], [14], and even gravimetry [15]. As reported in [75], a mechanical quality factor of more than  $10^7$  and a mechanical damping time of  $10^4$ s are achievable for the magnetically levitated neodymium-based microparticle with the radius of  $27\mu m$  under vacuum pressure of  $10^{-5}$ mbar at temperatures around 4K using type-I superconductor. The direct coupling between the magnetically-trapped single micro-magnet and a single NV center in diamond has also been recently investigated [76]. It provides a new platform towards coupling the individual spin qubits with the mechanical motion of macroscopic objects for testing of mesoscopic quantum behaviors. The magnetically-levitated oscillator has also been suggested as a super-sensitive sensor for magnetic field sensing. A levitated ferromagnetic needle has been theoretically considered as a perfect magnetometer [77]. It was predicted that the needle can even have a few orders of magnitude higher sensitivity than atomic magnetometers and in principle surpass the standard quantum limit (SQL). Motivated by this, an analysis of a single magnetic needle has been performed in the presence of an external magnetic field [78] for achieving ultra-sensitive magnetometry with high precision. In this thesis, we mainly focus on the study of levitated optomechanical systems at the macroscopic scale. We study the trapping and dissipation mechanisms for a levitated mirror whose motion can be precisely measured with an optical field.

### 1.2.2 Trapping and Noise in Superconducting Levitation

In superconducting levitation, the noise and dissipation are mainly due to the thermal noise, the noise caused by the gas collisions, vibrational noise such as seismic noise, and other noise associated with the environmental magnetic noise including eddy currents and magnetic hysteretic noise.

#### Thermal Noise

The superconducting levitated magnet can be considered as a nonlinear Duffing oscillator. Then the restoring force ( $F$ ) is the repulsive force between the levitated magnet and its image inside the superconductor, which is nonlinear and directly acting on the magnet. To use the levitated magnet as a mechanical oscillator for sensing applications such as a force sensor, magnetic field sensor or torque sensor, the sensitivity is the most important quantity that needs to be considered. For a levitated oscillator, the sensitivity is generally limited by the noise that drives this oscillator. For example, if one resonator is in its thermal equilibrium state with the thermal bath, then the thermal force ( $F_{th} = 4k_B T m \frac{\omega_0}{Q}$ , where  $k_B$  is the Boltzmann constant,  $m$  is the resonator's mass,  $T$  is the temperature of the thermal bath,  $\omega_0$  is the resonant frequency, and  $Q$  is the quality factor of the resonator) is the force noise that limits the sensitivity of the resonator for sensing.

#### Gas Collisions

In general, the damping rate due to the collisions of gas can be described by

$$\tau_g \approx \frac{CPR^2}{m_g v_g} \quad (1.4)$$

where  $C$  is a constant,  $C \approx 16$ ,  $P$  is the gas pressure (vacuum chamber pressure),  $r$  is the radius of the superconducting levitated magnet,  $m_g$  and  $v_g = \sqrt{3k_B T / m_g}$  are the mass and the thermal velocity of the gas molecules, respectively [79]. The damping caused by the gas collisions can be neglected under certain vacuum conditions.



## Seismic Noise

The superconducting levitated objects have relatively lower resonant frequencies ( $<1\text{kHz}$ ), which makes them susceptible to the seismic noise that can be significantly larger than the thermal noise. Typically, the seismic noise in a lab setting above  $1\text{Hz}$  can be described as follows [80],

$$S_{\text{sei}}^{1/2} \sim [\frac{10^{-9}}{(f/\text{Hz})^2}]m/\sqrt{Hz} \quad (1.5)$$

It means for the resonance frequencies ranging from 0 to  $100\text{Hz}$ , the seismic noise would be in the range between  $\sim 10^{-9}m/\sqrt{Hz}$  and  $\sim 10^{-13}m/\sqrt{Hz}$ . The lower the resonant frequency of the levitated magnet is, the higher the seismic noise would be. The seismic noise could be very different for different locations where the labs are built.

Other than the seismic noise and thermal noise caused by gas collisions, the magnetic noise including the unavoidable magnetic hysteretic noise and eddy current dissipation is another noise source for the superconducting levitated objects.

## Noise from Eddy Currents

Assuming the levitated object is a permanent spherical magnet that is fully magnetically saturated and has a finite electrical conductivity  $\sigma$ , the dissipated energy due to the effect of the eddy currents can be calculated as [75]:

$$W_{\text{edge}} = \frac{\mu_0}{4\pi} \omega \alpha'' B^2 V \quad (1.6)$$

where  $\alpha'' = 1/5(R/\delta)^2$  is the imaginary part of the eddy current polarizability,  $B$  is the averaged effective magnetic field from the surroundings of the superconducting trap, and  $V$  is the volume of the levitated magnetic object with the resonant frequency of  $\omega$ .

## Noise from Magnetic Hysteretic Losses

For the magnetic hysteresis losses, the eddy current polarizability  $\alpha$  can be replaced by the imaginary part of the magnetic susceptibility  $\chi''$ . Using a similar method as for the calculation of dissipated energy due to eddy currents, the total dissipated power due to magnetic hysteretic losses is given as follows [75]

$$W_{hys} = \frac{\omega}{2\mu_0} \chi'' B^2 V \quad (1.7)$$

Similar formulas to calculate the dissipated energy caused by eddy currents and magnetic hysteretic losses can be derived by directly integrating the power dissipation if the levitated object is not spherical and has other geometric shapes.

## Mode Coupling

The dynamics of one superconducting levitation system can be well described using the advanced mirror image method or the frozen image method [81], [82]. Based on this method, there are two images of the levitated magnet generated inside of superconductor, one is called frozen image generated before levitation and another is called diamagnetic image generated after levitation. Then the superconducting trapping potential energy and the equations of motion could be derived by calculating the interaction energy between the levitated magnet and its two images. For one superconducting levitated magnet, if it moves in one direction, the positions of its two images also change, which causes the change of trapping potential energy and therefore affects the motions along other directions. In other words, the displacement of the levitated magnet gives rise to the variation of supercurrents within London penetration depth on the superconductor surface, which in part changes the trapping potential energy. As a consequence, the coupling among different modes could occur through the superconductor. It has been reported that one translational mode  $\mu$  and one rotational mode  $v$  are linearly coupled for one freely-levitated permanent magnet above a high-temperature superconductor (HTS) [83]. The mode coupling also exists between the translational modes. For example, the vertical oscillation mode has been found to be

coupled with the horizontal vibrational mode for a HTS magnetic levitation system [84]. In principle, depending on the superconducting levitation experimental configuration, the magnetic field inhomogeneity, the magnetization axis, and geometry of the levitated magnet, any two modes of the magnet could couple to each other. It is possible to make use of this type of coupling to reduce the vibrational noise of certain modes.

## Nonlinear Dissipation

If the levitated magnet over the superconductor is magnetized uniformly and homogeneously along its magnetic axis, the stray magnetic field of the magnet would remain unchanged if the magnet is rotating along its magnetization axis. Then no magnetic damping should be expected in this case. However, in reality, the magnetic field distribution of the levitated magnets is usually more or less inhomogeneously distributed, which is the main reason for the damping caused by the magnetic hysteresis losses. When an external magnetic field is applied to type-II superconductors, the magnetic field vortices are formed inside of the superconductor. In the following, we refer to “type-II superconductor” as “superconductor”. The higher strength of the external magnetic field, the more the vortex density. Once a magnet is levitated above the superconductor, the larger the magnetic field sensed by the superconductor, the larger the trapped magnetic fields inside of SC and therefore the larger amount of magnetic vortices. It is observed that the lossy magnetic hysteretic effect is caused by the moving vortices inside of superconductor for superconducting levitated magnets [85], [86]. The levitated magnet is actually modulating the stray magnetic field sensed by the superconductor with the magnetic variation/fluctuation amplitude of  $\delta B$  because of the field inhomogeneity of the magnet. As a result, the density of pinned/trapped magnetic vortices changes with  $\delta B$ , which is the origin of the magnetic hysteretic dissipation. If  $\delta B$  is smaller, then the density of trapped magnetic vortices on the superconductor surface changes less, which results in less dissipation. This means the damping depends on the amplitudes of the oscillation, which is a signature of the nonlinear damping mechanism. The Bean critical state model [87] was developed to study the hysteretic losses when the superconductor is immersed in an AC magnetic field with the field strength of  $\delta B$ . Since the levitated magnet

above the superconductor acts like an AC magnetic field, Bean's model is widely used to quantitatively calculate the dissipated energy from the superconducting levitated magnet. Based on Bean's model, the dissipated energy per cycle for the spherical levitated magnet is given by

$$W_{dis} = \frac{2}{3j_c\mu_0^2}\pi r^2\delta B^3 \quad (1.8)$$

where  $r$  is the radius of the levitated sphere magnet,  $j_c$  is the critical current and  $\delta B$  is the magnetic fluctuation amplitude caused by the levitated magnet.

Since Bean's model underestimates the dissipated energy by several orders of magnitude as reported in [88], the modified critical state model was proposed later in Refs. [89], [90] to more precisely calculate the dissipated energy during a hysteretic cycle, the formula is shown as follows:

$$W_{dis} = \frac{4-2\eta}{3(j_c t)^{2-\eta}}\mu_0^{\eta-3}(\delta B)^{4-\eta} \quad (1.9)$$

where  $t$  is the thickness of the superconductor and  $\eta$  is a free parameter that varies from 0 to 1.4 and depends on the magnetic flux pin-distribution and coherence length. It is seen that the energy dissipated during a hysteretic cycle is nonlinearly dependent on the magnetic fluctuation amplitude  $\delta B$  sensed by the superconductor.

## 2. RARE-EARTH IONS SCALABLE INTEGRATION WITH SILICON PHOTONICS USING LITHIUM NIOBATE HOST

In order to explore the integration of lithium niobate bulk crystal implanted with rare-earth ions ( $Yb^{3+}$  and  $Er^{3+}$ ) with silicon photonics for the applications of solid-state quantum memory, characterizing the optical properties of Yb and Er ions implanted in lithium niobate (LN) crystals and then developing a bonding method between rare-earth-ions implanted LN crystals and silicon photonic chips are highly demanded. A large portion of this chapter is reproduced from the previously published work [91], with the permission of AIP Publishing.

### 2.1 Introduction

Implementation of as-of-yet unrealized scalable quantum photonic networks requires the integration of compatible photon sources and quantum memories. On-chip silicon photonic elements operating at the telecommunication wavelengths are attractive for implementation of single-photon sources [92]. Moreover, rare earth (RE) crystals have been used to implement solid-state quantum memories at these wavelengths [93], [94]. Integration of sources and memories on a single platform capable of carrying multiplexing tasks is a grand challenge for future quantum optical communication [95]. Rare earth (RE) ions in crystals have been the attractive optical centers for applications in quantum information processing and communication [96]–[98] due to their relatively low sensitivity to the crystalline hosts. Using RE crystals, record-high coherence time [99], quantum storage efficiency in solids [100], and quantum storage bandwidth [101] have already been demonstrated. Integration of RE crystals with silicon photonics is an important step toward the realization of multiplexed quantum photonic networks [102], [103]. Integration of silicon photonic structures with RE doped yttrium orthosilicate crystals and miniaturization of RE-based devices are being explored for single-photon generation [104] and quantum light storage [30]. As one of the RE crystalline hosts, lithium niobate (LN),  $LiNbO_3$ , is very attractive and has recently emerged as a viable material for heterogeneous photonic system integration due to its electro-optic, nonlinear, and acousto-optic properties as well as its integration capability. LN-based microphotonic

fabrication was used to demonstrate the functional photonic devices with high-speed optical modulation [105]–[107]. Furthermore, RE doped bulk LN crystals have been used for implementation of quantum memories [52]. To achieve light confinement in RE-doped LN crystals and enhance light-matter interactions for quantum applications, Tm-doped LN waveguides have been fabricated in the bulk LN crystals in which broadband quantum storage [52], relatively long coherence time [108], and non-destructive detection of photonic qubits [109] have been achieved. However, doping RE ions into crystals cannot achieve the nanoscopic engineering of RE ions which is required in building scalable and integrated quantum networks. The ion implantation technique is considered as a versatile way to enable doping RE ions into the desired locations in the host crystals such as LN [110], which is important to develop novel integrated photonic chips for quantum applications. Further development of solid-state quantum photonic devices operating near the telecommunication bands and the ability to integrate such devices with silicon photonic systems may address the outstanding challenges of future quantum photonic networks. Therefore, RE-implanted LN crystal integration with silicon photonics has great potential to bring multiple functionalities to the future photonic networks, and it is specifically important for the development of integrated quantum memories.

In this chapter, we investigate the activation and characterization of LN crystals implanted with Yb or Er ions and discuss their scalable integration with silicon photonics. Using a direct bonding technique, we integrate the Er-implanted LN crystals with Si-SiN waveguides and microresonators and study the evanescent coupling of light emitted from Er ions in LN crystals to the underlying Si-SiN structure. We observe the superluminescent light emission from Yb ions in the bulk Yb-implanted LN crystal and modified photoluminescence (PL) of Er ions in the presence of Si-SiN microresonator integrated with the Er-implanted LN crystal.

## 2.2 Implantation of Er and Yb Ions into Lithium Niobate Crystals

We implant Yb ions into the LN crystal (z-cut and stoichiometric from CRYSTAL GmbH) using the energy and fluence of 70 keV and  $10^{14}$  ions/ $cm^2$ , respectively. In the case of the

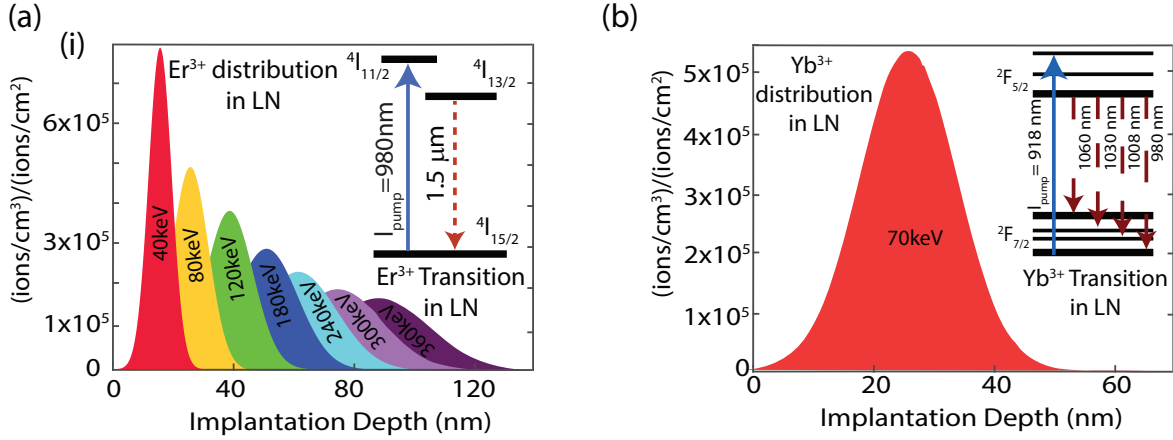


**Figure 2.1.** (a) Er ions' distribution in Er-implanted LN crystals based on the SRIM calculation. (b) Yb ions' distribution in Yb-implanted LN crystals based on the SRIM calculation. The two insets show the schematic energy level diagrams of Yb and Er ions in LN crystals, respectively.

Yb implanted LN (Yb:LN) crystal, subsequent annealing is performed after implantation at a temperature of  $700^\circ\text{C}$  for 24h under a nitrogen atmosphere. The stopping and range of ions in matter (SRIM) calculation show that Yb ions are located about 25 nm below the top surface of the Yb:LN crystal with a Gaussian distribution of the width 15 nm as seen in Fig. 2.1. To achieve a uniform Er ions' concentration near the LN crystal surface and avoid dipolar interactions among Er ions as well as to maximize the PL signal, we carry out implantation with varying energies from 40 keV to 360 keV and ion fluences from  $5.3 \times 10^{12}$  to  $2.4 \times 10^{13}$  atoms/ $\text{cm}^2$ , respectively. The implantation depth of Er ions in the LN crystal varies from 20 nm to 100 nm because of the different implantation energies based on the SRIM simulation. After implantation, three-step annealing ( $400^\circ\text{C}$  for 8 h,  $800^\circ\text{C}$  for 8 h, and  $1100^\circ\text{C}$  for 3 h) is performed for Er:LN crystals under a nitrogen atmosphere to repair the lattice damage induced by the implantation. As reported in Refs. [111], [112], the undoped LN crystals were observed to turn black when annealed above around  $600^\circ\text{C}$ . But we have not observed any visible change in the transparency of Yb/Er-implanted LN crystals after annealing.

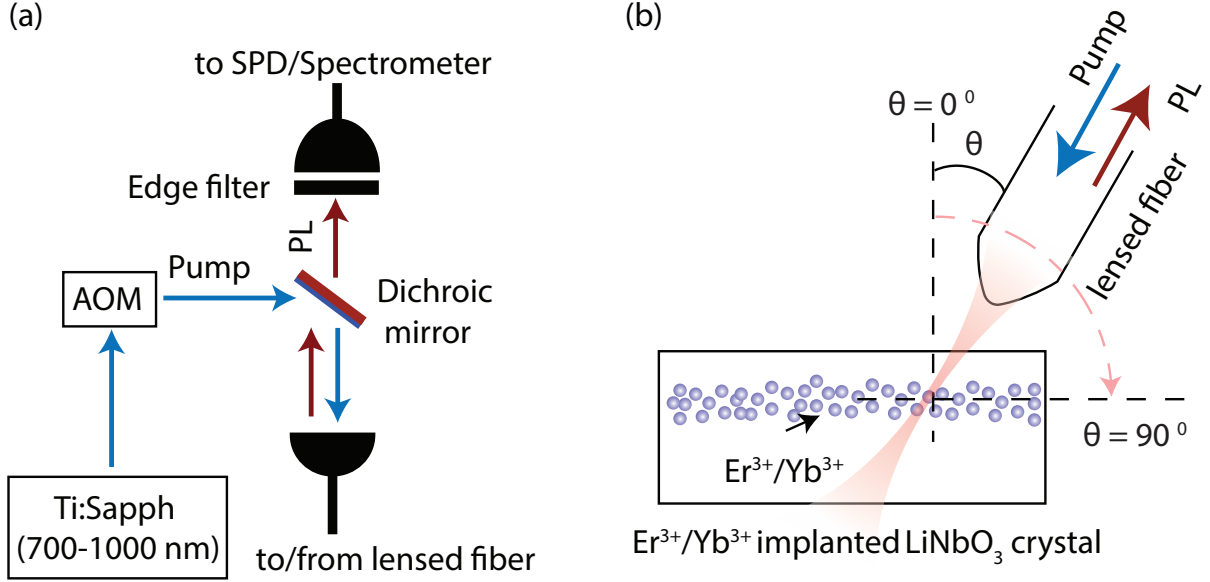


**Figure 2.2.** (a) Experimental setup of detecting PL emission from an ensemble of Yb and Er ions implanted in LN crystals. (b) Excitation and collection through a lensed fiber and the angle of the fiber is altered while photoluminescence decay is recorded

### 2.3 Optical Characterization of Yb-implanted Bulk LN Crystals

To characterize the optical properties of the Yb:LN crystal, we first measure the photoluminescence (PL) decay of Yb ions from the optical transitions between  $^2F_{5/2}$  and  $^2F_{7/2}$ , which is excited with 918 nm pump light using the setup shown in Fig. 2.2(a). We use one lensed fiber with the spot size of  $2\mu\text{m} \times 2\mu\text{m}$  for both excitation and PL collection while varying the excitation/collection angle ( $\theta$ ) as described in Fig. 2.2(b).

Fig. 2.3(a) shows the PL lifetime of Yb ions in the Yb:LN crystal and their total PL counts as a function of  $\theta$ . The lifetime increases as the fiber approaches the horizontal direction ( $\theta = 90^\circ$ ) from the normal direction ( $\theta = 0^\circ$ ), an effect attributed to the reabsorption of PL light (radiation trapping). This is because along the horizontal direction, the optical density (OD) of ions is the largest, resulting in Yb ions' reabsorption at around  $1\mu\text{m}$ . We noticed that at low pump powers, the excited state lifetime ( $\tau$ ) at  $\theta = 90^\circ$  is almost twice longer than  $\theta = 0^\circ$  whether at 4 K or room temperature. For Yb ions' decay measurement



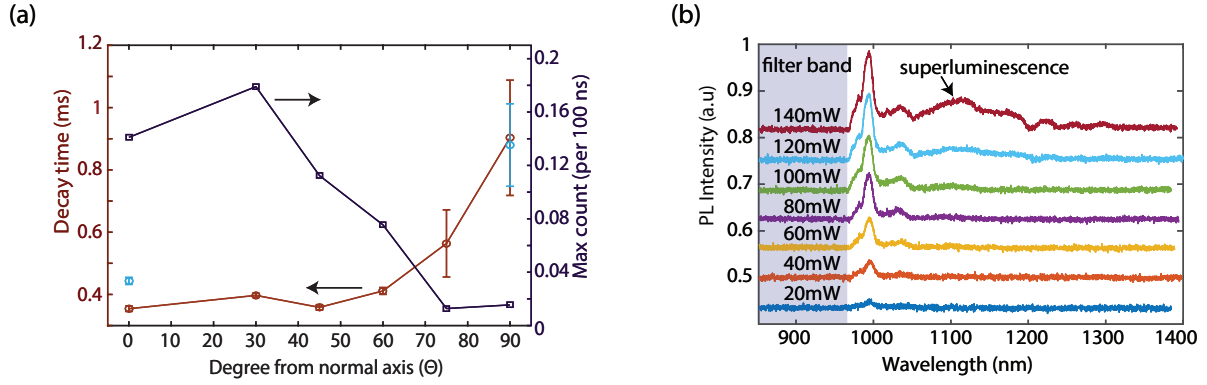


**Figure 2.3.** (a) The photoluminescence lifetime (red circle) and peak intensity (dark-purple rectangle) as a function of the collection angle of the lensed fiber from the axis normal to the sheet of implanted Yb ions in the LN crystal at room temperature (300 K). The blue data points show the decay time measurement at 4 K. (b) The photoluminescence spectrum of Yb ions implanted in the LN crystal plotted with the increasing pump powers from 20 mW (bottom blue line) to 140 mW (top red line) where a different intensity offset is used for each pump power.

taken at 90 degrees (light beam is almost parallel to the Yb atomic plane), the lensed fiber is positioned parallel to the crystal surface and its center is aligned to the implanted Yb atomic plane on the side of the Yb-implanted LN crystal. It can be seen that the PL lifetime of Yb ions does not noticeably change at a low temperature of 4K compared to the room temperature lifetime measured at the same detection angle ( $\theta = 90^\circ$  or  $0^\circ$ ), indicating the negligible nonradiative decay. The spontaneous emission from Yb ions can be optically amplified (superluminescence) at high pump powers. That is why we begin to observe the gain and significant shortening of the lifetime as the pump power increases beyond around 120 mW. The PL spectrum of bulk Yb:LN is plotted in Fig. 2.3(b) for different pump powers. The change revealed in this spectrum with increasing pump power is another signature of superluminescence. Additionally, we also looked for the superluminescence from the Er-implanted LN crystal; however, it was not observed due to the limited pump power we have near  $1.5\mu\text{m}$ . Based on our experimental results, the threshold of observing superluminescence for Yb ions implanted in LN crystal is about 30 mW.

In terms of Er/Yb ions' inhomogeneity caused by the implantation, it can be almost solved by careful post-annealing after implantation. Also, the current goal of this work is to build a solid-state quantum memory based on the integrated Er:LN-Si-SiN or Er:LN-Si device. Like many atomic memories including atomic frequency comb [33], they all rely on the inhomogeneous broadening for the light storage and the large bandwidth storage is only possible when taking advantage of the large inhomogeneous broadening in the rare-earth-doped crystals. Thus, having relatively large inhomogeneous broadening is helpful to build the quantum memory based on Er/Yb-implanted LN crystal.

## 2.4 Fabrication of Si and SiN Finger-type Microresonators

We fabricate finger-type microresonators using Si and SiN materials. The fabrication process of such structures starts with a (100) silicon wafer with a  $3\mu\text{m}$  thick thermally grown silicon oxide layer. First, a stoichiometric SiN layer of 480 nm is deposited in the horizontal tube furnace of a low-pressure chemical vapor deposition (LPCVD) tool with a gas mixture of dichlorosilane and ammonia at a temperature of  $800^\circ\text{C}$ . Next, an electron-beam resist of hydrogen silsesquioxane (HSQ) is spun over the sample and device patterns.

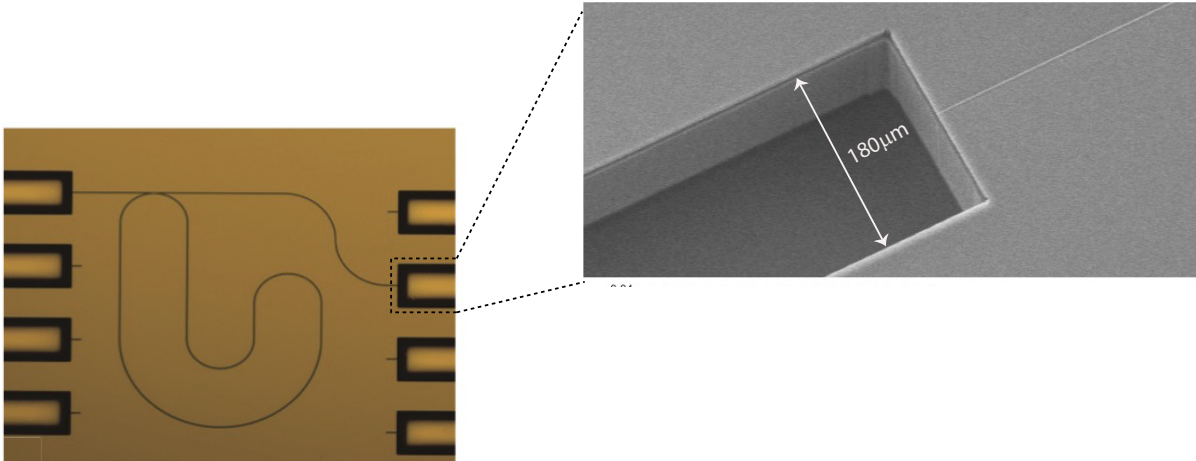


**Figure 2.4.** The scanning electron microscopy (SEM) image of the U-groove and the top-view optical microscopy image of Si-SiN waveguides and finger-type resonators.

The device patterns (waveguide and microresonator structures) are written by a 100 kV ultrahigh-resolution, wide-field electron beam lithography (EBL) tool. Reactive-ion etching (RIE) is then performed to etch the SiN using HSQ as an etch mask by an inductively coupled plasma RIE machine. We use  $\text{CHF}_3/\text{O}_2$  chemistry to etch the SiN to create an almost vertical etching profile. The finger-type shape of the resonator is chosen to achieve a long optical path while having a relatively small footprint. By using this kind of resonator, we can prevent nonlinear interactions while having large light-atom coupling and a large effective atom number. It has been shown at Purdue, that such finger-type shape of resonators will not suffer from bending loss and can provide record-high optical quality factor [113]. Moreover, the small free-spectral range achieved in this case relaxes the requirement for frequency tuning of the resonator to match the atomic resonance. In order to efficiently couple light to the waveguide, we use a tapered waveguide and then couple the light directly from the fiber to the optical resonators through the waveguide. To have a stable and low-loss fiber-to-waveguide coupling for optical measurements, we use patterned substrates with U-grooves that allow the semi-self-alignment of the optical fibers. The scanning electron microscopy (SEM) image of the U-groove and the top-view optical microscopy image of Si-SiN waveguides and finger-type resonators are shown in Fig. 2.4. The grooves can be placed in any orientation of the wafer using RIE dry etching with tolerance to the misalignment based on double-tip inverse taper design [114]. This method avoids the limitation of wet etching that requires devices to be precisely aligned to the crystal lattice of the wafer. The height of the U-groove is about  $70\text{ }\mu\text{m}$  from the bottom to the nitride layer. It is about half of the diameter of an optical fiber with cladding. Hence, by simply placing the fiber down into the groove, it allows the fiber core to be aligned with the waveguide in close proximity. Then, the fine tuning of the fiber position can be achieved by slight adjustment of the fiber position using the three-dimensional positioning stages.

## 2.5 Inregration of Er-implanted LN Crystal with Si-SiN Microresonators

Since silicon has serious absorption in the spectral range of Yb ions' emission (around  $1\text{ }\mu\text{m}$ ), there would be much light loss if one integrates silicon photonic structures with a

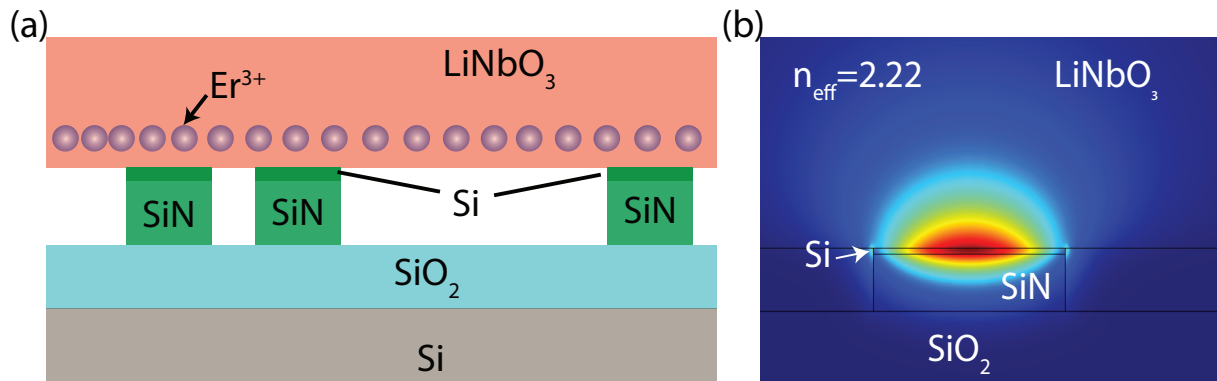


**Figure 2.5.** (a) The cross-sectional view of the Er:LN crystal integrated with Si-SiN waveguides and resonators. (b) Comsol simulation of the optical mode in the cross section of the structure showing enhanced mode confinement at 1.5um in the 50 nm thick Si layer near the crystal.

Yb:LN crystal directly. Therefore, we use the Er-implanted LN (Er:LN) crystal, instead, for the integration with silicon photonic structures.

Before directly integrating the Er:LN crystal with a SiN resonator, we deposit a 50 nm layer of Si on top of the SiN structure using LPCVD, simply named Si-SiN. The 50 nm-thick Si layer is used to ensure sufficient refractive index contrast required to have the enhanced mode confinement near Er ions' positions in the Er:LN crystal while introducing less two-photon absorption loss in the SiN optical path, the cross section of this integrated Er:LN-Si-SiN device is shown in Fig. 2.5(a), and Fig. 2.5(b) shows the mode confinement at 1.5 $\mu\text{m}$  in the thin silicon layer, which is simulated by Comsol.

To integrate the Er:LN crystal with the Si-SiN photonic chip, we directly bond these two without any adhesives using a direct bonding technique [115], [116], the detailed integration process is described in the following. The Si-SiN chip with resonator and waveguide structures and Er:LN crystal are first cleaned using the standard solvent cleaning method to remove the dust particles and contaminants. To be specific, we first put the Si-SiN chip and Er:LN crystal (5 mm $\times$ 2 mm $\times$ 0.2 mm) in acetone for 10 min and then in isopropanol for another 10 min. After that, we rinse them with deionized (DI) water for 15 min. The ultrasonic cleaning is required for the LN:Er crystal cleaning in each step above. Then, the piranha cleaning is applied to both the Si-SiN chip and the Er:LN crystal, meaning they

are placed in the mixture of hydrogen peroxide ( $\text{H}_2\text{O}_2$ ) and sulfuric acid ( $\text{H}_2\text{SO}_4$ ) with their volume ratio of 1:2 for around 15 min. We then use DI water to rinse them for 10 min before using a nitrogen gun to dry them. Once the Si-SiN chip and Er:LN crystal are dry and clean enough, we carefully place the Er:LN crystal on top of the Si-SiN chip manually. Since the piranha cleaning hydroxylates the surfaces and makes them hydrophilic, the crystal will be lightly bonded with the Si-SiN chip at the beginning. Finally, this bonded Er:LN-Si-SiN device is placed on a hotplate for heat treatment at around  $150^\circ\text{C}$  for around 30–40 min to enhance the bonding between the Er:LN crystal and the Si-SiN chip. The integrated Er:LN-Si-SiN photonic device using the direct bonding technique is schematically shown in Fig. 2.6(a).

## 2.6 Optical Characterization of Integrated Er:LN-Si-SiN Photonic Device

Fig. 2.6(b) shows top-view optical microscopy image of Si-SiN finger-shape resonators directly bonded to the Er:LN crystal (left). The width and thickness of the fabricated SiN finger-shape ring resonator are  $1.0\mu\text{m}$  and 480 nm, respectively. The width of the SiN waveguide and the gap between the waveguide and resonator are  $1\mu\text{m}$  and 200 nm, respectively. The U-groove structure seen on the right is used to couple light to the Si-SiN waveguide using a lensed fiber. Similar lensed-fiber coupling is used on the other side of the chip (not shown) to monitor the transmission. The transmission of 1550 nm (dark-red curve) and 980 nm (blue curve) light coupled into the middle resonator of the integrated Er:LN-Si-SiN device is indicated in Fig. 2.6(c). The transmission data are collected from the other side of the integrated Er:LN-Si-SiN device. The light-blue curve shows the transmission of the middle resonator at 1536 nm before integration. All curves are fitted with Lorentzian functions. It is seen that the fitted cavity linewidth of the middle finger-type Si-SiN resonator completely covered by the Er:LN crystal is 10.4 GHz near  $1.5\mu\text{m}$  and 16 GHz near 980 nm. The asymmetry seen from the transmission line shapes in Fig. 2.6(c) could be caused by the polarization shift during the averaged measurement. The coupling efficiency from the lensed fiber to Si-SiN waveguide is about 10%. After power calibration, we estimate an in-waveguide pump power of around 7.6 mW. We use a 1000 nm dichroic mirror to filter the

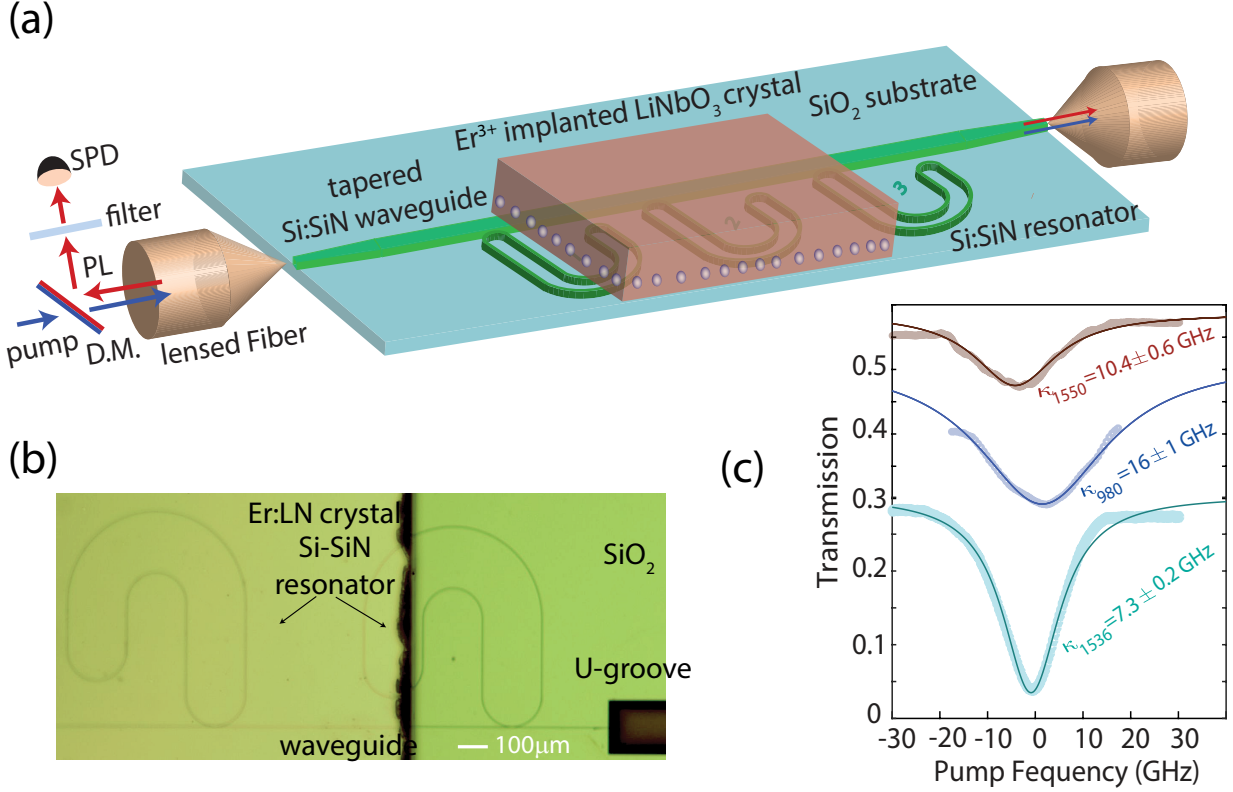


**Figure 2.6.** (a) A schematic of the device showing the Er:LN crystal directly integrated with Si-SiN waveguides and resonators. A simplified layout of the experimental setup is also shown on the left used to detect the emission photons from Er ions in the LN crystal through the Si-SiN waveguide. SPD: single photon detector; D.M.: dichroic mirror (b) Top-view optical microscopy image of Si-SiN finger-shape resonators directly bonded to the Er:LN crystal (c) The transmission of 1550 nm (dark-red curve) and 980 nm (blue curve) light coupled into the middle resonator of the integrated Er:LN-Si-SiN device. The light-blue curve shows the transmission of the middle resonator at 1536 nm before integrating Er:LN crystal with this resonator.

pump signal from the emitted signal and a single photon detector to detect the PL decay of coupled emission of Er ions to the Si-SiN waveguide and resonator.

We found the fitted decay time ( $\tau_{WG} = 0.9$  ms) of the integrated Er:LN-Si-SiN device is always smaller than the PL lifetime in the bulk Er:LN crystal ( $\tau_{WG} = 1.97$  ms) measured from the direction normal to the implanted Er ions' plane as suggested in Fig. 2.7(a). It has been reported that the strain in erbium-doped fibers can cause the lifetime of Er ions to change by about 10% [117], [118]. However, the strain in our case is expected to be much

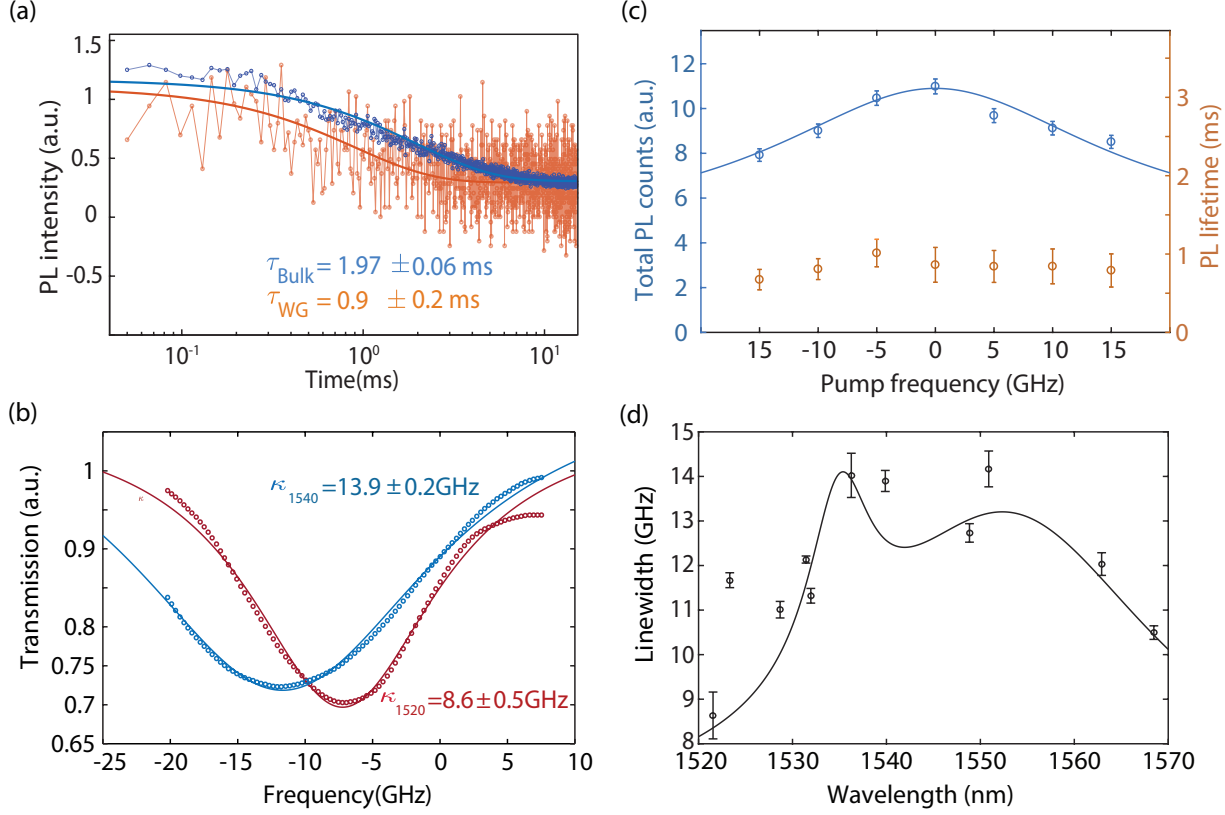


**Figure 2.7.** (a) PL decays of Er ions from the integrated Er:LN-Si-SiN device compared to the Er:LN bulk crystal through evanescent coupling. (b) Cavity transmission signal for two different free spectral ranges (FSRs) of the cavity at 1520 nm and 1540 nm. (c) The total PL counts after the pump is switched off and PL lifetime as a function of frequency detuning of the pump from an optical cavity resonance near 980 nm. The solid line is Lorentzian functions with the linewidth of 17 GHz. (d) The linewidth of the cavity at different FSRs near  $1.5\mu\text{m}$  for the hybrid finger-type resonator of integrated Er:LN-Si-SiN device.

less than what is observed in the erbium-doped fibers, which does not explain a factor of 2 change of the implanted Er ions' lifetime in the integrated Er:LN-Si-SiN device. The bonding strength using direct bonding method between silicon and lithium niobate wafer is around 37MPa [119], so the calculated strain in lithium niobate wafer is around  $220\mu\epsilon$  based on the strain calculation  $\epsilon = P/Y$ , where P is the bonding stress per unit square meter, Y is Young's modulus of lithium niobate wafer (about 170GPa). Since we are also using the direct bonding method to integrate Er:LN crystal and Si-SiN resonator, so the strain induced in the Er:LN



crystal should be on the order of  $220\mu\epsilon$ . With such small strain, the Er ions' lifetime in the integrated Er:LN-Si-SiN device can hardly change according to the references mentioned above. Therefore, we attribute the lifetime change of Er ions in the integrated Er:LN-Si-SiN device to the small free-spectral range (50 GHz) and large cavity linewidth (20 GHz) at 980 nm, which means the pump light excites the Er atoms almost continuously around the cavity resonance. As the maximum absorption of Er doped LN crystals is expected to be around 1540 nm [120]. The linewidth of the cavity at this wavelength should be broader than other off-resonant wavelengths because of the induced loss by the atomic resonance near 1540 nm, which is shown in Fig. 2.7(b). As the maximum absorption of Er ions in LN crystals is around 1540 nm [120], the cavity linewidth is expected to be broader at this wavelength than other off-resonant wavelengths such as 1520nm due to the induced loss by Er atomic resonance close to 1540nm, as shown in Fig. 2.7(d). It reveals that the linewidth increases almost twice at 1540 nm compared to other off-resonant wavelengths such as 1520 nm. As seen in Fig. 2.7(c), when the pump is close to the 980 nm cavity resonance, the PL count increases due to the slight increase in the intracavity pump power on resonance. We do not observe a significant change in PL lifetime vs pump frequency near cavity resonance. We note that the optical Q factor of the Si-SiN resonator after integration with Er:LN is measured to be 9600 at 1.5  $\mu\text{m}$ . The low Q factor, in this case, is mainly limited by the Si layer surface quality deposited by LPCVD (due to its availability). The Q factor is expected to significantly increase when the Si layer is deposited using PECVD system enabling us to achieve better surface roughness. The quality factor of the hybrid integrated Er:LN-Si-SiN resonator is reduced after integration by a factor of approximately 1.5.

One important potential application of this integrated platform developed here is in the realization of integrated quantum memories with silicon photonics. As LN has the electro-optical effect and Er ions have permanent dipoles, applying a local electric field can introduce the Stark shift to the ions using on-chip electrodes [107] and also the frequency shift to the resonators for the control of light-atom coupling and on-demand storage at the telecom wavelength [93]. Other protocols for optical light storage in RE crystals have been proposed which can be implemented in the studied platform [121]. Importantly, arbitrary ion positioning in the crystal lattice via ion implantation creates an additional control knob



to engineer the quantum photonic devices based on rare earth crystals with nanometer ion positioning capabilities [110], [122]. We note that neither high co-operativity nor single ion precision implantation is required for the realization of quantum memories. The small single-ion co-operativity is offset by the number of ions in the crystal collectively interacting with the incident photons. For this reason, the long cavity used in this work and the integrated platform introduced can be used to create strong linear interactions for the on-chip light storage capable of being integrated into a silicon chip. Moreover, the integration method described here can be extended to other RE crystals such as  $\text{LiYF}_4$  crystals exhibiting ultranarrow inhomogeneous broadenings [123] or  $\text{Y}_2\text{SiO}_5$  crystals with ultralong coherence time [94].

## 2.7 Summary

To conclude, we carry out implantation of RE ions ( $\text{Yb}^{3+}$  and  $\text{Er}^{3+}$ ) in LN crystals and characterize the emission properties of these ions while carefully controlling the implantation and annealing processes. We observe the superluminescence from the Yb-implanted LN crystal by investigating the PL lifetime from different angles with respect to the plane where Yb ions are implanted and different pump powers as well. Moreover, we integrate the Er-implanted LN crystal with the Si-SiN photonic chip with waveguide and resonator structures using the direct bonding technique and observe the evanescent mode coupling between the emission mode of Er atoms in the LN crystal and Si-SiN waveguide and cavity modes. The integrated heterogeneous platform based on rare-earth ions in the electro-optical crystal and silicon photonic chip enables the development of advanced and multifunctional photonic devices [107] and also provides a way to integrate more photonic components on one chip for applications in quantum communication.

### 3. OPTOMECHANICAL FREQUENCY COMB FOR LIGHT STORAGE

To solve the problem of the inhomogeneously broadening of an nanomechanical oscillator array caused by imprecision in the nanofabrication process, a optomechanical memory proposal has been theoretically studied for the applications of quantum memory. A large part of this chapter is the reproduction of the previously published work [41], with the permission from Optica Publishing Group.

#### 3.1 Introduction

The optomechanical systems have been considered as hybrid platforms for the investigation of novel physical phenomena at the intersection of quantum photonics, atomic physics, and nanotechnology that can also reveal quantum signatures [124]–[126]. The optomechanical interactions have been used for cooling nanomechanical oscillators to its quantum ground state (QGS) of motion [124], achieving the optomechanical squeezing [125], and creating photon-phonon and phonon-phonon entanglement [126], [127], all signatures of the quantum mechanical regime. Integrated optomechanical circuits are being investigated as scalable platforms for quantum optical information processing [128]–[130], precision mass and force sensing [131]–[133] and study of many-body dynamics [134]–[136]. Recent realization of atom-like phenomena such as cavity sideband cooling [137], optomechanical induced transparency (OMIT) [138]–[140], and optomechanical squeezing [125], [141]–[143] has revealed potential applications of optomechanical systems as engineered and versatile structures for quantum information processing. To date, coherent light storage using a single micromechanical oscillator has been experimentally demonstrated for a classical light pulse [38], [39]. The key to many quantum information proposals based on integrated optomechanical systems is the cooperative behavior in nano-oscillator ensembles. For instance, a coherent light storage protocol was proposed that relies on the collective interaction of light with an optomechanical array [129]. In most cases, the nanomechanical oscillator arrays in an optomechanical system exhibit a large inhomogeneous broadening in the resonance frequency due to the imprecision

in the nanofabrication processes. Therefore, actively tuning the mechanical frequency [144]–[146] of the individual oscillators or strong phononic coupling [130], [147] between neighboring oscillators is proposed to observe the synchronization and cooperative optomechanical effects. The cooperative effects in optomechanical systems have been observed by coupling multiple oscillators and tuning their mechanical frequencies [145], [146]. Also, incorporating mechanical oscillators into a phononic crystal is being investigated as a mean to reduce the mechanical dissipation while increasing coupling to the neighboring oscillators [147]. The collective excitation of this kind generally follows Kuramoto’s model of synchronization [148] where the coupling between oscillators needs to exceed a threshold in order to observe the collective phase dynamics. However, reaching such a crucial coupling regime is experimentally challenging. Recently, it was suggested that an array of weakly-interacting optomechanical oscillators can be coupled and synchronized via a laser drive [149], [150].

In this chapter, we use an optomechanical platform based on a weakly interacting optomechanical array collectively coupled to an external laser drive to study the cooperative optomechanical effect and use it to demonstrate a coherent optical storage technique. In this regime, strong interactions between individual oscillators are not required and linear optomechanical interaction alone is sufficient to observe instantaneous synchronization. We consider an array of high-quality mechanical oscillators interacting with a common optical bus in a waveguide or optical resonator and seek strong collective interaction of light with the ensemble optomechanics. By tuning and reversing the interactions between photons and optomechanical resonators, we investigate the cooperative effects such as the photon-phonon echo enhancing the strength of the light-matter interactions.

### 3.2 Optomechanical Interaction in a Cavity

Considering successfully developed techniques in atomic and optical physics such as atomic frequency comb [33], optical frequency comb [151] and gradient echo [152] techniques, we implement phenomena similar in nature by using mechanical oscillators that behave somewhat similar to atoms. In the originally proposed atomic frequency comb technique for light storage [33], a broad inhomogeneous broadening in the atomic transition that

is present in solid-state systems was used to generate photon echoes recovering the stored optical coherence. In the simplest form, a pump laser is used to “burn” narrow absorption lines in the broad inhomogeneous absorption spectrum (the spectral hole burning technique) [153]. Multiple absorption lines (holes) generated with a fixed frequency spacing ( $\Delta$ ) create an atomic frequency comb fully absorbing a broadband input pulse. As the relative phase between the absorbing atoms matches at every  $2\pi/\Delta$ , a coherent photon echo is emitted to regenerate the input light. This method has been used for quantum storage of optical information [52], [154], [155] with record-high bandwidth crucial for multiplexing resources for a scalable quantum network [156]. We use the analogy between the atomic and optomechanical systems to implement an optomechanical frequency comb memory. The optomechanical echo scheme under consideration is shown in Fig. 3.1(a) – (c). As Fig. 3.1(b) indicates, the probe photon corresponds to the transition  $|n_p\rangle$  to  $|n_p + 1\rangle$ , in which there is no mechanical transition (phonon number  $|n_m\rangle$  remains the same). The red-detuned control light (read/write) interfering with the probe photon leads to one photon being annihilated

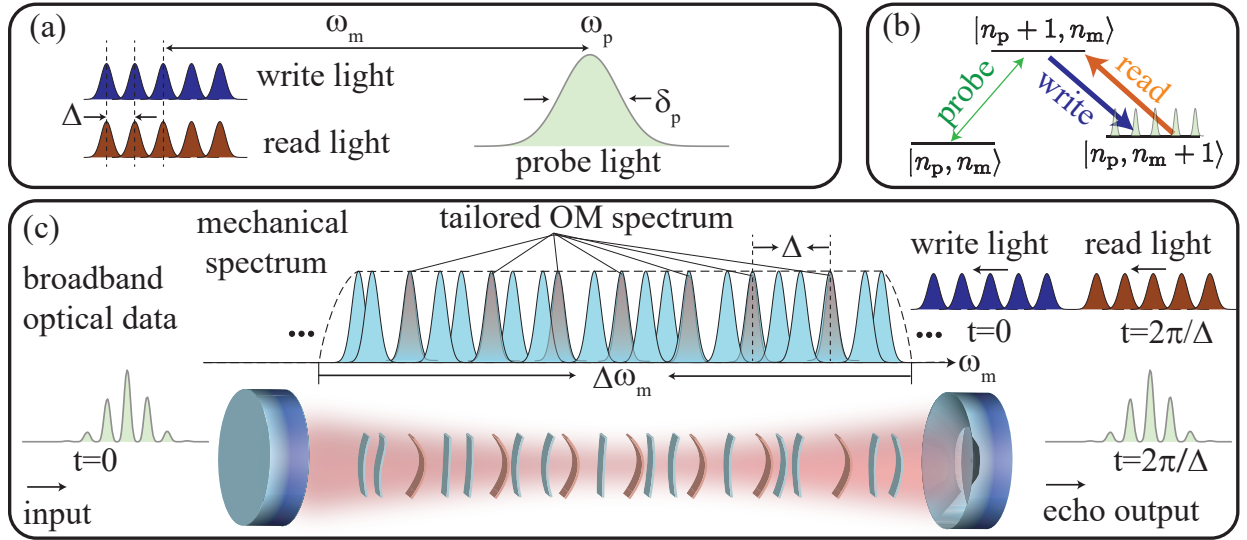


**Figure 3.1.** Broadband data pulse (probe) and “read” and “write” control pulses with multiple frequency comb lines, as depicted in (a), create a controllable optomechanical frequency comb. The interaction scheme and equivalent energy level structure are depicted in (b) for the optomechanical system. (c) Optomechanical interaction between a broadband input pulse and the mechanical oscillators in an array is tailored by the control pulses.

(writing)/created (reading), while one phonon is created (writing)/annihilated (reading) in the cavity, where the energy difference between the two fields takes the form of a phononic excitation. This is how the transition  $|n_p+1, n_m\rangle \leftrightarrow |n_p, n_m+1\rangle$  occurs. The full realization of the optomechanical echo is described schematically in Fig. 3.1(c). Only the oscillation frequencies equal to the frequency difference between the probe and “write” pulse spectral components are excited, mapping the input light into a collective phononic excitation. The resulting collective excitation dephases/rephases at a rate given by the frequency detuning  $\Delta$ . The excitation is subsequently retrieved by the “read” light after a controllable time  $2\pi/\Delta$ , when the phase-matching condition is satisfied.

We use the inhomogeneous frequency broadening present in an ensemble optomechanical array to our advantage to implement reversible and controllable optomechanical transduction. We use a control laser shaped into a frequency comb that is off-resonance from the cavity to engineer the interaction between the probe light, which is resonant with the cavity, and a subset of the oscillators in the array. As the optomechanical interaction mainly occurs when the probe-control frequency difference is equal to the mechanical frequency, multiple comb lines of the control light coherently interfere with the probe spectrum. The coherent interference between multiple frequency components creates an optomechanical frequency comb similar to the multi-frequency interference in the atomic systems [157]. In this way, a broadband probe pulse is fully mapped and stored as mechanical excitations onto a subset of oscillators with equally-spaced frequencies (with frequency spacing  $2\pi/\Delta$ ) in the ensemble optomechanical array. A subsequent “read” frequency comb light retrieves the stored excitations from the ensemble after a time equal to multiples of  $2\pi/\Delta$ . Below we first use approximations to find a simplified analytical description of the storage process and then carry out numerical simulations to quantify the process more accurately.

The total Hamiltonian ( $\hat{H}$ ) of a general optomechanical system basically consists of optical  $\hat{H}_{opt}$ , mechanical  $\hat{H}_{mech}$ , optomechanical interaction  $\hat{H}_{int}$ , and drive  $\hat{H}_{drive}$ . To write the equations of motion, we consider an optomechanical cavity driven with an electric field,  $\mathcal{E}_{in}(t) = \mathcal{E}_c(t) + \delta\mathcal{E}_p(t)$ , where  $\mathcal{E}_c(t)$  and  $\delta\mathcal{E}_p(t)$  represent the frequency comb control (read/write)

and a weak probe field, respectively. The Hamiltonian ( $\hat{H}$ ) of the considered optomechanical system is given by:

$$\begin{aligned}\hat{H} &= \hat{H}_{opt} + \hat{H}_{int} + \hat{H}_{mech} + \hat{H}_{drive} \\ &= \hbar\omega(\hat{z})\hat{a}^\dagger\hat{a} + \sum_j^M \hbar\omega_j\hat{b}_j^\dagger\hat{b}_j + i\hbar\sqrt{\kappa}[\mathcal{E}_{in}(t)\hat{a}^\dagger + \mathcal{E}_{in}(t)\hat{a}],\end{aligned}\quad (3.1)$$

where  $\omega(\hat{z})$  is the resonance frequency of the optical cavity that varies with the mechanical oscillator position  $\hat{z}$ ,  $\omega_j$  is the mechanical frequency of the  $j$ th oscillator inside the optical cavity,  $\kappa$  is the decay rate of the impedance matched optical cavity,  $\hbar$  is the reduced Planck constant,  $\hat{a}$  and  $\hat{a}^\dagger$  represent the annihilation and creation operators of the optical cavity mode,  $\hat{b}_j$  and  $\hat{b}_j^\dagger$  are the annihilation and creation operators of the  $j$ th mechanical mode,  $\mathcal{E}_{in}(t)$  is the drive field of the optomechanical system, and  $M$  is the total number of mechanical oscillators considered in the cavity. The first term in Eq. 3.1 represents both  $\hat{H}_{opt}$  and  $\hat{H}_{int}$ . To obtain the optomechanical interaction Hamiltonian ( $\hat{H}_{int}$ ), we expand the optical resonance frequency ( $\omega(\hat{z})$ ) of the cavity in the displacement around  $\hat{z} = 0$  to the first order we have:

$$\omega(\hat{z}) = \omega_0\left(1 - \frac{\hat{z}}{L_c}\right), \quad (3.2)$$

where  $\omega_0$  is the resonance frequency of the cavity at equilibrium condition and  $L_c$  is the effective length of the optical cavity. The displacement of the intra-cavity mechanical oscillators introduces an effective change in the cavity length and is given by  $\hat{z} = \sum_j^M z_{ZPF}(\hat{b}_j + \hat{b}_j^\dagger)$  where  $z_{ZPF} = \sqrt{\hbar/2m\omega_j}$  is the zero-point fluctuation amplitude ( $m$  is the effective mass of the  $j$ th mechanical oscillator). Therefore, to the first order, the standard optomechanical Hamiltonian of the system reads:

$$\begin{aligned}\hat{H} &= \hbar\omega_0\hat{a}^\dagger\hat{a} + \sum_j^M \hbar\omega_j\hat{b}_j^\dagger\hat{b}_j - \sum_j^M \hbar g_0\hat{a}^\dagger\hat{a}(\hat{b}_j + \hat{b}_j^\dagger) \\ &\quad + i\hbar\sqrt{\kappa}[\mathcal{E}_{in}(t)\hat{a}^\dagger + \mathcal{E}_{in}(t)\hat{a}],\end{aligned}\quad (3.3)$$

where the optomechanical coupling rate  $g_0 = \omega_0 \zeta (\zeta = z_{ZPF}/L_c)$  quantifies the strength of interactions between the optical and the mechanical modes. It is assumed to be the same for all the mechanical oscillators. The radiation pressure force applied to an oscillator is defined as  $\hat{F}_{rp} = (\hbar\omega_0/L_0)\hat{a}^\dagger\hat{a}$  that causes the oscillator displacement and changes the effective cavity length. With the Hamiltonian  $\hat{H}$ , we can write the equations of motion in a frame rotating at the center frequency of the control field as:

$$\dot{\hat{a}} = -(\mathrm{i}\delta + \kappa/2)\hat{a} + \sum_{j=1}^M \mathrm{i}g_0\hat{a}(\hat{b}_j^\dagger + \hat{b}_j) + \sqrt{\kappa}\mathcal{E}_{in}(t), \quad (3.4)$$

$$\dot{\hat{b}}_j = -(\mathrm{i}\omega_j + \gamma_m/2)\hat{b}_j + \mathrm{i}g_0\hat{a}^\dagger\hat{a} + \sqrt{\gamma_m}\hat{\beta}_{in}, \quad (3.5)$$

where  $\delta$  is the frequency detuning of light from the cavity,  $\beta_{in}$  is the noise introduced by the thermal bath satisfying  $\langle \hat{\beta}_{in}(t) \rangle = 0$  and  $\langle \hat{\beta}_{in}(t)\hat{\beta}_{in}(t') \rangle = k_B T \delta(t - t')$ , and  $\gamma_m$  is the thermalization rate of the  $j$ th mechanical oscillator. We assume the mechanical/phonon loss rate  $\gamma_m$  is the same for all mechanical oscillators in the optical cavity. For a single mechanical oscillator with a single-frequency control field, the steady-state solution for the expectation values,  $\langle \hat{a} \rangle = \alpha$  and  $\langle \hat{b} \rangle = \beta$ , can be obtained:

$$\alpha = \frac{\sqrt{\kappa}\mathcal{E}_{in}}{\frac{\kappa}{2} + \mathrm{i}(\delta - g_0\beta)}, \quad (3.6)$$

$$\beta = \hbar\zeta \frac{\alpha^2}{m\omega_m^2}, \quad (3.7)$$

In terms of the coupling between the mechanical oscillators in the optical cavity, we are not ignoring it because the coupling Hamiltonian term between mechanical oscillators is already included in Eq. 3.1. As we have described, to linearize the equations of motion (Eq. 3.4 and Eq. 3.5), We assume the operators,  $\hat{a}$  and  $\hat{b}$ , consist of time-independent (coherent amplitude) terms,  $\alpha$  and  $\beta$ , plus fluctuating terms,  $\delta\hat{a}$  and  $\delta\hat{b}$ , where  $\alpha \gg \langle \delta a \rangle$  and  $\beta \gg \langle \delta b \rangle$ , namely  $\hat{a} = \alpha + \delta\hat{a}$  and  $\hat{b} = \beta + \delta\hat{b}$ . Then the corresponding linearized Hamiltonian first-order term,  $\hat{H}_{OM}$ , for the optomechanical coupling can be described as

$$\hat{H}_{OM} = - \sum_j^M \hbar g_0 (\delta\hat{a}^\dagger + \delta\hat{a}) (\hat{b}_j + \hat{b}_j^\dagger), \quad (3.8)$$

Using the second-order perturbation theory [158], when  $\delta$  (the frequency detuning of light from the cavity) is much larger than the mean mechanical frequency of oscillators,  $\omega_m$ , the direct coupling between mechanical oscillators in the cavity can be simplified expressed as

$$\hat{H}'_{OM} = -\hbar \sum_j^M \frac{g_0^2}{\delta} (\hat{b}_j + \hat{b}_j^\dagger)^2, \quad (3.9)$$

where we assume the optomechanical coupling rate,  $g_0$ , is the same for all the mechanical oscillators. Therefore, we only need to assume that the direct coupling rate ( $\frac{g_0^2}{\delta}$ ) between oscillators is smaller than the global loss rate of mechanical oscillators,  $\gamma_m$ , namely  $\frac{g_0^2}{\delta} \ll \gamma_m$ . The reason is to make sure the optomechanical interaction can occur to store probe light information before mechanical oscillators lose the information of light. We also assume that the initial phonon occupation number is much less than one ( $\beta_{in} \ll 1$ ) that can be achieved by passive cooling to initially prepare the system.

Using the steady-state solutions, we can now linearize the equations of motion by only keeping the first-order terms in the fluctuations. The input drive field can be described as  $\mathcal{E}_{in}(t) = \bar{\mathcal{E}}_{in} + \delta\mathcal{E}_{in}$  with  $\bar{\mathcal{E}}_{in} = \mathcal{E}_c$  and  $\delta\mathcal{E}_{in} = \delta\mathcal{E}_p e^{i\omega_m t} + \sum_{m=-m_s/2}^{m_s/2} \mathcal{E}_c e^{-im\Delta t}$ , where  $\mathcal{E}_c$  is the frequency comb control (read/write) field,  $\delta\mathcal{E}_p$  is a weak probe field,  $m_s$  is a non-zero integer representing the number of control field frequency lines spaced by  $\Delta$ , and  $\omega_m$  is the center mechanical frequency of the frequency comb created by control laser. Using the steady-state solutions for  $\alpha$  and  $\beta$  we arrive at the linearized equations of motion for  $\delta\hat{a}$  and  $\delta\hat{b}$ :

$$\begin{aligned} \dot{\delta\hat{a}} &= -(i\delta + \kappa/2)\delta\hat{a} + ig_0\alpha \int [\delta\hat{b}_\omega(t) + \delta\hat{b}_\omega^\dagger(t)]n(\omega)d\omega \\ &\quad + \sqrt{\kappa}\delta\mathcal{E}_{in}, \end{aligned} \quad (3.10)$$

$$\dot{\delta\hat{b}_j} = -(i\omega_j + \gamma_m/2)\delta\hat{b}_j + ig_0\alpha(\delta\hat{a}^\dagger + \delta\hat{a}), \quad (3.11)$$

where  $n(\omega)$  represents the frequency distribution of mechanical oscillators inside the cavity and  $\delta(\omega - \omega_m - m\Delta)$  accounts for the  $m_s$  control (read/write) field frequency comb lines separated by  $\Delta$ . The interaction of the control frequency comb with the ensemble optomechanics tailors the optomechanical frequency distribution,  $n(\omega)$ , and addresses  $m_s$  mechanical modes



as a subset of the entire mechanical ensemble. Using the solution to the mechanical fluctuations,  $\delta\hat{b}_\omega(t) = \delta\hat{b}_j(t) = \int_{-\infty}^t ig_0\alpha(\delta a^\dagger(t') + \delta a(t'))e^{-(i\omega+\gamma_m/2)t'} dt'$ , we rewrite the above equation for the mean value of the cavity field operator,  $\mathcal{E} = \langle\delta a\rangle = \langle\delta a\rangle^\dagger$ , as [159]

$$\begin{aligned}\dot{\mathcal{E}}(t) = & -(i\delta + \kappa/2)\mathcal{E}(t) - G \int_{-\infty}^t \mathcal{E}(t')e^{-\frac{\gamma_m}{2}t'} n(t-t')dt' \\ & + \sqrt{\kappa}\delta\mathcal{E}_{in}(t),\end{aligned}\tag{3.12}$$

where the coefficient  $G = 4g_0^2\alpha^2$  and  $n(t)$  is the Fourier transform of  $n(\omega)$ . If the total width of the inhomogeneous frequency distribution,  $\Delta\omega$ , is much larger than the mechanical dissipation rate,  $\gamma_m$ , then the exponential  $e^{-\frac{\gamma_m}{2}t}$  can be ignored over the timescales of the absorption. We can approximately write  $n(t-t') \approx \frac{M}{\Delta\omega}\delta(t-t')$  when  $\Delta\omega$  is much larger than the probe bandwidth (for times around  $t=0$ , when the absorption occurs). Therefore,

$$\dot{\mathcal{E}}(t) = -(i\delta + \kappa/2)\mathcal{E}(t) - G'\mathcal{E}(t) + \sqrt{\kappa}\delta\mathcal{E}_{in}(t),\tag{3.13}$$

The solution to the optical field is then  $\mathcal{E}(t) = \int_{-\infty}^t \sqrt{\kappa}\delta\mathcal{E}_{in}(t')e^{-(i\delta+\kappa/2+G')t}dt'$ . Here we defined  $G' = \frac{M}{\Delta\omega}G$ . We can further simplify the above equation to find an analytical solution of the electric field assuming the probe pulse bandwidth is much smaller than the cavity bandwidth  $\kappa$ . In that case, we can adiabatically eliminate the cavity mode and use the cavity input-output relation  $\mathcal{E}_{out}(t) = -\delta\mathcal{E}_{in}(t) + \sqrt{\kappa}\mathcal{E}(t)$  to find an approximate solution for the out-coupled cavity light. We use the transformation  $\mathcal{E}(t) \rightarrow \mathcal{E}(t)e^{-i\omega_m t}$  and the rotating wave approximation to get

$$\mathcal{E}_{out}(t) \approx \frac{\kappa/2 - G'}{\kappa/2 + G'}\delta\mathcal{E}_p(t).\tag{3.14}$$

The coefficient  $G$  mentioned above is considered as the effective optomechanical coupling rate in our system. We note that  $G$  is proportional to  $(g_0\alpha)^2$  where  $\alpha$  can be understood as the coherent amplitude resulted from the interference between the broadband weak probe field,  $\delta\mathcal{E}_p(t)$ , and the control (write/read) field,  $\mathcal{E}_c(t)$ , with multiple frequency comb lines, as indicated in Eq. 3.6. In this regime, one can see that  $\mathcal{E}_{out} = 0$  when  $\kappa/2 = \frac{M}{\Delta\omega}G$  the input

light is fully absorbed by the mechanical oscillators inside the optical cavity. The above equation approximately describes the “write” process for our optomechanical frequency comb system. Since Eq. 3.13 is identical to the equation of motion for the atomic frequency comb in a cavity, the reading process can also be analytically described similar to the case of the atomic frequency comb storage [160]. The analytical solution is only an approximate description of the system dynamics. We now carry out numerical simulations of Eqs. 3.4 and 3.5 without further approximations, using multi-dimensional differential equation simulator (XMDS) [161]. We consider an optical pulse matched to the cavity spectrum interacts with an ensemble of  $M = 100$  oscillators with the frequency spectrum of width on the order of  $\Delta\omega_m = 0.01\omega_m$  that is tailored using a control laser with  $m_s$  frequency lines. We use a control (read/write) laser shaped into a frequency comb that is off-resonance and red-detuned from the cavity to engineer the interaction between the probe light, which is resonant with the cavity, and a subset of  $m_s$  oscillators with the frequency space of  $\Delta$  in the mechanical oscillator array with total  $M$  mechanical oscillators ( $m_s \leq M$ ). The optomechanical interaction, in this case, mainly occurs when the probe-control frequency difference is equal to the mechanical frequencies of one or more oscillators (making up the subset with  $m_s$  oscillators mentioned above), thus multiple comb lines of the control light create an optomechanical frequency comb. With the interference of the probe and writing pulses, the probe pulse is fully mapped and its information is stored as the mechanical excitations onto this subset of  $m_s$  mechanical oscillators with an equally spaced frequency of  $\Delta$ . Because the relative phase between the neighboring excited mechanical oscillators in this subset matches at time intervals of  $2\pi/\Delta$ , the read laser is sent into the optical cavity after a time  $2\pi/\Delta$  to retrieve the stored information (mechanical excitations) from the subset of oscillators.

### 3.3 Optomechanical Frequency Comb for Storing Light Information

The mechanical modes are in fact distributed randomly. We consider many mechanical modes (oscillators) in the optomechanical system forming a wide mechanical frequency distribution with a width of  $\Delta\omega_m \approx 1\%\omega_m$ , where  $\omega_m$  is the center mechanical frequency.

The frequency spacing  $\Delta$  is the spacing between the subset of the oscillators selectively addressed by the control laser (read/write) from the entire ensemble of the oscillators. We also consider an optomechanical array consisting of  $M = 100$  mechanical modes (oscillators) with random frequencies around  $\omega_m$ , a frequency distribution width around  $1\%\omega_m$ , and a subset of  $m_s = 3 - 21$  oscillators to perform storage. In Fig. 3.2, we plot the optical and mechanical excitations as a function of time, demonstrating the coherent transduction of an optical pulse to phonons that echo at precise time intervals. For a probe pulse and  $m_s = 5, 7, 11$  control comb lines, a subset (5, 7, 11) of mechanical modes within the spectrum are

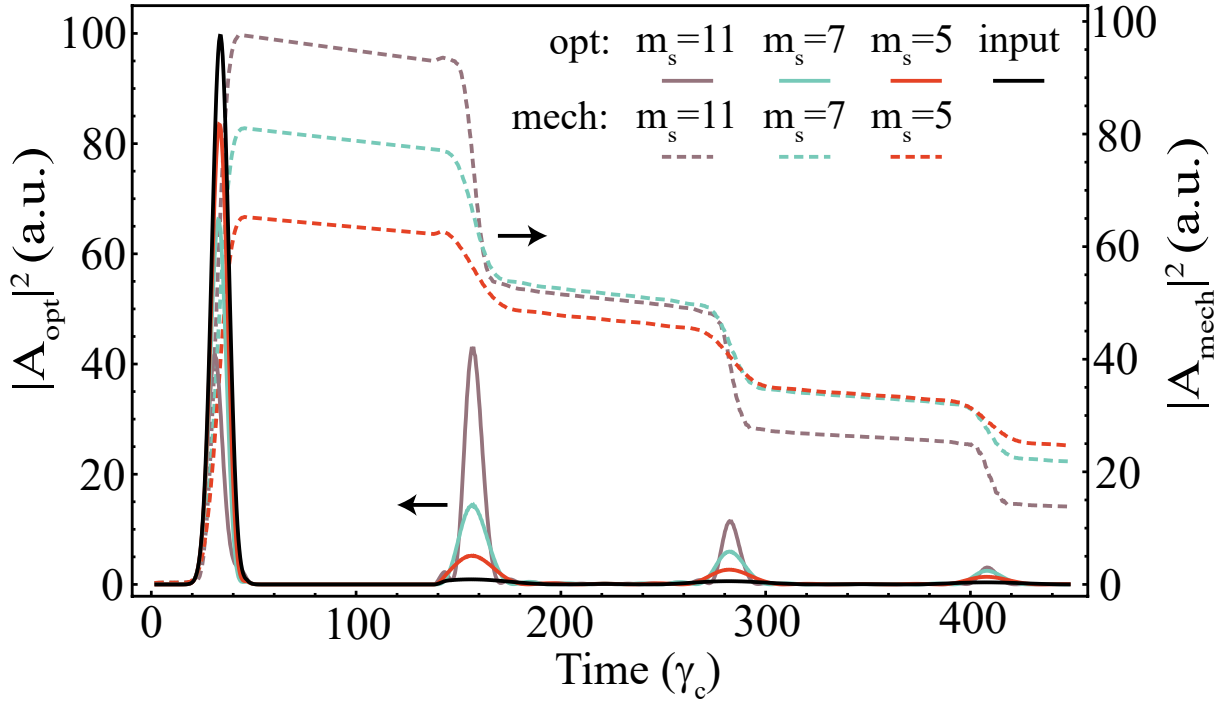


**Figure 3.2.** Amplitude of the optical ( $A_{opt}$ ) and mechanical ( $A_{mech}$ ) excitations are plotted as a function of the normalized time. A probe pulse (black curve) impinging on the cavity together with a write laser create mechanical excitations that echo after a time of  $2\pi/\Delta$ . The photon-phonon echo intensities from the subset of ensemble with mechanical oscillators as low as eleven (solid purple), seven (solid green) and five (solid red) are shown (left axis). The corresponding collective mechanical excitations are indicated with dashed lines (right axis). A normalized optomechanical coupling rate of  $g_0^2/\kappa\gamma_m = 10^{-3}$ , thermalization rate  $\gamma_m/\kappa = 0.001$ , mechanical dephasing/rephasing rate  $\Delta/\kappa = 0.05$ , center mechanical resonant frequency  $\omega_m/\kappa = 10$ , and the total number of mechanical oscillators  $M = 100$  are used in this simulation.

collectively excited, storing the probe information. If a control laser is present when the phase-matching condition is satisfied, a photon echo is generated from the phonon echo. If, however, no control laser is applied, the mechanical excitations keep dephasing and rephasing at a rate of  $\Delta$  until the control light is applied or they are lost through coupling to the thermal bath. The storage efficiency here is the ratio of echo intensity after a time of  $2\pi/\Delta$  to the input (probe) light intensity. As the storage and retrieval efficiencies are symmetric, at finite storage efficiencies the left-over mechanical excitations after the first echo give rise to the multiple photon echoes at  $2\pi/\Delta$  time intervals. Below, we investigate the role of various parameters in the memory performance using the numerical simulation.

Fig. 3.3 (a) shows that the storage efficiency drops as the center frequency ( $\omega_m$ ) of the mechanical excitations increases. This is because the optomechanical coupling rate ( $g_0$ ) drops with the square root of the mechanical frequency. Apart from the storage efficiency, we calculate the signal-to-noise ratio (SNR) of the output echo. SNR is defined as the ratio of output echo intensity to the mean intensity of output fluctuations which are mainly attributed to the control laser introducing mechanical heating that appears as modulation of the echo signal at frequency  $\omega_m$ . These fast fluctuations at the mechanical frequency that is greater than the bandwidth of the probe pulse can be filtered by reducing the measurement bandwidth. The SNR enhances with the increase of  $\omega_m$  as we approach the resolved sideband regime and there is less residual heating. Fig. 3.3 (b) shows the effect of control field intensity on the storage efficiency and SNR. Here we plot the efficiency and SNR vs. the control field cooperativity defined as  $C_c = 4g_0^2 n_c / \kappa \gamma_m$ , where  $n_c$  is the mean photon number of the control light. The enhancement in the storage efficiency at low control field power ( $C_c < 1$ ) is explained by the fact that the effective optomechanical coupling strength is proportional to the control field amplitude. As the control cooperatively approaches one, the system enters the parametric amplification regime [140]. Moreover, one observes higher storage efficiency for narrower inhomogeneous broadenings while the SNR remains unchanged. The proposed storage protocol relies on the interaction of light with multiple mechanical modes by selectively addressing a subset of mechanical modes out of the entire ensemble of oscillators. A single mechanical oscillator can not be used to store light in this manner, however, using other protocols like single electromagnetically induced transparency (EIT), light

storage can be achieved in a single mechanical oscillator [39]. Fig. 3.3 (c) demonstrates the ensemble effect on the storage efficiency and SNR. The subset of  $m_s$  oscillators, addressed by the frequency-comb control laser out of  $M = 100$  total oscillators, collectively store light. The enhancement in the storage efficiency at high  $m_s$  numbers is limited by the optical cavity bandwidth. When the memory bandwidth,  $m_s\Delta$ , approaches the cavity linewidth, the efficiency enhancement reaches a plateau. At large  $m_s$  numbers, the memory performance

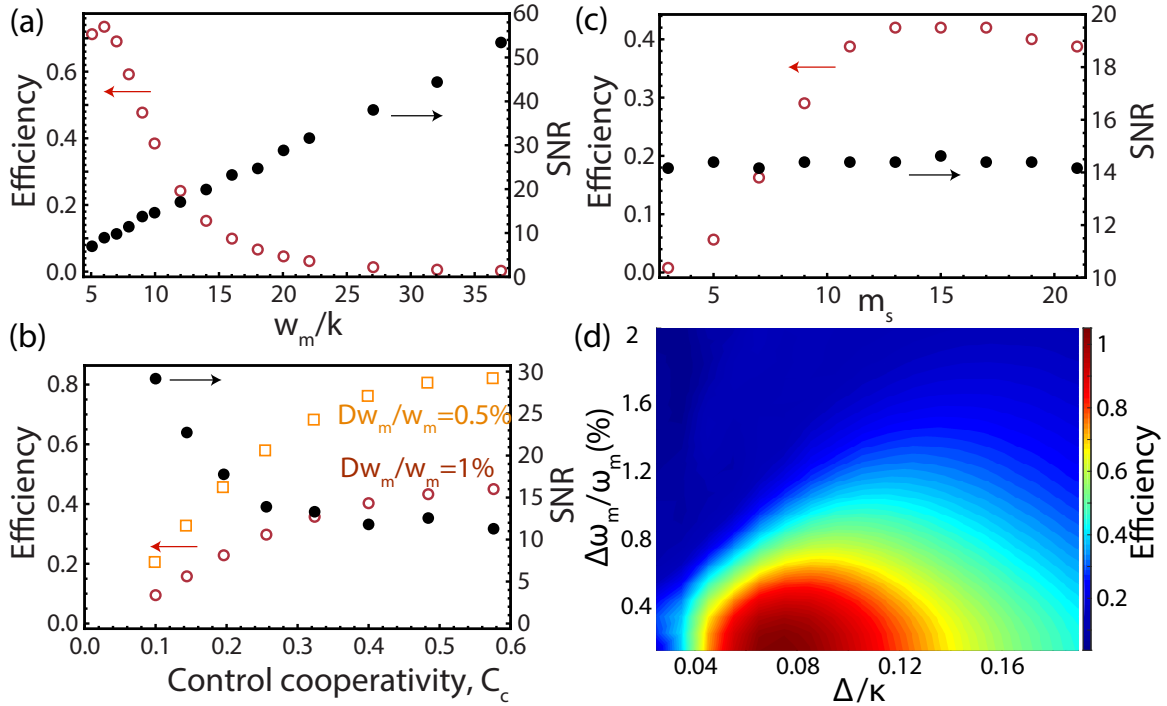


**Figure 3.3.** The storage efficiency (open circle) and the signal-to-noise ratio (filled circle) of the optomechanical array memory as a function of (a) the normalized center frequency ( $\omega_m$ ) of the mechanical excitations as  $m_s = 11$ , (b) the control cooperativity,  $C_c = 4g_0^2 n_c / \kappa \gamma_m$ , where  $n_c$  is varied, for inhomogeneous broadening  $\Delta\omega = 1\%w_m$  (open circle) and  $\Delta\omega = 0.5\%w_m$  (open square) as  $m_s = 11$ , (c) the number of mechanical oscillators ( $m_s$ ), which are addressed by the control field out of  $M = 100$  total oscillators, and have frequency spacing of  $\Delta = 0.05\kappa$ , and (d) the storage efficiency as a function of the normalized optomechanical spectral width  $\Delta\omega_m/\omega_m$  and frequency spacing  $\Delta/\kappa$  of the tailored optomechanical spectrum, where  $m_s = 11$  and  $C_c = 0.4$  are used for the simulation while the other parameters are the same as the ones used in Fig. 3.2

can be further improved by varying the comb spacing,  $\Delta$ . Similar to the atomic frequency comb, the unity storage efficiency is feasible in the current approach. Fig. 3.3 (d) describes the storage efficiency as a function of the normalized optomechanical spectral width  $\Delta\omega_m$  and frequency spacing of the tailored optomechanical spectrum. It can be seen that with total inhomogeneous broadening below 1% of  $\omega_m$  the storage efficiency close to unity can be achieved. In this case, the SNR of about 15 was achieved using realistic numbers. We note that what we refer to as noise in the retrieval signal is in fact fast oscillations (at well-known frequencies about  $\omega_m$ ) on top of a slowly varying probe signal that can be filtered by reducing the measurement bandwidth provided. Due to the large mechanical frequency of the oscillators, a measurement bandwidth on the order of the cavity linewidth ensures a low contribution of noise while maintaining reasonable detection bandwidth on the order of the probe bandwidth. We note that the simulation parameters used to plot Fig. 3.3 (d), namely the coupling strength  $g_0^2/\kappa\gamma_m = 10^{-3}$  and the mechanical quality factor of  $Q_m = 10^4$ , are achievable in the state-of-the-art optomechanical systems [140]. The most important aspect of the multimode memory considered here is its ability to store light with large delay-bandwidth products. Although a single double-beam oscillator integrated into a photonic resonator can exhibit higher optomechanical coupling [162],  $\omega_0/L_c > 100$  GHz/nm, compared with an oscillator array integrated into a resonator, the delay-bandwidth product of storage achieved with a single oscillator is at most one. Compared with a single oscillator used for light storage, the proposed memory protocol here offers much larger values of delay-bandwidth products as is the case in the atomic frequency comb memories. As we see from Fig. 3.3, the memory performance depends on both the number of oscillators,  $M$ , and the spectral density. Since here we assume the thermalization rate  $\gamma_m$  is the same for all the  $M$  mechanical oscillators considered in the optical cavity, as long as  $M \times \gamma_m \gg \Delta\omega_m$ , up to  $\Delta\omega_m/\Delta$  mechanical modes can be selected out of the total  $M$  modes as the subset of oscillators using the control (write/read) laser. This provides a storage bandwidth of  $\Delta\omega_m$ . The enhancement of the memory storage efficiency is limited by the optical cavity bandwidth at higher  $m_s$  numbers. At the large  $m_s$  numbers, the memory performance can be improved by varying the frequency spacing ( $\Delta$ ). This is the remarkable advantage of the frequency comb storage technique allowing to use the inhomogeneous broadening in the system to perform

the on-demand storage. The proposed optomechanical system still works if the light state is the superposition of  $A|0\rangle$  and  $B|1\rangle$ , here  $|0\rangle$  and  $|1\rangle$  are Fock states of the light. Our optomechanical memory requires cooling the mechanical oscillators near their quantum ground states. At very low temperatures like 50mK, the mean phonon number of the system would be less than 1, so the considered optomechanical frequency comb memory still can store photon information onto the mechanical oscillators with less noise.

In the proposed scheme, the thermal excitations, which are detrimental to the quantum light storage and ignored in the current study, can degrade the memory performance by introducing both phase and amplitude noise to the output echo. Although the coherent storage of a classical signal using room-temperature optomechanical systems can be obtained [39], the storage in quantum regime requires cooling the mechanical oscillators near their quantum ground states (QGS). The current system relies on the ensemble of oscillators with large mechanical frequencies for light storage. In the limit of  $\omega_m \gg \kappa$ , the control laser (read/write beam) acts as the cooling beam actively reducing the thermal phonons before the storage process. Thus, an extra cooling laser in our proposal is not required. Moreover, low phonon numbers can be achieved by passive cooling of the optomechanical chip thanks to the low phonon occupation number at the large mechanical frequencies. For example, the mean phonon number ( $N_p = k_B T / \hbar \omega_m$ ) of the optomechanical system is around 5 at 4K and 1 at 50mK, respectively, if  $\omega_m = 1\text{GHz}$ . Therefore, a combination of passive and active cooling may enable broadband quantum light storage on a chip with large delay bandwidth products. Also, it has been demonstrated that, even near the room temperature, the mechanical excitations created by a weak optical signal can be extracted from the optomechanical system using the interferometric measurements canceling the background signal from the thermal noise [163]. In the case of the collective optomechanical interactions considered here, although the thermal excitations directly excite the mechanical modes to the upper excited energy state of the system and therefore introduce phase and amplitude noise to the retrieved photon-phonon echo mode, they are not phase-matched to the photon-phonon echo. Using interferometric detection, the thermal noise can be subtracted with higher efficiency in the case of collective coupling compared to the single oscillator case. In this way, one can perform a type of lock-in detection, where the quantum correlation inverts

whereas thermal correlations remain unchanged. Using this detection method, it might be possible to reduce the effect of the thermal noise on the stored quantum optical signal even near room temperature. The lock-in-type detection of this kind enables, in principle, the study of quantum optomechanical interactions outside the QGS.

### 3.4 Merit of Proposed Optomechanical Memory System

The light storage protocol in atoms relies on mapping optical coherence into atomic spin coherence that can be fairly decoupled from the thermal noise. The thermal noise in this context will appear as collisional decoherence and direct excitation of atoms between the hyperfine states. In the optomechanical memories, however, the effect of thermal noise is more direct as it increases the thermal phonons. The main merit of the proposed scheme compared with the atomic systems is not to achieve a room-temperature optomechanical memory but to realize the collective optomechanical interaction over a wide wavelength range (100s of *nms*) that can be used for broadband light storage. Another advantage is that the proposed system is not bound to a particular atomic transition. The solid-state atomic memories are generally required to operate at cryogenic temperatures to realize the long-lived quantum storage. For example, to achieve light storage for a few microseconds in rare-earth-doped crystals, the operating temperature needs to be below 4 K. Although the optomechanical systems also require cryogenic cooling, their room-temperature operation can be envisioned for some applications. It has been demonstrated that a weak optomechanical signal can be extracted from a room-temperature oscillator using interferometric detection canceling the effect of the thermal noise [163]. In the current optomechanical system, the random phase of the thermal excitations suggests that they are not phase-matched to the photon-phonon echo. This means that using the interferometric method, a weak optical signal buried under thermal noise can be extracted with a high signal-to-noise ratio from the current optomechanical memory. In this way, one can perform a type of lock-in detection, where the quantum correlation inverts whereas thermal correlations remain unchanged, reducing the contribution of the thermal noise.



### 3.5 Potential Realization of Proposed Optomechanical Comb Memory

We envision the implementation of the proposed optomechanical system in a single photonic resonator on a chip. Relying on the optical gradient forces [162], multiple slot-waveguide optomechanical resonators can be fabricated in a silicon photonic race-track resonator with high mechanical frequencies and reasonably high optomechanical coupling strengths [164]. Such gradient force with effective cavity length,  $L_c$ , exponentially dropping with the gap size, is the key to achieving ultra-high optomechanical coupling strengths [137]. Although a single double-beam oscillator integrated into a photonic resonator can exhibit higher optomechanical coupling [162],  $\omega_0/L_c > 100$  GHz/nm, compared with an oscillator array integrated into a resonator, the delay-bandwidth product of storage achieved with a single oscillator is at most one. The collective optomechanical interactions considered in this work enable storage with large delay-bandwidth products while the large oscillator number can compensate for the relatively low optomechanical coupling.

Moreover, the scaling, in this case, is similar to the atomic systems. Although a single atom trapped in a high-Q cavity with a small mode volume enables strong light-atom interactions much higher than those for an ensemble of atoms in a lower Q cavity, in practice it is easier to work with the ensemble of atoms. In particular, as we are interested in light storage which is a linear process, we do not require nonlinear interaction strength provided by the large single-particle cooperativity in high Q cavities. The strong interaction of light with a single particle creates a large nonlinearity that is useful for quantum applications such as logic operations, however, it is not needed for the storage process proposed here and in fact it is the regime that should be avoided for pure light storage. More importantly, the multimode properties offered by the ensemble proposed in this work enable multimode and large delay-bandwidth storage as discussed earlier.

### 3.6 Summary

In conclusion, we study controllable dynamics of optomechanical interactions in an array that can efficiently store light over a wide wavelength range. Using a write laser tailoring the inhomogeneously-broadened spectrum of a mechanical resonator ensemble inside an optical

cavity, the information of the probe light can be stored as mechanical excitations with the help of the interference between the write laser and the probe pulse. The stored information is retrieved with high efficiency by the read laser after a multiple of time  $2\pi/\Delta$ , when all mechanical oscillators are phase-matched. The interaction scheme overcomes the current limitation in preparing identical optomechanical arrays enabling observation of large-scale cooperative optomechanical effects. The results of this study may initiate more investigations of the cooperative optomechanical coupling, many-body dynamics, and long-range optomechanical interactions. The proposed method will provide a new way to enhance and externally control the optomechanical interactions for coherent light storage, multimode sensing, and optomechanical transduction applications as well as to study the many-body dynamics in optomechanical systems such as long-range phonon dynamics in the optomechanical array.

## 4. SUPERCONDUCTING LEVITATION OF A MG-SCALE CAVITY MIRROR

Motivated by the idea of building an optical cavity using the milligram scale mirror levitated by superconductor at low temperatures, we characterized the mechanical properties of the superconducting levitated mirror and applied it for magnetic field sensing applications. A large portion of the work described in this chapter is the reproduction of the previously published work [165], with the permission of AIP Publishing.

### 4.1 Introduction

Reducing the mechanical clamping loss is a great challenge in optomechanical systems [166]. Clamping loss can be removed through levitation via optical tweezer traps [167]–[169], radio frequency (RF) traps [170], [171] and magnetic traps [14], [75], [76], [172]. However, the lack of coherent control in these traps of macroscopic objects limits the mechanical properties and thus results in loss of information through, for example, scattering loss (in the case of optical tweezers) or induced noise from the trapping electrodes or magnets (in the case of RF or magnetic traps) [70]. It was proposed that scattering loss can be eliminated using coherent optical trapping of a cavity mirror [173]. Towards this goal, an optically levitated nanosphere has been shown to be cooled to its quantum ground state by coherent scattering [68]. The magnetic traps, on the other hand, offer a flexible tool to trap objects while inducing relatively small mechanical noise [14]. Observation of quantum mechanical effects have also been predicted in these systems [74], [76], [174]. Moreover, levitated micro-size magnetic particles using Meissner effect have also been experimentally used for the ultrasensitive acceleration [14], force [175] and gravimetry [15] sensing.

In this chapter, we propose and experimentally study a hybrid levitation platform based on superconducting levitation of a cavity mirror. We characterize the mechanical properties and magnetic sensing sensitivity of the levitated mirror. We observe a magnetic (B) field sensitivity of  $370 \text{ pT}/\sqrt{\text{Hz}}$  by measuring the magnetic torque applied to the mirror. We also build a Fabry-Pérot resonator with the levitated mirror as the end mirror of the cavity. The

optical spring effect of the intra-cavity field can, in principle, provide a 1D coherent optical trap of the mirror, self-locked along the cavity axis while the trapping in the other directions is provided by the magnetic trap.

## 4.2 Hybrid Superconductor Levitation Platform

The experimental setup scheme is shown in Fig. 4.1. The high-reflectivity ( $R > 99.8\%$ ) coated dielectric small mirror with a diameter of  $d = 2\text{mm}$ , a mass of  $m_r = 6\text{mg}$ , and thickness of  $t = 1\text{mm}$  is attached to one small neodymium(Nd)-based magnetic disk which has the same dimensions as the mirror and a mass of  $m_n = 24\text{ mg}$ . The YBaCuO superconductor (SC) disk with a diameter of  $2.5\text{ cm}$  and critical temperature of  $\sim 93\text{K}$  is placed inside a cryogenic system (ST-500 from Janis) and cooled down to  $77\text{K}$  using cyclic liquid nitrogen. The mirror attached to the small magnetic disk is levitated  $3.2\text{ mm}$  above the SC disk outside the cryostat, as shown in Fig. 4.1. The  $850\text{nm}$  light of a Ti-sapphire laser is used to sense the mirror's position via a quadrant detector and also study the optical resonance of the levitated cavity-end mirror. To calibrate the magnetic field sensing, we place a 15-turn coil with a diameter of  $3\text{ cm}$  above the levitated mirror and modulate its current at different frequencies and amplitudes. The main B-field of the coil near the mirror is along the vertical direction introducing a torque on the mirror. We use a quadrant detector to detect the reflected light from the levitated mirror and measure the mirror's vibrational noise in two directions.

## 4.3 Theoretical Calculation of Superconductor Levitation based on Frozen-image Model

To theoretically calculate the resonant frequencies of the levitated small mirror, we use the frozen-image model [82], [176] depicted in Fig. 4.2. We approximate the magnetic disk with the attached mirror as a magnetic dipole ( $d$ ). In this case, the magnetic flux pinning effect is expected to occur giving rise to the levitation of the magnet. The interaction between  $d$  and its frozen and diamagnetic images  $d'$  and  $d''$  (see Fig. 4.2), respectively, is sufficient to approximately describe the dynamics [82], [176]. The effective magnetic moment ( $m_{lev}$ )

of the levitated disk makes an angle  $\theta'$  with the vertical direction,  $z$  axis in Fig. 4.2, which can be different from the angle of the frozen dipole  $\theta = \theta' - \delta\theta$ , where the deflection angle  $\delta\theta$  is caused by the inhomogeneity of the superconductor disk's field, external magnetic field and gravitational torque applied by the mirror.

Taking the center of mass (CM) of the levitated magnet as the origin of the coordinate system, the magnetic field ( $B_{lev}$ ) that the dipole  $d$  imposes to  $d'$  can be calculated as:

$$B_{lev} = \frac{\mu_0}{4\pi} \left[ \frac{3(m_{lev} \cdot r)r}{r^5} - \frac{m_{lev}}{r^3} \right] \quad (4.1)$$

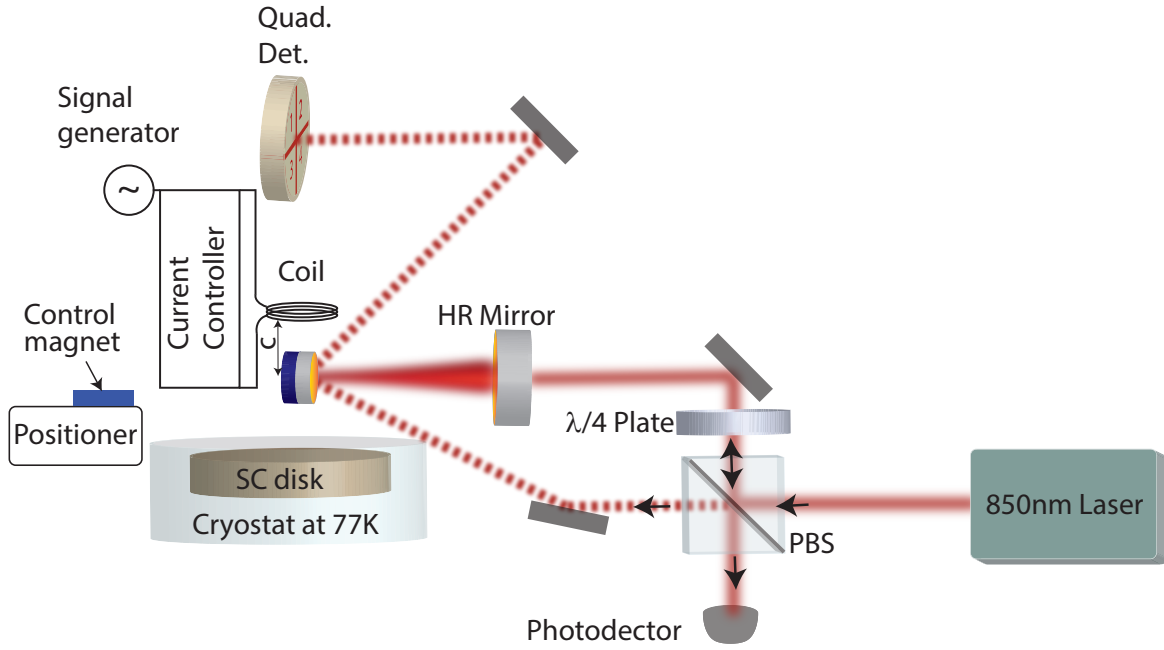


**Figure 4.1.** Experimental setup for a cavity mirror magnetically levitated and optically probed. The vibration of a magnetic mirror levitated above a superconductor (SC) disk is monitored using a quadrant detector (quad. det.). Also, the levitated mirror together with the fixed HR mirror (reflectivity of  $\sim 98\%$  and radius of 25cm) form an optical cavity. The current controller controls AC and DC current in the coil down to a few hundreds of  $nA$  in order to calibrate the response of the mirror to the external magnetic field.

where  $\mu_0$  is the vacuum permeability. The corresponding potential energy due to the interaction between  $d$  and  $d''$  can be written as

$$U_{dia} = \frac{\mu_0 m_{lev} m_{dia}}{4\pi} \left[ \frac{1 + \cos^2(\theta)}{8z^3} \right]. \quad (4.2)$$

Similarly, the potential energy due to the interaction between  $d$  and the frozen image  $d'$ ,  $U_{frz}$ , can be written as

$$U_{frz} = \frac{\mu_0 m_{lev} m_{frz}}{4\pi} \left\{ \frac{P(x, y, z, \theta', \alpha)}{[x^2 + y^2 + (z+h)^2]^{5/2}} \right\}, \quad (4.3)$$

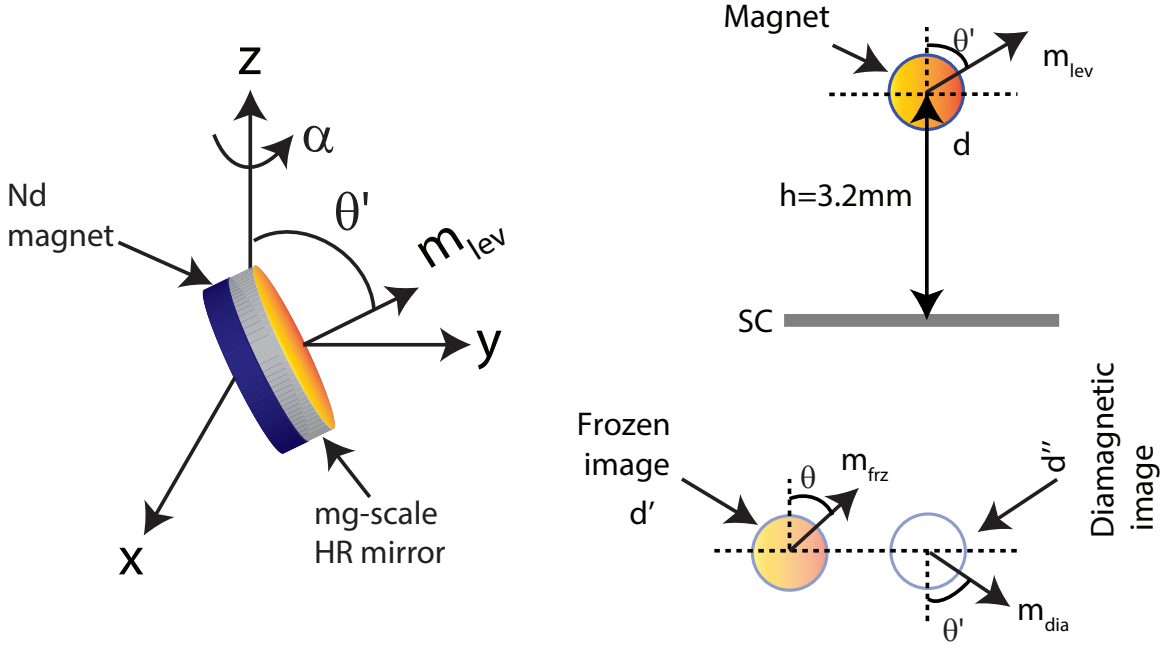


**Figure 4.2.** The model describes the frozen and diamagnetic images based on the interaction between the levitated magnetic mirror and the SC disk, which is used to calculate the mechanical modes.

where  $h$  is the trapping height,  $m_{dia}$  and  $m_{frz}$  are the effective magnetic dipole moments of the diamagnetic and frozen images, respectively.

$$\begin{aligned}
P(x, y, z, \theta', \alpha) = & (z + h)^2(1 - 3 \cos^2(\theta')) + y^2(1 - 3 \sin^2 \theta' \sin^2 \alpha) + x^2(1 - 3 \sin^2 \theta' \cos^2 \alpha) \\
& - 6xy \sin^2 \theta' \cos \alpha \sin \alpha - 6x(z + h) \sin \theta' \cos \theta' \cos \alpha \\
& - 6y(z + h) \sin \theta' \cos \theta' \sin \alpha,
\end{aligned} \tag{4.4}$$

Using the total potential energy,  $U_t = U_{frz} + U_{dia}$ , the stiffness matrix elements can then be derived using  $K = \nabla^2 U_t$  as

$$k_x \simeq \frac{\mu_0 m_{lev}^2}{4\pi} \left[ \frac{3 - 21 \cos(2\delta\theta)}{64h^5} \right], \tag{4.5}$$

$$k_y \simeq \frac{\mu_0 m_{lev}^2}{4\pi} \left[ \frac{-3 + 15 \sin^2(\delta\theta)}{32h^5} \right], \tag{4.6}$$

$$k_z \simeq \frac{\mu_0 m_{lev}^2}{4\pi} \left[ \frac{15 - 9 \sin^2(\delta\theta)}{8h^5} \right], \tag{4.7}$$

$$k_\theta \simeq \frac{\mu_0 m_{lev}^2}{4\pi} \left[ \frac{1 - 3 \cos(2\delta\theta)}{4h^3} \right], \tag{4.8}$$

where we consider  $m_{lev} = m_{dia} = m_{frz}$ , and assume  $x = y \simeq 0$ ,  $z \simeq h$  due to the fact that the release point and trapping point of the levitated magnet are close based on the experimental observations. We also set  $\theta = 90^\circ$ ,  $\alpha = 0^\circ$  for the mirror using a nanopositioner carrying a permanent magnet. We note that there is a range of  $\delta\theta$  within which the restoring force along  $x, y, z, \theta$  can be achieved. The resonant oscillation frequencies of the levitated mirror can vary depending on the exact condition under which the mirror is released, before being trapped above the superconductor. To experimentally verify  $\delta\theta$ , we observe the stable trapping angle of the magnet without the mirror attached and external magnetic field, which shows a minimum  $\delta\theta \sim \pi/4$ .

The magnetic moment of the levitated magnetic disk,  $m_{mag} \simeq 0.003 \text{ A m}^2$ , is calculated based on the measured field on its surface. The magnitude of  $m_{lev}$  is not necessarily the same as  $m_{mag}$  because the magnetic flux pinning effect occurs in a limited-size superconductor. We estimate that there is about 87% of the magnetic field from the levitated Nd-based magnetic disk trapped in the SC disk, i.e.  $m_{lev} = 0.87m_{mag}$ . The calculated oscillation frequencies of

the trapped mirror for  $h = 3.2$  mm are plotted in Fig. 4.3. Assuming a deflection angle of about  $\pi/4$ , then the oscillation frequencies along  $x, y, z$ , and  $\theta$  are approximately 9, 15, 45Hz and 83Hz, respectively. This prediction qualitatively agrees with the measurement done by the quadrant detector, which will be described in detail in Section 4.4.

#### 4.4 Experimental Characterization of Superconductor-levitated Mirror

The experimental oscillation spectra of the levitated mg-scale mirror measured by quadrant detector by subtracting the left-right (horizontal) or top-bottom (vertical) pixels are shown in Fig. 4.4. The top-bottom mode achieved by subtracting the quadrant detector's vertical pixels should have the highest sensitivity to  $f_\theta$ . At a deflection angle of about  $45^\circ$  the calculated values of frequencies approximately match the measured values indicated by the shaded regions on the spectrum of Fig. 4.4. The small discrepancy between the theoretically calculated and experimental oscillation frequencies about the  $x, y, z$ , axes, and  $\theta$  direction could be because we assume the magnet to be a point-like dipole which given its size

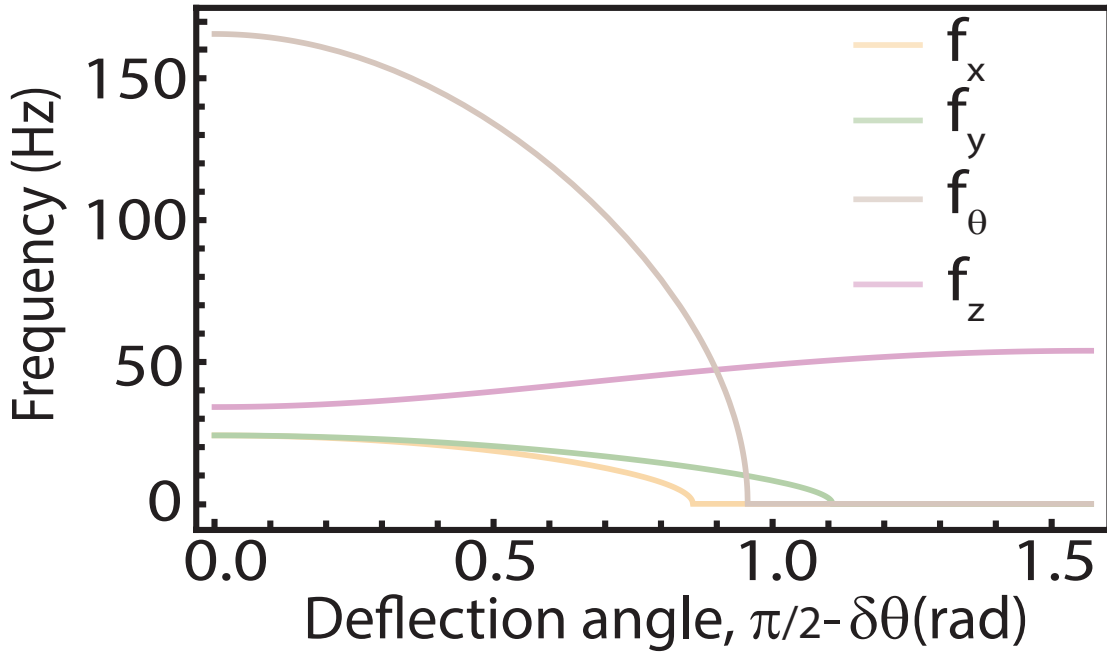


**Figure 4.3.** The calculated values of resonant frequencies of the levitated mirror



relative to the levitation height is not quite accurate. Moreover, the inaccurate estimation of initial and final levitation locations and angles of the levitated magnet, the background magnetic field, and the hysteresis effect [176] in the SC disk make it difficult to accurately quantify the trapping frequencies of the levitated cavity mirror. The oscillation frequencies of the levitated magnetic mirror are very sensitive to its initial angle ( $\theta$ , defined between the magnetic moment of levitated magnetic disk and z axis) and orientation. Different angles and orientations will slightly change the oscillation frequencies once the magnetic mirror is levitated, as the theoretical results show in the inset of Fig. 4.3. Also, the frequencies of the oscillation are very sensitive to the location and height of the levitation. Moreover, the commonly used theoretical frozen-image model we used in predicting the resonant frequencies of the levitated mirror does not consider the hysteresis in the superconductor disk. This could be another reason why we don't expect this model to quantitatively predict the oscillation frequencies in our dynamic measurement where the hysteresis could be more effective. The magnetic trap is shallow and such a shallow trap is susceptible to the low-frequency noise from the environment. The strong 60Hz noise from the vacuum pump dominating the spectra is close to the expected  $f_z$  frequency. We have tried to take data with the pump off, but unfortunately, in that situation, the levitated magnetic cavity mirror would become less stable due to the small fluctuations of temperature induced by the small leakage from the vacuum chamber where the superconductor (SC) is cooled, which is technically limited by our cryogenic system. And because of this leakage, the temperature of SC will rapidly increase, which makes the trapping of the levitated magnetic cavity mirror unstable. The low-frequency noise of the environment including the 60Hz noise from the vacuum pump can be significantly reduced by switching the pump off when a closed-cycle cryostat is used. We have recently acquired an ultra-low vibrational closed-cycle cryogenic system which is more stable than the current one with the vibrational noise on the order of a few nanometers while the vibration from the vacuum pump is completely eliminated. Also by placing both cavity mirrors in vertical configuration inside the vacuum chamber of the cryostat, where the vibrational noise will be common-mode between both mirrors, the relative fluctuations in cavity length can be reduced. Such modification can greatly improve our ability to ob-

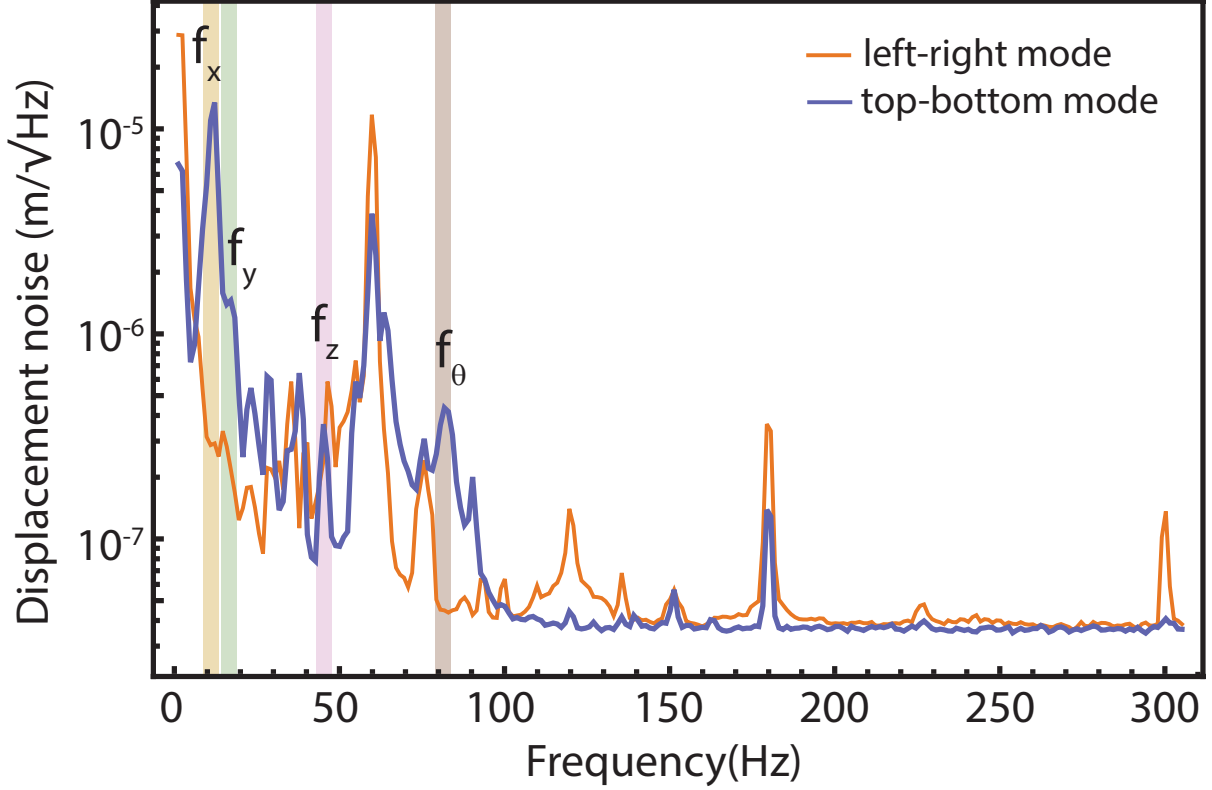


**Figure 4.4.** The vibration spectra of the levitated mirror captured by the quadrant detector by subtracting the left-right (horizontal) or top-bottom (vertical) pixels. At a deflection angle of about  $45^\circ$  the calculated values of frequencies approximately match the measured values indicated by the shaded regions on the spectrum plot.

serve various trapping frequencies and sensing signals. The other vibrational frequencies are indirectly measured by the quadrant detector.

#### 4.5 AC Magnetic Field Sensing Using Levitation Mirror

To confirm the sensitivity measurement to  $f_\theta$ , we also measure the peak vibration intensity as we modulate the magnetic field (B field) at different frequencies using a nearby coil. The coil is positioned right above the levitated mirror separated by distance  $c$  from the coil, and the B field of the coil is along the  $z$  axis. The modulating magnetic torque applied to the levitated mirror causes the oscillations of  $\theta$ , which is measured using the top-bottom mode of the quadrant detector placed at the same height as the mirror. Fig. 4.5 shows the signal

to noise ratio (SNR) of the vibrational intensity as a function of the modulation frequency. According to Fig. 4.5, the SNR peaks at around 90Hz, in agreement with the theoretically predicted  $f_\theta$ .

The high sensitivity of the levitated mirror and detection scheme to the vertical B field along  $z$  axis can be used to estimate the magnetic field sensitivity of the mirror. This is achieved by varying the magnitude of the magnetic field at 90Hz to calibrate the SNR. When the coil is close to the levitated magnetic disk ( $c = 3mm$ ), the linear dependency of the vibration amplitude to the applied B field (inset of Fig. 4.5) could be observed, enabling deduction of the minimum detectable field. To calibrate the B-field sensing, we measure the quadrant detector signal at different coil currents, calculate the applied AC magnetic field from the coil and find the minimum magnetic field corresponding to the amplitude SNR=1.

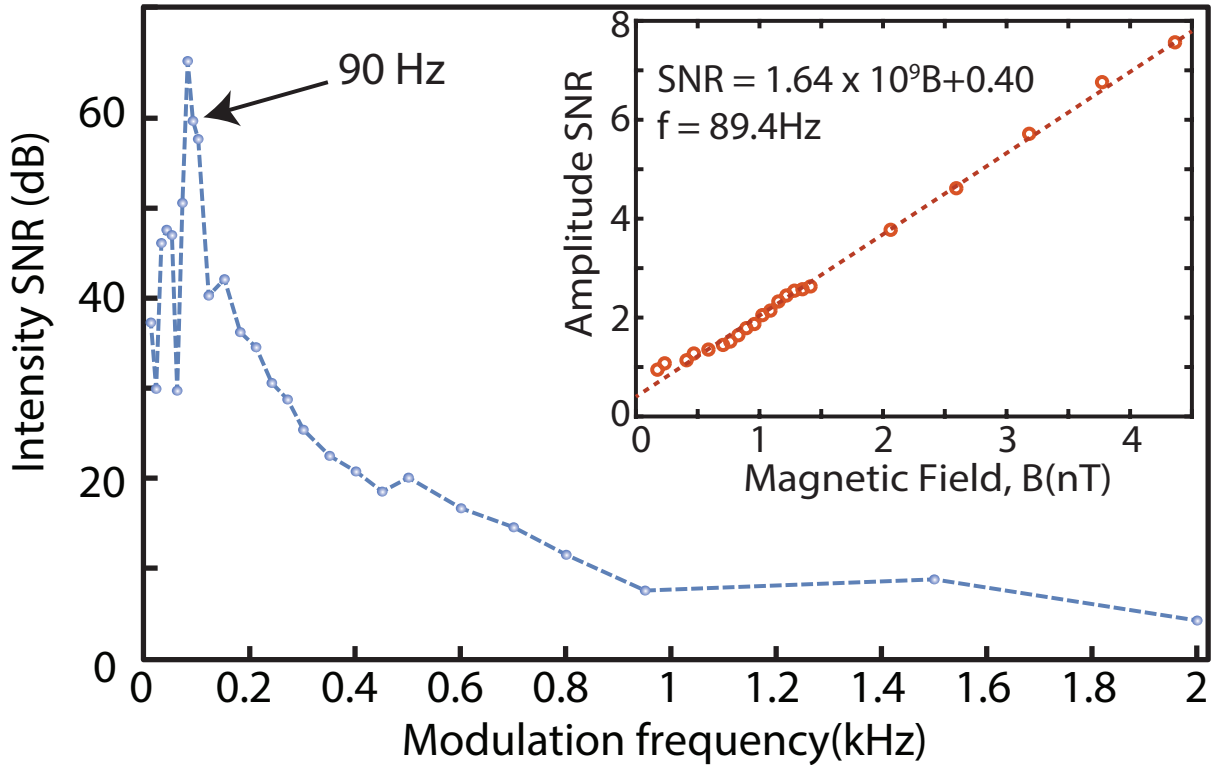


**Figure 4.5.** The peak vibrational intensity (normalized to the background noise) or signal to noise ration (SNR) is plotted at different applied modulation frequencies. Inset shows the measured peak vibrational intensity normalized to the electronic noise (i.e., SNR) as a function of the applied magnetic field for the modulation frequency of  $f \simeq 90\text{Hz}$ .

The maximum sensitivity of the levitated mirror in measuring the magnetic field is then found to be  $370 \text{ pT}/\sqrt{\text{Hz}}$ .

We also compare our magnetic field sensor (the superconducting levitated mirror) with other widely used magnetometers as shown in Table 4.1. It turns out that the field sensitivity that we have achieved is comparable to the one of NV center and MEMS. In our case, the sensitivity of the levitated mirror for sensing AC magnetic field decreases with higher bandwidth. The mirror’s sensitivity will be improved to  $\sim \text{fT}/\sqrt{\text{Hz}}$  by building a cavity based this levitated mirror, which is described in details in Chapter 6.

**Table 4.1.** Comparison of different magnetometers. SQUID: superconducting quantum interference device; SERF: spin-exchange relaxation-free atomic magnetometers; NV Center: nitrogen-vacancy center; MEMS: micro-electromechanical systems.

Magnetometers Types	Field Sensitivity	Vector Sensor (Yes/No)
SQUID	$\sim \text{aT}/\sqrt{\text{Hz}}$ [177]	No
SERF	$\sim \text{fT}/\sqrt{(\text{Hz})}$ [178]	Yes [179]
MEMS	$\sim \text{pT}/\sqrt{(\text{Hz})}$ [180]	No
NV Center	$\sim \text{pT}/\sqrt{(\text{Hz})}$ [181]	Yes [182]
Our Work	$370 \text{ pT}/\sqrt{\text{Hz}}$	Yes

It should be noted that what we measure is the motions of the levitated mirror due to the effective force from the external coil above the mirror. Even though the oscillating external field from the coil can in principle induce an oscillating supercurrent with time response given by the geometry of experimental setup and superconductor material properties, we only measure the mirror’s motion in response (direct or indirect) to a known current in the coil and we do not make any assumption about the effect of external magnetic field on the mirror. Also, we can accurately estimate the field applied by the coil to calibrate the force sensing. In addition, the magnetic field applied from the coil on the mirror is on the order of  $nT$  whose magnitude is even less at the location of the superconductor. This is far smaller than the field of the levitated magnet near the superconductor. Therefore, we believe the

interaction between the coil current and the superconductor disk is negligible, and it will basically not affect our sensitivity estimation of sensing the magnetic field.

#### 4.6 Fabry-Pérot Cavity Built Based on Superconducting Levitated Mirror

We further use the levitated mirror as the end mirror of a cavity to demonstrate the optical resonance and characterize the properties of the cavity. The demonstration of optical resonance of the suspended cavity mirror is significant for various reasons: 1) a stable cavity resonance, once achieved, can enhance the measurement sensitivity of the mirror's position in both DC and AC regimes, 2) the optical spring can be more than an order of magnitude stiffer than the superconducting trap, enabling the study of optomechanical effects, 3) the intra-cavity optical field can potentially trap the mirror along the direction of the cavity axis through AC radiation pressure force or the optical spring effect [183], [184]. In the current experiment, we build an optical resonator using the levitated mirror as the end mirror of a Fabry-Pérot cavity. The calculated optical trapping potential is plotted in Fig. 4.6 as a function of the mirror's position from the resonant condition, considering the experimental parameters. Fig. 4.6 (inset) also shows the theoretical curves for the optical stiffness and trapping frequency as a function of light frequency relative to the cavity resonance (cavity-light detuning). The maximum trapping frequency expected is around 300 Hz which is achieved if the mirror position is self-locked to the laser frequency.

To build a cavity, we use a fixed mirror placed about 9 cm away from the levitated mirror. The initial angle ( $\theta$ ) of the magnetic moment of the levitated mirror with respect to the z axis can be controlled using a magnet on a nano-positioner stage. The cavity spectrum measured from the reflection of the fixed cavity mirror using a quarter waveplate and a polarizing beam splitter (PBS) along the cavity axis is plotted in Fig. 4.7 as a function of time and displacement of the levitated cavity mirror along the cavity axis (y axis), primarily showing three optical resonant modes within one free-spectral range (FSR). By observing the cavity lines over many FSRs, we found the oscillation frequency of the mirror along the cavity axis to be around 12.5Hz which agrees well with the theoretically calculated frequency of 15Hz. Using this experimentally observed oscillation frequency, we estimate the vibrational

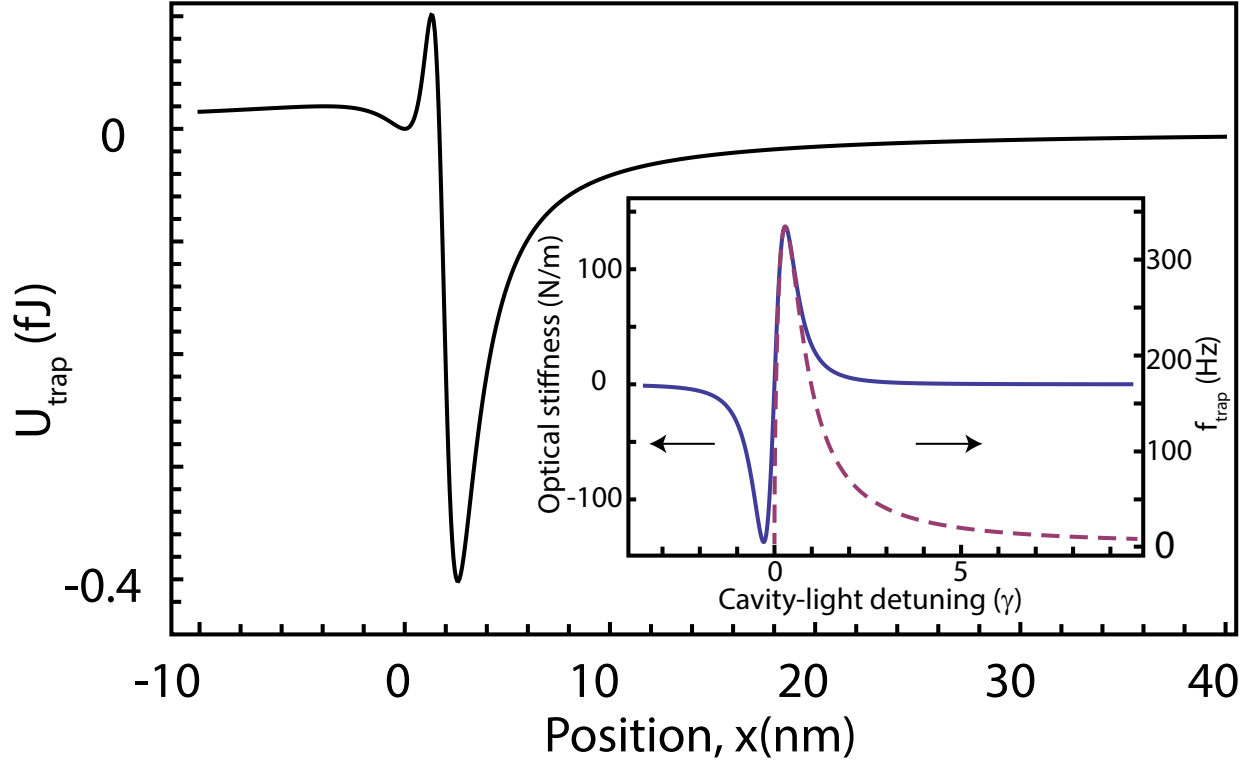


**Figure 4.6.** Theoretical calculation of trapping frequency ( $f_y = f_{trap}$ ), optical stiffness and trapping potential ( $U_{trap}$  in the inset) for a mirror of mass 30mg and cavity of finesse (input power) of 400 (0.25W).

amplitude of the levitated cavity mirror along the cavity axis to be around  $5\mu\text{m}$ , which is in agreement with the measured value shown in Fig. 4.5(a) for  $f_y$  frequency. Without any feedback to stabilize the cavity, a transient optical resonance could be observed with a full linewidth of about  $25\mu\text{s}$  corresponding to the cavity linewidth of about 10nm, and a cavity finesse of 400.

Since the optical cavity length is not stable in our experiment where the damping and restoring forces compete in the system (oscillation between blue- and red-detuned cavity), the overall effect of the transient AC radiation pressure force is not clearly observed. As the cavity length changes in time scale faster than the trapping time scale, the optical effect, manifested as a cavity self-locking effect or shift in the mirror's mechanical frequency, is not observable. This problem will be solved by our new ultra-low vibrational close-cycle

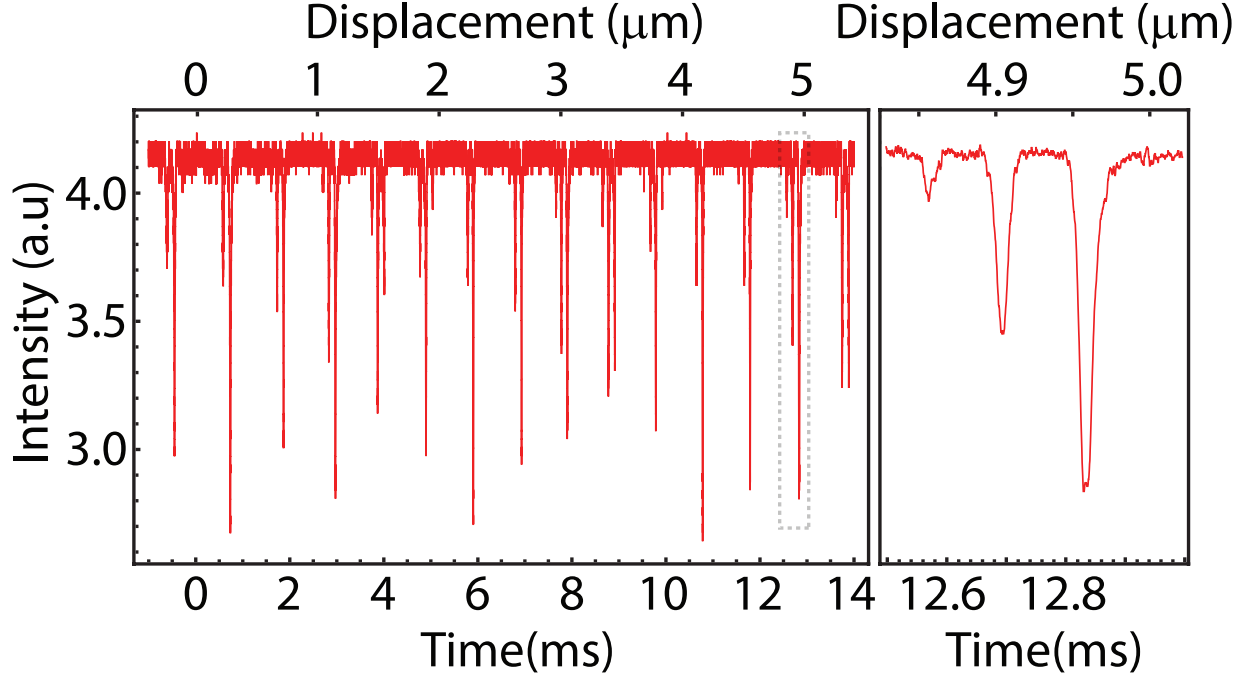


**Figure 4.7.** Intensity of the reflected light from the fixed cavity mirror as a function of the experiment time and the displacement along the cavity axis (y axis). Inset shows the signal close up in a shorter time window (dashed box).

cryogenic system with the noise level on the order of a few nanometers and even less using a vertical-cavity geometry to obtain the common-mode vibrations.

A clear trapping frequency due to the optical spring effect [185] can be observed, in principle, by suppressing the mechanical noise on the mirror which leads to the stable cavity resonances and thus coherent trapping of the mirror. The stability of the mirror and the cavity resonance can be enhanced using different approaches namely: passive control of the environment around the mirror via the mechanical and magnetic shielding, active feedback to the cavity length via external electromagnetic field control [186], and also all-optical self locking [173], [187] relying on AC radiation pressure force.

Once low-frequency mechanical noise can be controlled, the optical radiation pressure force of the cavity may enable, in principle, coherent optical trapping of the mirror in the direction of the cavity axis. Assuming the vibration amplitude of the mirror can be controlled to less than 10 nm at 15Hz, which can be achieved by state-of-the-art ultra-low vibration cryostats, the optical trapping potential of the cavity field of finesse 400 can exceed the

kinetic energy of the mirror with a mass of 10mg. The mirror can be optically trapped in one direction while trapping in other directions is achieved by the superconducting trap. The optical spring effect of the cavity field can increase the mirror frequency along the cavity axis from  $f_y = 15\text{Hz}$  to  $f_y > 300\text{Hz}$  where other mechanical noise is absent enabling study of optomechanical interactions and sensing using macroscopic objects [188]. Apart from optomechanical magnetometry [172], [189], [190], gravity sensing [191], [192] and the study of quantum mechanical motion of macroscopic objects [193], [194] are other applications of the levitated cavity mirror. In the vertical cavity geometry, for example, the coherent trapping of the mirror using the intra-cavity field enables sensing the change in the gravitational acceleration,  $g$ , by shot-noise limited measurement of the intensity of the out-coupled cavity light. When the density modulation of interacting objects occurs at a rate close to the optical trapping frequency, its effect can be predominantly measured by a change in the cavity power ( $P_c$ ), i.e.  $dg/g = dP_c/P_c$ , that is limited by the shot noise. Moreover, in the vertical geometry, the common-mode vertical vibration of the cavity mirrors can dramatically enhance the mechanical stability of the cavity. The macroscopic optomechanical approach may then potentially contribute to the understanding of screened interactions [195], [196] by, for example, studying the forces between an ensemble of ultra-cold atoms and the levitated cavity mirror.

## 4.7 Summary

In conclusion, we have demonstrated the levitation of a mg-scale mirror at ambient conditions above a superconductor. The levitated mirror serves as the end mirror of a Fabry-Pérot cavity and we have used it to test its sensitivity to the externally applied magnetic fields and observed the peak sensitivity of  $370 \text{ pT}/\sqrt{\text{Hz}}$ . By stabilizing a cavity of finesse 400, the magnetic field sensitivity on the order of  $\text{fT}/\sqrt{\text{Hz}}$  or better is within reach. The transfer of the magnetic trap to the restoring optical force of the intra-cavity field can enable the first coherent trapping in one dimension with broad applications in sensing. The tunable vibrational frequency of the mirror along the cavity axis enables the broadband sensing of



the mirror's position, and the mirror's macroscopic surface makes the directional sensing of the external forces possible.

## 5. DRIVEN NONLINEAR DAMPING AND MODE COUPLING IN A SUPERCONDUCTING LEVITATED MAGNET

To study the vibrational noise of the superconducting levitated magnet, the nonlinear damping mechanism and the mode coupling are explored in this chapter, which is reproduced from our previously published work [197], with the permission of APS Publishing.

### 5.1 Introduction

Levitated mechanical oscillators with exceptionally low mechanical dissipation rates are being investigated for applications in precision sensing and even observation of quantum phenomena at the mesoscopic scale [198]. Observation of quantum effects in acoustic vibrations of nanostructures [137], [199] and macroscopic volumes of superfluid liquid [200] are examples where boundaries of quantum and classical mechanics can be studied. Compared with acoustic waves, the center-of-mass (CM) motion of micro and macro-scale objects provides a different toolbox to harness the mode coupling and dissipation. Optical tweezers have been proven useful in studying the CM motion of objects ranging from a single trapped neutral atom [201] to  $10^3$ -atom Bose-Einstein Condensates [202] and  $10^8$ -atom solid nanospheres [68]. Other kinds of levitation techniques, such as superconducting levitation, have been proposed for coupling mechanical vibrations to other forms of coherent oscillatory modes [73], [74], [76]. Superconducting levitation systems are also being investigated for magnetometry and accelerometry [14], [76], [165] and very recently a method for ground-state cooling in these systems was proposed [203]. Although the phenomenon of superconducting levitation in the steady state is well known, the dynamic nature of superconducting trapping and its dissipation mechanisms [88], [204] is not well understood.

In this chapter, we consider a levitated magnetic mirror above a superconductor and study the mode coupling and nonlinear dissipation. We have found that nonlinear coupling between different oscillation modes of the mirror can be harnessed to control the damping of certain vibrational modes via an off-resonance drive. For example, by exciting the vertical oscillation mode (along  $z$ ) of the magnetic mirror, the magnetic inhomogeneity in the

orthogonal directions can be introduced via mode coupling. The orthogonal field fluctuations on the superconducting disk (SD) then lead to enhanced hysteresis losses, damping oscillation energy in modes other than  $z$ . In this regime, suppressing of vibrational noise of modes orthogonal to  $z$  is possible if the excitation frequency is far from the parametric heating regime of the damped modes. The geometry and detection method used in the current levitation experiment enable us to realize such a controlled driven dissipation or “cooling by heating” phenomenon. Here the induced dissipation is the result of mode coupling and nonlinear damping inherent in superconductors.

## 5.2 Theoretical Calculation of Vibrational Modes of Levitated Magnetic Mirror

We use the frozen-image model [82], [83] to theoretically calculate the vibrational modes of the levitated magnetic mirror. In this model, we approximate the levitated magnetic mirror with a magnetic dipole ( $d$ ). This dipole generates one frozen image ( $d'$ ) before field cooling, and then another diamagnetic image ( $d''$ ) after field cooling inside of the SD during the levitation process, as shown in Fig. 5.1. The magnetic moment ( $\mathbf{m}_{\text{lev}}$ ) of the magnetic mirror after levitation makes an angle of  $\theta$  with the vertical axis ( $z$ ), while the initial angle between the magnetic moment ( $\mathbf{m}_{\text{fro}}$ ) of frozen image and  $z$  axis is  $\theta' = 90^\circ$  before levitation. This is because the magnetization axis of the levitated magnetic mirror is along  $y$  axis in our experiment.  $h$  is the levitation height of the magnetically levitated mirror here.

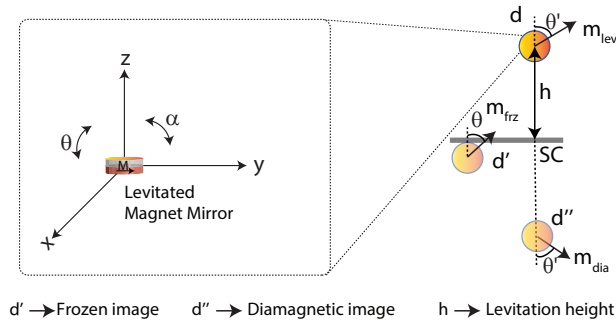


**Figure 5.1.** Frozen image model diagram.

Taking the center of mass of the levitated magnetic mirror as the origin of the coordinate system, the magnetic field that the frozen and diamagnetic images  $d'$  and  $d''$  imposes to the magnetic dipole ( $d$ ) is denoted by  $\mathbf{B}$  in the following equation:

$$\mathbf{B} = \frac{\mu_0}{4\pi} \left\{ \left[ \frac{3(\mathbf{m}_{\text{fro}} \cdot \mathbf{r}')\mathbf{r}'}{r'^5} - \frac{\mathbf{m}_{\text{fro}}}{r'^3} \right] - \left[ \frac{3(\mathbf{m}_{\text{dia}} \cdot \mathbf{r}'')\mathbf{r}''}{r''^5} - \frac{\mathbf{m}_{\text{dia}}}{r''^3} \right] \right\} \quad (5.1)$$

where  $\mathbf{r}' = -(x\hat{\mathbf{x}} + y\hat{\mathbf{y}} + z\hat{\mathbf{z}})$ ,  $\mathbf{r}'' = -2h\hat{\mathbf{z}}$ ,  $\mu_0$  is the vacuum permeability. Then by calculating the trapping potential energy between the magnetic dipole( $d$ ) and these two images( $d'$  and  $d''$ ), the magnetic force ( $\mathbf{F}$ ) and torque( $\mathbf{T}$ ) exerted on the magnetic mirror can be describe as:

$$\mathbf{F} = \nabla(\mathbf{m} \cdot \mathbf{B}) = \frac{\mu_0 \mathbf{m}}{4\pi} \nabla \left\{ \left[ \frac{3(\mathbf{m}_{\text{fro}} \cdot \mathbf{r}')\mathbf{r}'}{r'^5} - \frac{\mathbf{m}_{\text{fro}}}{r'^3} \right] - \left[ \frac{3(\mathbf{m}_{\text{dia}} \cdot \mathbf{r}'')\mathbf{r}''}{r''^5} - \frac{\mathbf{m}_{\text{dia}}}{r''^3} \right] \right\} \quad (5.2)$$

$$\mathbf{T} = \mathbf{m} \times \mathbf{B} = \frac{\mu_0 \mathbf{m}}{4\pi} \times \left\{ \left[ \frac{3(\mathbf{m}_{\text{fro}} \cdot \mathbf{r}')\mathbf{r}'}{r'^5} - \frac{\mathbf{m}_{\text{fro}}}{r'^3} \right] - \left[ \frac{3(\mathbf{m}_{\text{dia}} \cdot \mathbf{r}'')\mathbf{r}''}{r''^5} - \frac{\mathbf{m}_{\text{dia}}}{r''^3} \right] \right\} \quad (5.3)$$

We approximate the magnitude of magnetic moment of the magnetic mirror  $|\mathbf{m}| = |\mathbf{m}_{\text{fro}}| = |\mathbf{m}_{\text{dia}}| = M$ , the azimuthal angle in the spherical coordinate system  $\varphi \simeq 0^\circ$  and the polar angle  $\theta \simeq 90^\circ$  based on our experimental conditions, and then derive the equations of motion of the magnetic mirror as:

$$m\ddot{x} + c_{xx}\dot{x} + c_{x\theta}\dot{\theta} - \frac{3\mu_0 M^2}{4\pi} \left( \frac{(z+2h) + x(\pi/2 - \theta)}{[x + (z+2h)^2]^{5/2}} - \frac{5x(z+2z_0)[x + (z+2h)(\pi/2 - \theta)]}{[x + (z+2h)^2]^{7/2}} \right) = 0 \quad (5.4)$$

$$m\ddot{z} + c_{zz}\dot{z} - \frac{3\mu_0 M^2}{4\pi} \left( \frac{3(z+2h)(\pi/2 - \theta) + x}{[x + (z+2h)^2]^{5/2}} - \frac{5(z+2h)^2[x + (z+2h)(\pi/2 - \theta)]}{[x + (z+2h)^2]^{7/2}} - \frac{1}{16(z+h)^4} \right) = mg \quad (5.5)$$

$$I_m\ddot{\theta} + c_{\theta\theta}\dot{\theta} + c_{\theta x}\dot{x} - \frac{3\mu_0 M^2}{4\pi} \left( \frac{(\pi/2 - \theta)}{8(z+2h)^3} + \frac{1}{[x + (z+2h)^2]^{3/2}} + \frac{3(z+2h)[x(\pi/2 - \theta) - (z+2h)]}{[x + (z+2h)^2]^{5/2}} \right) = 0 \quad (5.6)$$

$$m\ddot{y} + c_{yy}\dot{y} + c_{y\alpha}\dot{\alpha} - \frac{3\mu_0 M^2}{4\pi} \left( \frac{y(\pi/2 - \theta)}{[x + (z+2h)^2]^{5/2}} - \frac{5y(z+2h)[x + (z+2h)(\pi/2 - \theta)]}{[x + (z+2h)^2]^{7/2}} \right) = 0 \quad (5.7)$$

$$I_m\ddot{\alpha} + c_{\alpha\alpha}\dot{\alpha} + c_{\alpha y}\dot{y} - \frac{3\mu_0 M^2}{4\pi} \left( \frac{-3y(z+2h)(\pi/2 - \theta)}{[x + (z+2h)^2]^{5/2}} \right) = 0 \quad (5.8)$$

Where  $M$  is calculated to be  $M \simeq 8.4 \times 10^{-4} Am^2$ ,  $I_m \simeq \frac{m}{12}[3r_m^2 + t_m^2]$  is the moment of inertia of the levitated magnetic mirror around  $x$  or  $y$  axis,  $m = 5.3 \times 10^{-6} kg$  is the mass of magnetic mirror,  $r_m = 10^{-3}m$  is the radius of magnetic mirror, and  $t_m = 0.15 \times 10^{-3}m$  is the thickness of the magnetic mirror,  $h = 1.5 \times 10^{-3}m$  is the levitation height,  $g = 9.8m/s^2$  is the acceleration of gravity,  $\sin(\theta) \simeq 1$ ,  $\cos(\theta) \simeq \pi/2 - \theta$ ,  $\cos 2(\theta) \simeq 0$ . By numerically solving the derived equations of motions above, we calculate the resonant frequencies of different modes of the magnetic mirror. The loss parameters in SI units used in this calculation are given as follows:  $c_{\theta\theta} = c_{\alpha\alpha} = 10^{-13} Nms$ ,  $c_{\theta x} = 0.5 \times 10^{-12} Ns$ ,  $c_{\alpha y} = 10^{-12} Ns$ ,  $c_{x\theta} = 0.1 \times 10^{-9} Ns$ ,  $c_{y\alpha} = 0.05 \times 10^{-9} Ns$ ,  $c_{xx} = 10^{-8} Ns/m$ ,  $c_{yy} = 5 \times 10^{-10} Ns/m$ ,  $c_{zz} = 10^{-10} Ns/m$ .

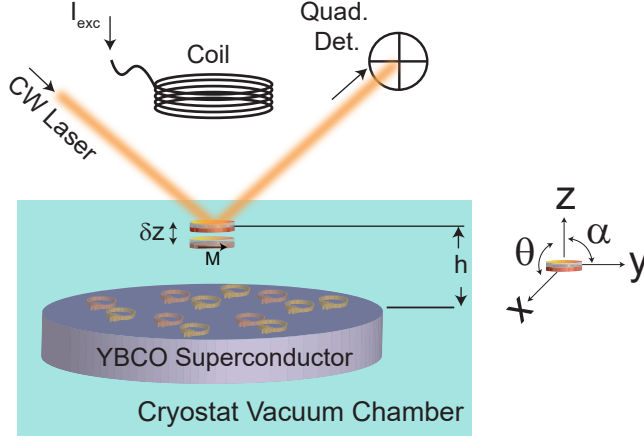


**Figure 5.2.** Experimental setup for a magnetic mirror (a magnetic ring attached to a dielectric mirror) levitated above a superconductor disk and optically probed in vacuum conditions ( $10^{-8}$  Torr). A coil with excitation current,  $I_{exc}$ , can excite and drive the levitated magnet.

### 5.3 Experimental Setup and Measurement

The experimental setup is shown in Fig. 5.2(a). We first purchased the smallest off-the-shelf high-reflective (HR) mirror ( $R > 99.8\%$ ) with both thickness and radius of 1mm and then lapped the mirror down to around 0.1mm thick without damaging its coating surface. And we attached this small HR dielectric mirror with the mass of  $m_r = 3\text{mg}$  to a thin neodymium (Nd) magnetic ring with a thickness of 0.05mm and mass of  $m_n = 2.3\text{mg}$ , which has the same radius as the mirror. We refer to this combination as the “magnetic mirror”, which has a final thickness of 0.15mm and a diameter of 2mm. Although using a smaller/thinner magnetic mirror will have higher oscillation frequencies and Q factors, our mirror is already only  $100\mu\text{m}$  thick and it is difficult to make it smaller since making the thickness of the mirror less than  $100\mu\text{m}$  would damage the coating surface. The disk-shaped levitated magnetic mirror would allow us to determine the orientation of the magnetic moment and study its effect on the dissipation mechanism. Also, the diameter of the mirror is chosen to be 1mm which is much larger than the beam size. By doing so, it can help us avoid the scattering and also determine its orientation and distinguish different modes from each other. Another reason we used the HR mirror instead of simply measuring the

scattering from a levitated magnetic particle was to use the mirror as an end mirror of a cavity. In addition, the use of a high-reflective mirror enables precise optical measurement of position and oscillations of the levitated object in different directions.

A YBaCuO SD with a diameter of 2.5cm and thickness of  $t=2.5\text{mm}$  and critical temperature of  $\sim 93\text{K}$  is placed inside a closed-cycle and ultra-low-vibration cryostat (DMX-20-OM from Advanced Research Systems) and then cooled down to around 10K using cyclic compressed liquid helium. The background gas pressure around the SD and the magnetic mirror was reduced to about  $10^{-7}$  Torr. The magnetic mirror is levitated about  $h=1.5\text{mm}$  above the SD inside the cryostat as shown in Fig. 5.2. To sense the mirror's vibrations, a Ti-sapphire laser light is used and reflected off the magnetic mirror surface and detected by a quadrant detector. There are three reasons why we used the Ti-sapphire laser for our experiment. One is that the Ti-sapphire laser has a low-noise spectrum at low frequencies ( $<200\text{Hz}$ ) where our measurements are performed. The other reason is the stability of the Ti-sapphire laser. For measuring the quality factor of the mechanical modes with frequencies of  $100\text{Hz}$ , we need the integration time to be at least a few minutes, which means the laser needs to be stable within this time scale. The Ti-sapphire laser can satisfy this requirement. The third reason is the high power of the Ti-sapphire laser. Because we were originally interested in sensing the radiation pressure force applied to the levitated magnetic mirror and the high power ( $>1\text{W}$ ) of the Ti-sapphire laser is necessary for such study. Fig. 5.3 shows the optical and electronic noise data in our experiments. We do not observe pointing noise or amplitude noise up to  $200\text{Hz}$  frequencies.

To excite the specific mechanical modes of the levitated mirror, we place a 15-turn coil with a diameter of 3cm above the mirror and modulate the current in the coil at different frequencies and amplitudes. During measurements, the vacuum pump and compressor were temporarily turned off to further reduce the associated mechanical noise.

#### 5.4 Displacement Noise Calibration of Levitated Magnetic Mirror

In order to calibrate the amplitudes of vibration for the levitated magnetic mirror, we mount one dielectric mirror on a piezo-electric transducer (Thorlabs) fixed near the position

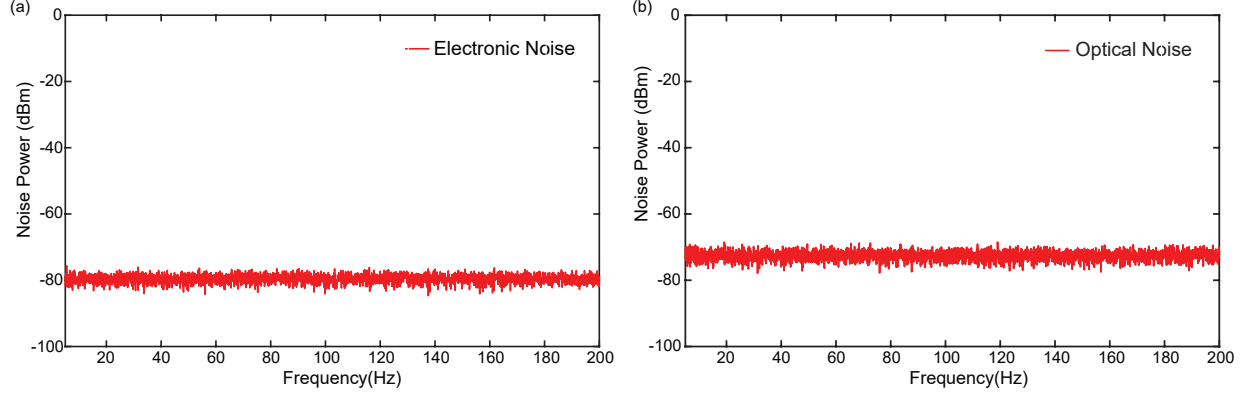


**Figure 5.3.** The optical noise and electronic noise power in the frequency range from 0 to 200Hz

of the levitated magnetic mirror, as shown in Fig. 5.4. By keeping the position and detection angle of the quadrant detector the same as in the levitation experiment, we can calibrate the intensity fluctuations of the magnetic mirror. By scanning the driving voltage of the piezo-electric transducer while using the driving frequency of 90Hz (resonant frequency of magnetic mirror along  $z$  axis,  $\omega_z$ ), we obtain the vibrational energy of the dielectric mirror as the function of its displacement, as shown in Fig. 5.5. In this way, we find the relationship between the quadrant detector intensity fluctuation and the dielectric mirror's displacement ( $A$ ). The linear fit in Fig. 5.5 is  $E = 8.1 \times 10^{-9}A^2 + 3.9 \times 10^{-11}$ . Using this relationship, we calibrate the oscillation amplitude of the levitated magnetic mirror. After calibration, the mirror's oscillation amplitude is calculated to be around  $10 \mu m$  at  $\omega_z = 90Hz$ . The minimum detectable displacement in our experiment was observed to be  $6 \times 10^{-8}m/\sqrt{Hz}$  limited by the quadrant detector sensitivity. We also calculate the rotation sensitivity to be  $5 \times 10^{-5}rad/\sqrt{Hz}$ .

The sensitivity of the quadrant detector also depends on the light spot size on the detector. The relationship between the laser beam radius ( $w$ ) and the quadrant detector sensitivity can be described as follows [205]:

$$S_x = \frac{2R}{w\sqrt{\pi}} \frac{\text{erf}(\frac{R}{w})\exp[(R/w)^2] - \frac{2R}{w\sqrt{\pi}}}{\exp[(R/w)^2] - 1} \quad (5.9)$$



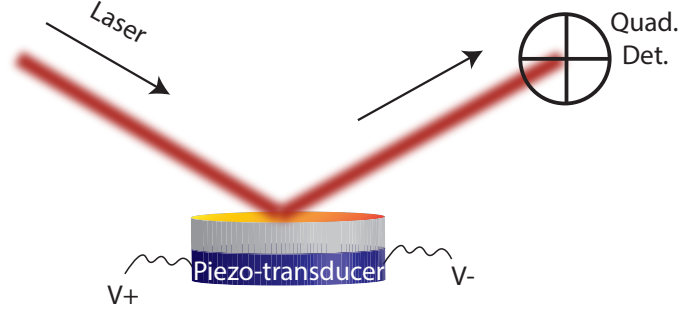


**Figure 5.4.** The setup for calibrating the displacement of the levitated magnetic mirror using the piezoelectric transducer.  $V_+ - V_-$  is the driving voltage applied to the transducer.

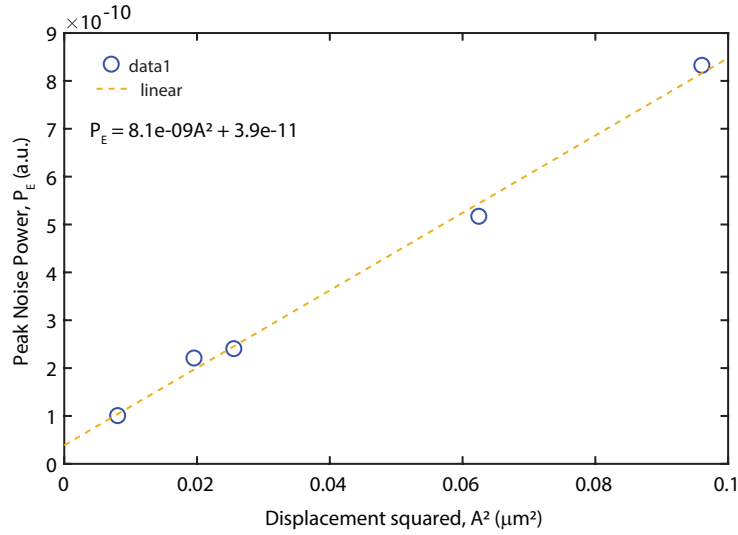


**Figure 5.5.** Calibration of displacement of the levitated magnetic mirror using the piezoelectric transducer

where  $R$  is the radius of the circular sensing area of quadrant detector. Fig. 5.6 (a) from reference above shows how the quadrant detector sensitivity changes with the ratio of  $w/R$ . By reducing the beam size on the detector we were able to increase the sensitivity by an order of magnitude. Fig. 5.7 of the main text and Fig. 5.6 show the results of the displacement noise for two different  $w$ , (about 3mm and 1mm), respectively. The sensitivity can also

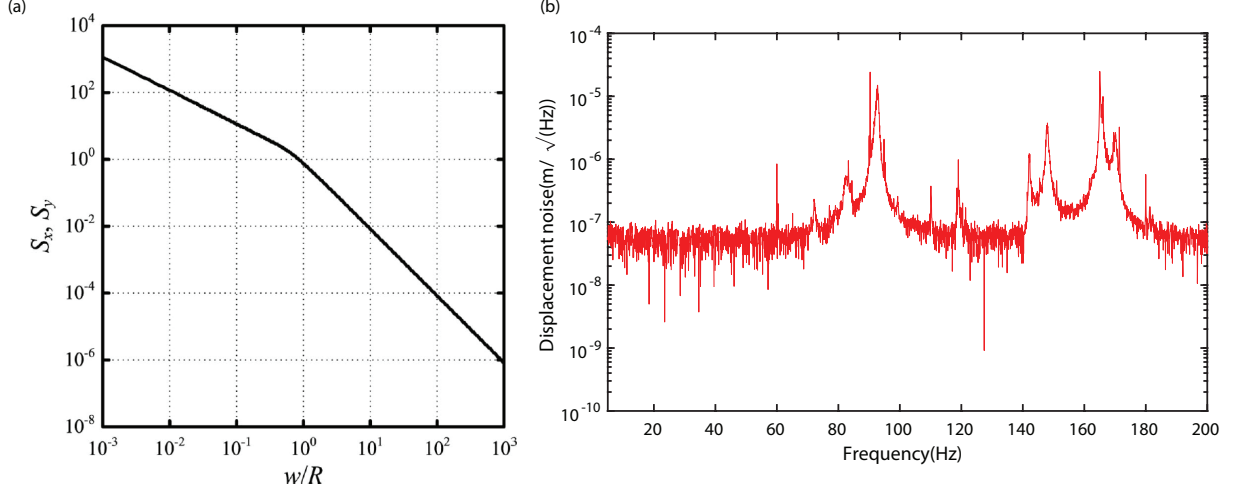


**Figure 5.6.** (a) The quadrant photodetector sensitivity  $S_x$  and  $S_y$  as a function of the ratio of light spot radius ( $w$ ) and quadrant detector radius ( $R$ ) [205]. (b) The displacement noise spectrum measured for the magnetic levitated mirror

be significantly improved when heterodyne or homodyne measurement is performed using a single-pixel detector [206]. In our experiment, because the magnetic mirror's vibration amplitude is high, we don't require higher sensitivity to sense the mirror's resonant modes.

## 5.5 Vibrational Spectra Comparison between Experimental and Theoretical Calculation

The relatively large displacement of the levitated magnetic mirror gives rise to the variation of surface current (or diamagnetic image) in the SD that in part changes the trapping potential. As the result, coupling between the translational and rotational modes of the mirror can occur through the SD. We numerically solve the coupled equations of motion and obtain a theoretical vibrational spectrum for the magnetic mirror, as seen in Fig. 5.7 (b). The theoretical spectrum qualitatively agrees with the experimental data shown in Fig. 5.7 (b). The dominant vibrational mode around 85Hz is identified as the oscillation along the vertical direction ( $\omega_z$ ) with the angular frequency of  $\omega_z$ . The coupling between the translational mode  $x$  (or  $y$ ) and angular mode  $\theta$  (or  $\alpha$ ) gives rise to the emergence of two coupled modes theoretically found to be  $\omega_{v(x,\theta)} \simeq 20\text{Hz}$  (or  $\omega_{p(y,\alpha)} \simeq 48\text{ Hz}$ ) and  $\omega_{u(x,\theta)} \simeq 152$

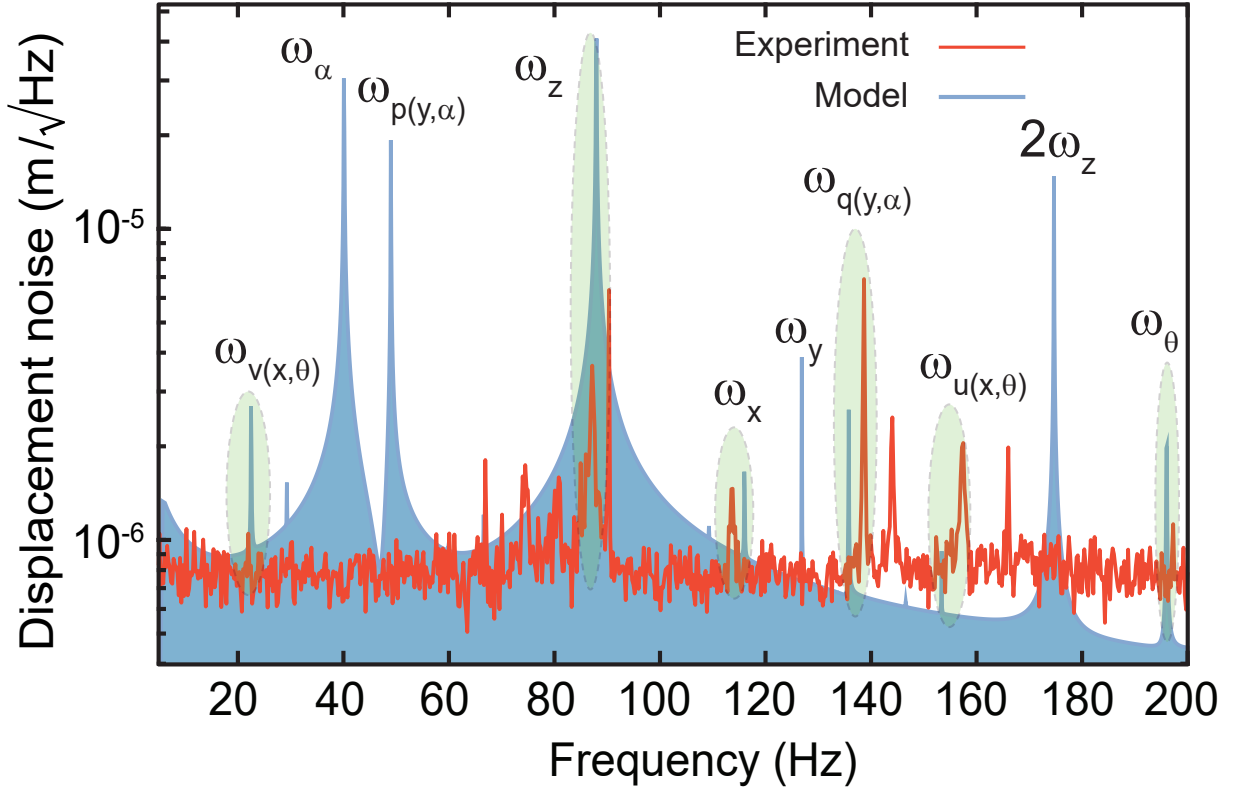


**Figure 5.7.** The theoretical (blue) and experimental (red) vibrational noise spectra of the levitated magnetic mirror. The modes whose resonances could be observed (shaded green areas) match theoretical predictions within 10%. The theoretical spectrum is plotted with an arbitrary offset and excitation.

Hz ( $\omega_{q(y,\alpha)} \simeq 135$  Hz). Not all of the modes could be experimentally observed due to the different excitation and detection sensitivity levels of different modes. The slight discrepancy in predicting the frequencies arises from the lack of precise knowledge of the magnet's orientation and its levitation height upon thermal cycling. Since the levitated magnetic mirror's orientation and position will change the superconducting trapping potential energy which determines the mirror's resonant frequencies. In our theoretical model, we assume the mirror is parallel with the SD ( $\theta = \pi/2$ ). We observe that resonant frequencies of modes can vary slightly every time the SD is re-cooled. This is because of the change in the stable orientation and position of the magnetic mirror upon thermal cycling. As we observed in our experiments, the resonant frequencies of the levitated magnetic mirror highly depend on the

initial orientation/angle of the mirror right after levitation and the levitation height. This effect has also been observed in Ref. [75] where some resonant frequencies were observed to change by as much as 50% when the experimental setup is tilted by only a few degrees for superconducting levitated micromagnets. Having the freedom to vary the theoretical model parameters (height and angle) we can find very good agreement between the simulated and measured resonant frequencies of the levitated magnetic mirror. By tuning the theoretical parameters near their steady-state values (measured in a typical run) we can tune the frequencies in the model to match that of the experiment. That is why we can claim that the experimental results qualitatively agree with the theoretically simulated results. We also observe that resonant frequencies can be different in different experimental runs by about 10%.

The peak heights experimentally measured can be different from the model as our detector sensitivity is not the same for different modes. Another reason is that the degree of coupling between modes is not known and cannot be easily calculated. In the model, we assume the same level of excitation for all modes.

## 5.6 Superconducting Levitated Magnetic Mirror as a Duffing Resonator

By continuously scanning the modulation frequency around  $\omega_z$  in one direction, we observe an asymmetric resonance that is bent towards lower frequencies (see Fig. 5.8 (a)). This is a typical signature of nonlinear oscillation by a soft spring [204]. Fig. 5.8 (b) indicates the time evolution of the amplitude of the levitated mirror under pulsed excitation at the frequency of  $\omega_z$ . The decaying oscillation amplitude, after excitation is switched off, shows the nonlinear oscillations observed as an asymmetric envelope of oscillation amplitudes with respect to the zero axis. This is an indication of anharmonicity in the trapping potential energy [88].

## 5.7 Magnetic Inhomogeneity of Levitated Magnetic Mirror

At low background gas pressures and under vacuum conditions, the primary source of mechanical damping of the oscillating magnetic mirror is the inhomogeneity of the mir-

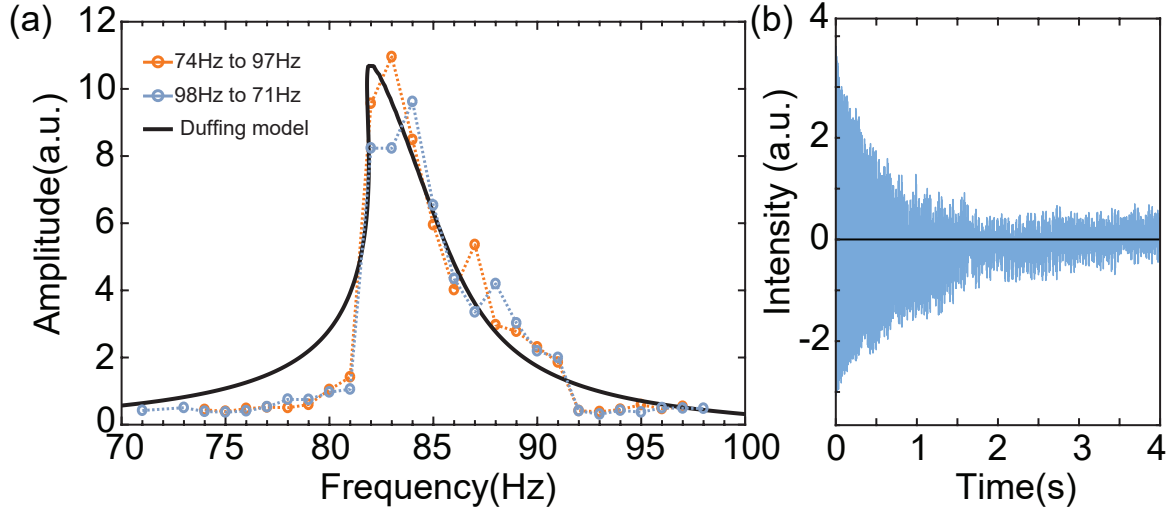


**Figure 5.8.** (a) Nonlinear frequency response of oscillation along  $z$  axis at different modulation frequencies near  $\omega_z$ . The black curve shows the fitting result using Duffing equation. (b) Ring down measurement of pulsed-resonant excitation at  $\omega_z$  shows an asymmetric oscillation with respect to the zero axis, which is caused by the related asymmetric trapping potential

ror's magnetic field distribution giving rise to the hysteretic losses. The field inhomogeneity causes redistribution or density fluctuation of trapped magnetic vortices on the superconductor surface. As the result, energy is dissipated to pay for the altered surface states. The dissipated energy can be quantified by calculating the magnetic field fluctuation ( $\delta B$ ) on the superconductor surface caused by the oscillations of the levitated magnetic mirror. Similar oscillation-induced dissipation was reported [88] when a macroscopic spherical magnet was levitated above a superconductor under ambient conditions. The dissipation for different vibrational modes of the levitated magnet strongly depends on the angle between the magnet's magnetization axis ( $M$ ) and the superconductor surface [88]. A very low dissipation coefficient is expected if the motion of the levitated object is along  $M$ , when  $M$  is parallel to the superconductor surface.

In order to know the magnetic field fluctuation ( $\delta B$ ) of the magnetic mirror on the SC surface, the magnetic field distribution of the neodymium (Nd) magnetic ring along  $z$  axis needs to be calculated. The magnetic mirror in our case is made of one thin diametrically

magnetized neodymium ring and one dielectric mirror. The diameter of both the neodymium ring and the dielectric mirror is the same and equal to  $2 \times 10^{-3}m$ . Therefore, what we need to calculate is the magnetic field distribution along  $z$  axis for the magnetic ring, which can be approximately described as follows [207]:

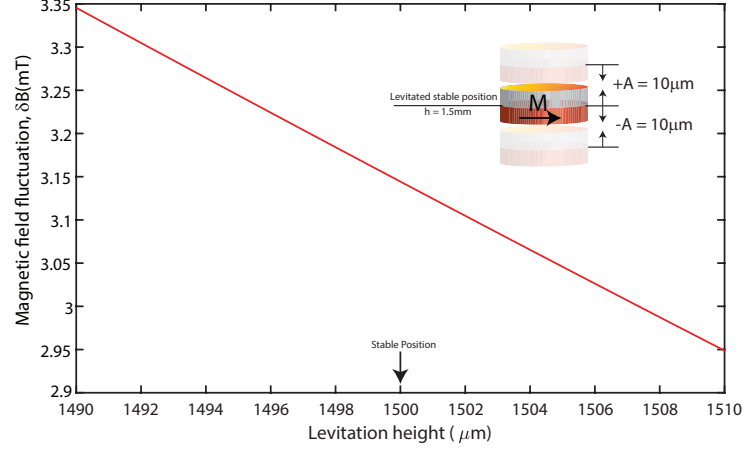


**Figure 5.9.** Calibration of magnetic fluctuation along  $z$  axis,  $\delta B$

$$H_z = \frac{JR \sin(\psi)}{\pi \mu_0} \left\{ \left[ \frac{a_o \mathbf{K}[p_o] + (c_o - a_o) \mathbf{E}[p_o]}{a_o \sqrt{a_o - c_o}} - \frac{b_o \mathbf{K}[\mu_o] + (c_o - b_o) \mathbf{E}[\mu_o]}{c \sqrt{b_o - c_o}} \right] - \left[ \frac{a_i \mathbf{K}[p_i] + (c_i - a_i) \mathbf{E}[p_i]}{a_i \sqrt{a_i - c_i}} - \frac{b_i \mathbf{K}[\mu_i] + (c_i - b_i) \mathbf{E}[\mu_i]}{c_i \sqrt{b_i - c_i}} \right] \right\} \quad (5.10)$$

where  $J = (1 + 1/\chi_v) \mu_0 M \simeq \mu_0 M$  because  $1/\chi_v \simeq 0$  for neodymium,  $r_o = 10^{-3}m$  and  $r_i = 0.5 \times 10^{-3}m$  are the outer and inner diameters of the magnetic neodymium ring, respectively,  $a_o = (h - t/2)^2 + r_o^2 + r^2$ ,  $b_o = (h + t/2)^2 + r_o^2 + r^2$ ,  $c_o = 2r_o r$ ,  $p_o = 2c_o/(c_o - a_o)$ ,  $\mu_o = 2c_o/(c_o - b_o)$ ,  $a_i = (h - t/2)^2 + r_i^2 + r^2$ ,  $b_i = (h + t/2)^2 + r_i^2 + r^2$ ,  $c_i = 2r_i r$ ,  $p_i = 2c_i/(c_i - a_i)$ ,  $\mu_i = 2c_i/(c_i - b_i)$ . Here  $t = 0.05 \times 10^{-3}m$  is the thickness of the neodymium ring.  $\mathbf{K}[\mu_o]$  and  $\mathbf{K}[\mu_i]$  are the complete elliptic integral of the first kind,  $\mathbf{E}[p_o]$  and  $\mathbf{E}[p_i]$  are the complete elliptic integral of the second kind. Because  $\mu_o$ ,  $p_o$ ,  $\mu_i$ , and  $p_i$  in our case are very close to zero and the complete elliptic integrals are dimensionless, it is reasonable to assume  $\mathbf{K}[\mu_o] = \mathbf{E}[p_o] = \mathbf{K}[\mu_i] = \mathbf{E}[p_i] \simeq 1.6$ . We consider the angular and radial coordinates  $\psi = \pi/2$  and  $r \simeq 0$  and then calculate the magnetic fluctuation ( $\delta B \simeq 434 \mu T$ ) sensed by SC when the

magnetic mirror is oscillating  $+/- 10\mu m$  around the levitation height  $h = 1.5mm$  along  $z$  axis after levitation, as shown in Fig. 5.9.

## 5.8 Effect of Magnetic Mirror's Orientation

The resonant frequencies of the magnetic mirror along different axes are determined by the superconducting trapping potential, which is defined by the position and orientation of the levitated magnetic mirror. Since the magnetic mirror is levitated from the initial rest position of the SC disk, its orientation and position are not always the same every time SC is cooled down. As a result, the trapping potential is slightly different after a thermal cycle. As reported in Ref. [14], a shifting of resonant frequencies of more than 50% has been reported for the superconducting levitated neodymium magnet sphere. We have also experimentally observed the resonant-frequency change of more than 10% from different experimental runs. It should be noted that the levitated magnetic mirror's orientation and position can be controlled via an external magnetic field as we have demonstrated in our previous paper [165].

In different experimental runs, we have observed that the frequency of the vibrational mode ( $\omega_z$ ) along  $z$  axis can vary from 84Hz to around 90Hz, and the coupled modes,  $\omega_{u(x,\theta)}$ , can vary from 158Hz to 164Hz,  $\omega_{q(y,\alpha)}$  can vary from 138Hz to 148Hz.

Other than the shifting of the resonant frequencies, the mechanical Q factor of modes varies in different experimental runs depending on external excitation and background noise level. This is because the magnetic fluctuation ( $\delta B$ ) caused by the inhomogeneity of the levitated magnetic mirror on the superconductor surface can be different changing the dissipation.

As shown in Fig. 5.10, the coupled modes ( $\omega_{q(y,\alpha)} = 148Hz$  and  $\omega_{u(x,\theta)} = 164Hz$ ) could be simultaneously cooled down by different amounts when we drive the levitated magnetic mirror at  $\omega_z = 90Hz$  ( $z$  mode). By varying the modulation voltages (proportional to  $\Delta B$ ) from 0 to about 5V, the vibrational noise of  $\omega_{q(y,\alpha)}$  and  $\omega_{u(x,\theta)}$  decrease by more than 20dB and 10dB, respectively. The relationship between the modulation voltage and the modulation magnetic amplitude is  $14\mu T/V$  based on our calibration.

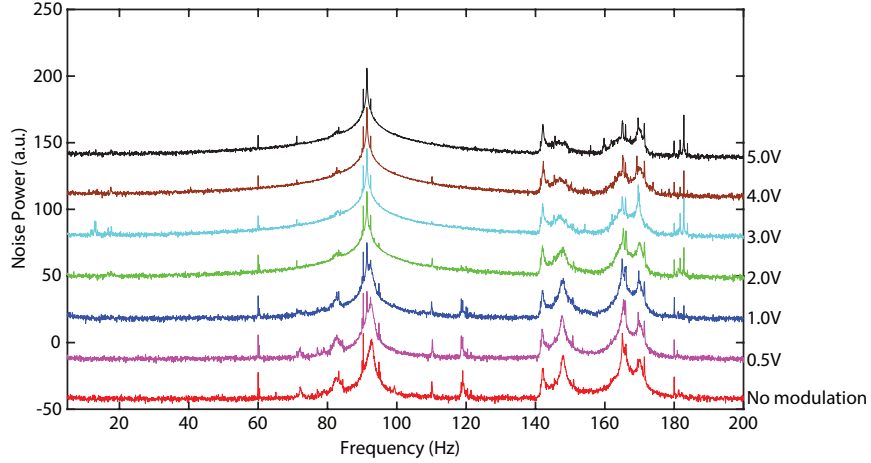


**Figure 5.10.** Observation of multi-mode cooling at different magnetic modulation voltages (proportional to  $\Delta B$ ) introduced by the driving coil at  $\omega_z = 90\text{Hz}$ . The vibrational spectra are vertically shifted for different modulation amplitudes for clarity. Simultaneous cooling of modes at 148Hz and 164Hz can be seen.

## 5.9 Quality Factor (Q) Measurement

When the dissipation due to background gas and external magnetic field fluctuations is negligible, the quality factors of different vibrational modes are determined by the geometrical factors such as the magnetic inhomogeneity of the levitated object, its magnetic axis, external excitation, and the superconductor configuration. Therefore, we expect different vibrational modes to have different linewidths, which is in agreement with our experimental observations as shown in Fig. 5.7 (b).

We have measured the Q factors for different mechanical modes, the value varies from a few hundred to more than 3000 for different modes. For the resonant frequency of the  $z$  mode with a frequency of  $\omega_z$ , the Q value is 483, which is the lowest among all the mechanical modes. The reason for this is its motion induces the largest magnetic field inhomogeneity on the superconductor surface. For the coupled mode,  $\omega_{q(y,\alpha)} = 138.5\text{Hz}$ , the measured Q was about 3000, with a mechanical linewidth of 0.05Hz obtained using a resolution bandwidth (RB) of 0.05Hz. This measurement is clearly limited by the resolution bandwidth of our detection. For these measurements, we turned off the vacuum pump and the compressor to reduce the mechanical noise. The maximum time we could turn off the pump and the



compressor is about 15 minutes before the superconductor temperature changes, which shifts the resonant frequencies. We realize that the lower-frequency modes, which could not be observed initially using  $RB = 0.05\text{Hz}$ , are high-Q modes and become visible when a longer integration time (higher resolution bandwidth) is used. By recording the detector signal in the temporal domain for about 1000s ( $RB = 0.001\text{Hz}$ ) which is the maximum time we could integrate for the signal and then doing the Fourier Transform, we could observe  $Q=3600$  for  $\omega_{v(x,\theta)}$  mode, which is no longer limited by our measurement (see Fig. 5.12 (a)). Fig. 5.11 shows the spectrum obtained for higher resolution bandwidth (0.001Hz) where external excitation was applied at  $\omega_q(x,\theta)$  to further excite mode  $\omega_v(x,\theta)$ . A 28.8Hz mode is visible that corresponds to  $\omega_v(x,\theta)$ . An additional mode detected around 55Hz could be  $\omega_p(y,\alpha)$ . It is found that the non-observable modes ( $\omega_y$  and  $\omega_\alpha$ ) are orthogonal to the modes related to the oscillations along  $x$  and  $\theta$  directions. Because the magnetization axis ( $M$ ) of the levitated magnet in our experiments is in the horizontal plane(x-y plane), which breaks the symmetry causing different excitations or dissipation rates for the modes along  $x$  and  $\theta$  as well as the modes along  $y$  and  $\alpha$  directions.

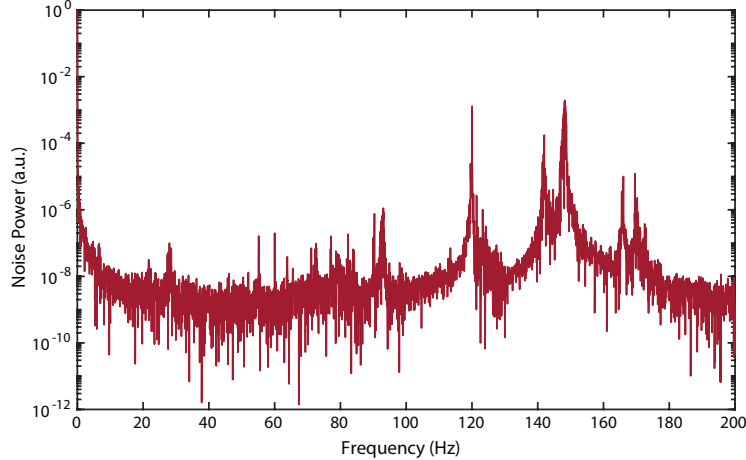


**Figure 5.11.** Noise power spectrum measured with resolution bandwidth of 0.001 Hz.

We note that  $Q$  factors as high as  $10^7$  can be reached for smaller magnetic levitated particles [75]. The  $Q$  factors of vibrational modes of SC levitated magnets depend on the size of the magnet and its levitation height above the superconductor [208]. In the case of a superconducting levitated magnetic sphere with the radius of  $r$  and levitation height

of  $h$ , the  $Q$  factor of mechanical modes is shown to be proportional to  $(h/r)^3$ . For one micromagnet with  $r = 30\mu\text{m}$  levitated  $h = 300\mu\text{m}$  above the superconductor, a  $Q$  of  $10^7$  has been measured [75]. Since the radius of the magnetic mirror and its levitation height in our experiments are 1mm and 1.5mm, respectively, thus the relatively large size limits our  $Q$  factors. Also, by choosing different geometry of the levitated magnet, one can reach higher  $Q$ s. The background gas pressure and external field fluctuations are other factors determining the  $Q$ s [75].

By exciting certain mechanical modes of the levitated magnetic mirror, we examine how the dissipation rates of the resonant modes change. The excitation is achieved by modulating the current inside the driving coil above the levitated magnetic mirror. Fig. 5.12 (b) indicates that the linewidths of the resonant modes dramatically increase as the modulation frequency approaches the resonant frequencies of the levitated magnetic mirror. This also suggests that the ring-down measurement is not a reliable way to measure  $Q$  as the excitation itself increases the damping and thus lowers the  $Q$ .

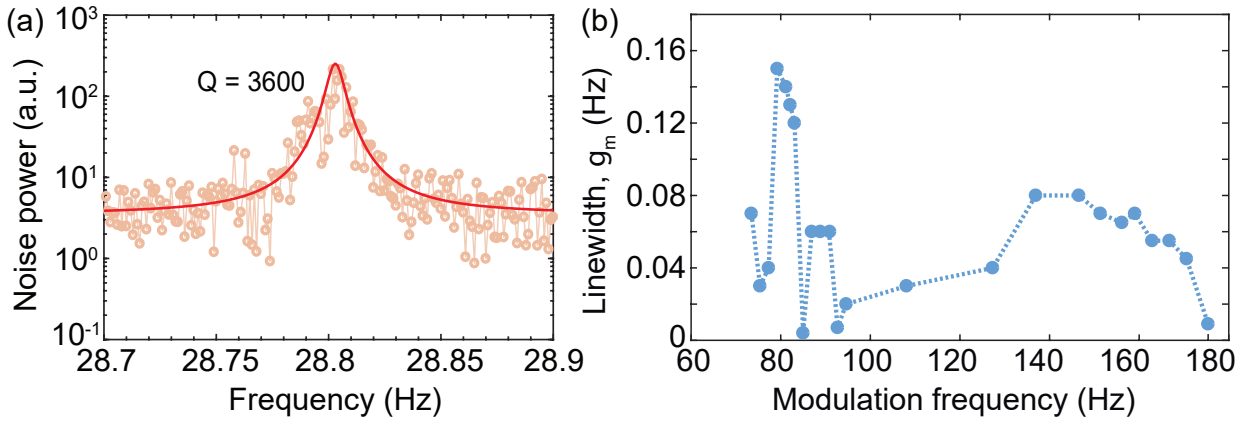


**Figure 5.12.** (a) Spectrum of the high- $Q$  coupled mode  $\omega_{v(x,\theta)}$  measured with a resolution bandwidth of 0.001Hz. (b) The fitted linewidth as a function of the external modulation frequency with a constant modulation amplitude  $\Delta B = 28\mu\text{T}$  shows the effect of external excitation on mechanical  $Q$ . The dotted line here is a guide to the eye.

### 5.10 Nonlinear Energy Dissipation

The origin of this excitation-induced dissipation is nonlinear damping that can be used to reduce the vibrational noise of certain modes. When the levitated magnetic mirror oscillates above the SD, its motion modulates the stray magnetic field on the surface of the SD. This is the result of the inhomogeneous magnetic field sensed on the SD surface when the mirror moves. This forces the superconducting trapped magnetic vortices to undergo a dynamical variation of configuration or density. The dissipation arising from this transformation is nonlinear. The dynamic dissipation energy during a hysteretic cycle per unit volume,  $\delta E$ , can be described using a modified Bean's critical state model or Irie-Yamafuji model [87], [89], [90] that follows the following relationship:

$$\frac{\delta E - \delta E_0}{\delta E_0} \simeq \frac{1}{2} \omega \tau_0 \quad (5.11)$$

where  $\delta E_0$  is the static energy loss per cycle per unit volume, and  $\tau_0$  is the time scale of the oscillation. In the regime where  $\omega \tau_0 > 1$ , the dynamic dissipation can exceed the static one. Similar results are expected using the collective weak-pinning theory [209] where the cross-over between the hysteretic and viscous damping regimes can be calculated.

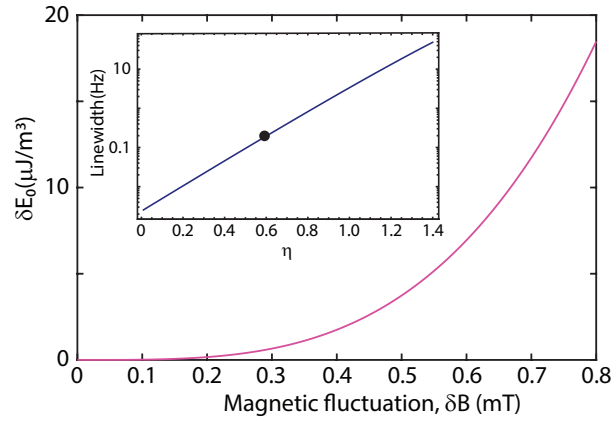


**Figure 5.13.** The calculated static dissipated energy per unit volume ( $\delta E_0$ ) as a function of magnetic field fluctuation ( $\delta B$ ) induced by the magnetic mirror oscillating along the  $z$  axis. Inset shows the calculated mechanical linewidth at  $\omega_z$  for different values of  $\eta$ .

By calibrating the oscillation amplitude along  $z$  axis, we can estimate the magnetic field inhomogeneity induced by the vertical vibrations of the magnetic mirror. We find that at  $\omega_z \simeq 85$  Hz the maximum vibration-induced magnetic field inhomogeneity along  $z$  axis is  $\delta B = 400\mu\text{T}$  on the surface of the superconductor. The static dissipated energy per cycle per unit volume,  $\delta E_0$ , and the linewidth of certain mechanical modes can then be calculated using Eq. (5.12) [88].

$$\delta E_0 = \frac{4 - 2\eta}{3(j_c t)^{2-\eta}} \mu_0^{\eta-3} (\delta B)^{4-\eta}. \quad (5.12)$$

where  $j_c$  is the critical current which is generally in the range of  $20\text{--}40\text{ kA/cm}^2$ ,  $\eta$  is a density parameter varies from 0 to 1.4 depending on flux pin-distribution and coherence length,  $t$  is the thickness of the superconductor. Fig. 5.13 (a) shows the calculated energy statically dissipated per unit volume ( $\delta E_0$ ) as a function of the magnetic field fluctuation ( $\delta B$ ) induced by the levitated magnetic mirror. The inset of Fig. 5.13 shows how the theoretical linewidth of  $z$  mode varies with the parameter  $\eta$ . In our experiment, the linewidth of  $z$  mode is around 0.2 Hz which corresponds to  $\eta=0.6$ , as marked with the black dot.

### 5.11 Cooling Theory

The approach to cooling a vibrational mode described in this paper is conceptually similar to feedback cooling as in both cases an external excitation of a mode is used to cool the thermal fluctuations. To obtain a theoretical description of cooling in our case we expand on the theory of feedback cooling [210]–[212], and use an appropriate description of forces and external excitations to derive the limits of cooling.

The displacement spectrum of the magnetic mirror can be written as

$$u(\omega) = \chi(\omega)(F_{th}(\omega) + F_v(\omega)) \quad (5.13)$$

where  $F_{th}$ , and  $F_v$  are the thermal and viscous forces, respectively, and the mechanical susceptibility is defined as

$$\chi(\omega) = \frac{1}{m(\omega_m^2 - \omega^2 + i\gamma_m\omega)} \quad (5.14)$$

where  $m$ ,  $\omega_m$ , and  $\gamma_m$  are mass, resonant frequency and bare mechanical damping rate of the levitated magnetic mirror, respectively, for the mode being cooled (e.g.  $u$ ). In the thermal noise limit, the fluctuation of the magnet is driven by the Brownian force described by  $F_{th}$  with spectral density

$$S_F^{(th)}(\omega) = \langle |F_{th}(\omega)|^2 \rangle = m\gamma_m\hbar\omega \coth \frac{\hbar\omega}{2k_B T}, \quad (5.15)$$

which, in the limit of high temperatures, becomes  $S_F^{(th)}(\omega) \simeq 2m\gamma_mk_BT$ . The viscous force can be approximately derived using the energy loss per unit volume  $V$  (within which dissipation occurs),  $\delta E_0 = \frac{4-2\eta}{3(j_c t)^{2-\eta}} \mu_0^{\eta-3} (\delta B)^{4-\eta}$ , where  $j_c$  is the critical current which is in the range of  $20\text{-}40\text{ kA/cm}^2$  [88],  $t$  is the thickness of the SC disk,  $\eta$  is a density parameter varies from 0 to 1.4 depending on flux pin-distribution and coherence length. Magnetic field fluctuation,  $\delta B$ , along certain directions gives rise to viscous damping along these directions. Oscillation of a magnet along  $z$ , for example, creates field fluctuations along  $z$  and also orthogonal directions due to modes couplings in the system. Therefore, excitation of the vertical mode gives rise to magnetic field fluctuation in different directions. Field fluctuation can give rise to a viscous force (through nonlinear damping) or residual mode excitation (through off-resonant driving). The former can cool the mode and the latter can heat it.

The viscous force for an oscillating magnet of frequency  $\omega_m$ , and amplitude  $A$ , can be written as

$$F_v(t) = -\frac{2\delta E_0 V}{A^2 \omega_m} \dot{u}(t). \quad (5.16)$$

and its spectrum then becomes

$$F_v(\omega) = K(\omega)u(\omega), \quad (5.17)$$

where  $K(\omega) = -i2\delta E_0 V \omega / (A^2 \omega_m)$ . When residual excitation is not negligible, we can replace  $u$  with  $u + \delta u$ , where  $\delta u$  is amplitude fluctuation caused by the off-resonant drive.

By re-arranging  $u(\omega)$  in Eq. 5.13 and neglecting off-resonance excitations, we can rewrite the equation for the displacement spectrum as :

$$u(\omega) = \chi_{eff}(\omega) F_{th}(\omega). \quad (5.18)$$

The effective susceptibility is defined as:

$$\chi_{eff}(\omega) = \frac{\chi(\omega)}{1 - \chi(\omega)K(\omega)} = \left\{ m[\omega_m^2 - \omega^2 + i(1 + \beta)\gamma_m \omega] \right\}^{-1}. \quad (5.19)$$

where  $\beta = 2\delta E_0 V / (mA^2 \omega_m \gamma_m)$ . The spectrum of the oscillations obtained from Eq. 5.18 is then

$$S_u(\omega) = |\chi_{eff}(\omega)|^2 S_F^{(th)}(\omega). \quad (5.20)$$

Using the equipartition theorem:

$$\frac{1}{2} m \omega_m^2 \sigma_u^2 = \frac{1}{2} k_B T_{eff} \quad (5.21)$$

we can derive the effective mode temperature,  $T_{eff}$  in relation to the variance of displacement as

$$T_{eff} = \frac{m \omega_m^2}{k_B} \int_{-\infty}^{+\infty} \frac{S_u(\omega)}{2\pi} d\omega. \quad (5.22)$$

Assuming the heating mode (where external modulation force is parked) is far detuned from the cooling mode ( $\delta u \ll 1$ ), we can have

$$T_{eff} \simeq \frac{T}{1 + \beta}. \quad (5.23)$$

In this case, the effective dissipation rate of the mode can also be written as  $\gamma_{eff} = (1 + \beta)\gamma$ . To estimate  $\beta$ , we can calculate magnetic field fluctuation  $\delta B$  along  $z$  direction using Eq.5.10. A fraction of this fluctuation will be coupled to the  $u$  mode (i.e.  $\delta B_z = \zeta \delta B_u$ ) that defines  $\delta E_0$  in the  $\beta$  coefficient. Comparing experimental value of  $\beta \simeq 10$  we find this fraction to be  $\zeta \simeq 0.1$ .

In practice, the residual excitation of the cooling mode bounds the lowest mode temperature that can be achieved using the nonlinear damping mechanism. When  $\delta u$  is not negligible, the effective mode temperature then becomes

$$T_{eff} = \frac{T}{1 + \beta} + T_0 \quad (5.24)$$

where

$$T_0 \simeq \frac{\beta^2}{1 + \beta} \eta_{ex} T \quad (5.25)$$

and the residual excitation energy relative to the thermal excitation is defined as

$$\eta_{ex} = \frac{m\omega_m^2 \gamma_m S_{\delta u}}{2k_B T}. \quad (5.26)$$

Here  $S_{\delta u} = \langle |\delta u|^2 \rangle$  is the time average of fluctuations in the cooling mode,  $\delta u$ , caused by the off-resonant excitation.

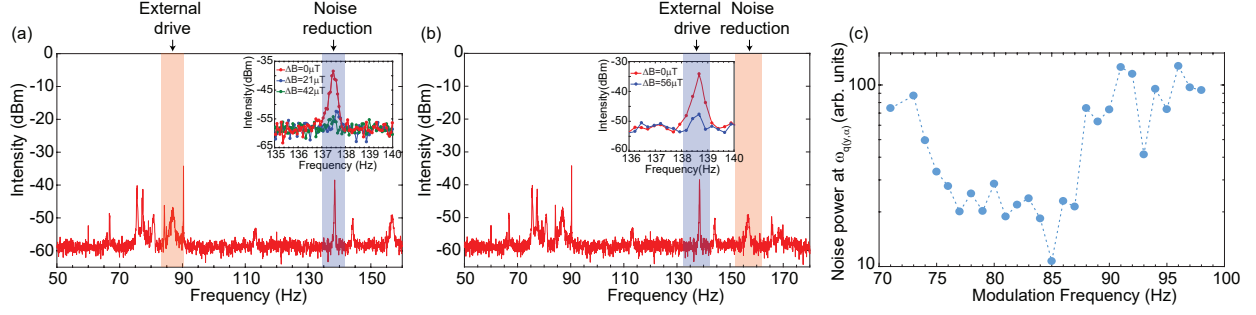


**Figure 5.14.** (a) and (b) Cooling of mechanical vibrations at  $\omega_{q(y,\alpha)} \simeq 138\text{Hz}$ , via resonant excitation of  $\omega_z$  and  $\omega_{u(x,\theta)}$  modes, respectively. Inset shows the cooled modes when different magnetic excitation amplitudes ( $\Delta B$ ) are applied. (c) The normalized vibrational intensity noise of  $\omega_{q(y,\alpha)}$  as a function of modulation frequency for the fixed  $\Delta B = 56\mu\text{T}$  applied to the driving coil. The dotted line is a guide to the eye.

## 5.12 Vibrational Noise Reduction Caused by Nonlinear Damping and mode Coupling

In our experiments, when the vertical mode ( $z$ ) is excited,  $\delta B$  along the orthogonal directions (e.g.  $\omega_{u(x,\theta)}$ ) also changes, which introduces vortex-vortex interaction leading to non-trivial dissipation of the flux motion [213]. This effect can then increase the damping of the orthogonal mode without increasing its vibrational amplitude. In the thermal noise limit, the mode temperature can be calculated using the cold damping theory [214]. The effective mode temperature is then given by  $T_{eff} \simeq \frac{T}{1+\beta}$ , where  $\beta \propto \frac{\delta E_0}{\omega_m \gamma_m}$ , and  $\omega_m$  and  $\gamma_m$  are center frequency and linewidth of the damped mode. This result is obtained in the limit that the excited mode (i.e. the frequency at which the external modulation force is applied) is far detuned from the cooled mode. In this case, the effective linewidth of the cooled mode can be written as  $\gamma_{eff} = (1 + \beta)\gamma_m$ . In practice, the residual excitation of the damped mode limits the lowest mode temperature that can be achieved using the nonlinear damping mechanism. The modified effective mode temperature then becomes  $T_{eff} = \frac{T}{1+\beta} + T_0$ , where  $T_0 \simeq \frac{\beta^2}{1+\beta} \eta_{ex} T$  and  $\eta_{ex}$  is the ratio of the residual excitation energy to the thermal energy.

Fig. 5.14 shows the result of cooling a mechanical mode of the mirror by heating or exciting another resonant mode. To the best of our knowledge, this is the first time such a cooling phenomenon has been reported. We have observed that the oscillation amplitude



of the mode at  $\omega_{q(y,\alpha)} = 138\text{Hz}$  is suppressed when the external magnetic field excitation is resonant with either the vertical oscillation mode of the mirror ( $\omega_z = 85\text{Hz}$ ) or the coupled mode  $\omega_{u(x,\theta)} = 158\text{Hz}$  (see Fig. 5.14 (a) and (b)). As the magnetic modulation ( $\Delta B$ ) amplitude of the external excitation increases, the mechanical vibrational intensity of the coupled mode  $\omega_{q(y,\alpha)}$  is suppressed by  $>17\text{dB}$ . Fig. 5.14 (c) shows the normalized intensity of the coupled mode  $\omega_{q(y,\alpha)}$  as a function of modulation frequency. We have observed no clear cooling effect when the modulation frequency is more than a few Hz away from the resonance frequency. Moreover, we have also observed that multiple modes ( $\omega_{q(y,\alpha)}$  and  $\omega_{u(x,\theta)}$ ) can be simultaneously cooled, although with different efficiencies, by exciting the vertical mode.

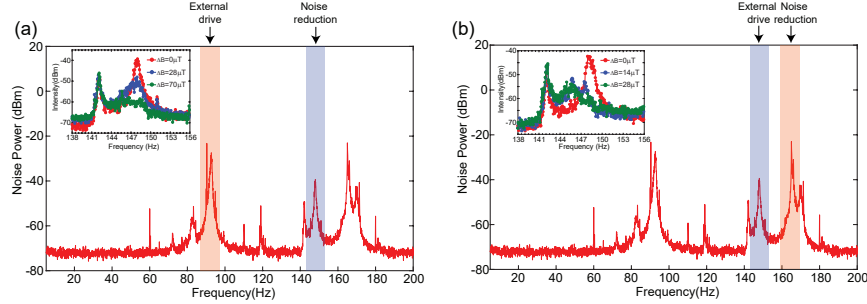


**Figure 5.15.** Observation of multi-mode cooling at different magnetic modulation voltages (proportional to  $\Delta B$ ) introduced by the driving coil at  $\omega_z = 90\text{Hz}$ . The vibrational spectra are vertically shifted for different modulation amplitudes for clarity. Simultaneous cooling of modes at  $148\text{Hz}$  and  $164\text{Hz}$  can be seen.

Fig. 5.15 shows data for a different experimental run where Qs are lower and we see a similar cooling effect as the one presented in the main text. The cooling of  $\omega_{q(y,\alpha)}$  mode is seen when the external magnetic excitation is applied at either  $\omega_z$  or  $\omega_{u(x,\theta)}$  frequencies. Here the noise power of the coupled mode ( $\omega_{q(y,\alpha)}$ ) has been reduced by about two orders of magnitudes when we externally drive the magnetic mirror at the frequency of  $85\text{Hz}$  ( $z$  mode) or  $164\text{Hz}$  ( $\omega_{u(x,\theta)}$  mode) at different magnetic modulation amplitudes,  $\Delta B$ . However, since there is a possibility that the vibrational noise reduction of one mode could be the result of a reduced detection efficiency when strongly exciting the other mode, we carefully confirmed this damping/cooling phenomenon we observed and eventually, we ruled the possibility out for the following reasons, 1) in the case of excitation-induced loss of sensitivity, we expect

the amplitude of oscillation to decrease but the linewidth should not change. The fact that we have increased damping, as also supported by the damping theory mentioned above, suggests that the damping of the mode occurs; 2) the external sinusoidal excitation is unlikely to change the equilibrium position of the levitated object. This is verified using the DC signal from the quadrant detector. The quadrant detector has three outputs, one for the intensity sum of pixels, one for the intensity difference of the horizontal pixels, and one for intensity difference of the vertical pixels. We would expect that change in sensitivity to be accompanied by either change in the intensity sum signal, or the change in the width of the beam at the detector location. The sensitivity of the quadrant detector itself depends on the light spot size on the detector, as shown in Eq. 5.9. But the truth is we do not observe the change in the intensity sum signal from the quadrant detector and we remain the beam size the same during the experiment. Also, we find that the light spot size is unlikely to be changed at the detector location by exciting one mechanical mode of the levitated mirror; 3) the reduced detection efficiency in one mode by exciting another mode could be possible if the objects being measured produce scattered light whose detected intensity could change nonlinearly with orientation and position. Using a flat and high reflective mirror ensures that small mirror oscillation or displacement does not result in scattering (e.g. from the edges), which could be the case when particles smaller than the beam size are used; 4) In our experiment, the linewidths and center frequencies of the damped modes both can be clearly determined as shown in Fig. 5.14 and 5.15. For the mechanical modes of the levitated mirror, we observed not only their vibrational intensities reduce and linewidths increase but also their frequency shift during the damping process. This is one typical signature of cold damping as reported in Refs. [215], [216]. Therefore, the driven controlled dissipation phenomenon we observed on this superconducting levitated magnetic mirror is not caused by the reduced detection efficiency but the magnetic inhomogeneity of the mirror which causes the magnetic vortex-vortex interaction between the driven and damped modes.

At elevated background excitations (e.g. seismic noise), the increased damping reduces the mechanical Q factors (See Fig. 5.13(b)). This effect has also been observed with superconducting levitated magnetic particles [75]. Results of Fig. 5.16 (a) and (b) were obtained in an experimental run where mechanical modes show higher dissipation rates (lower Qs).

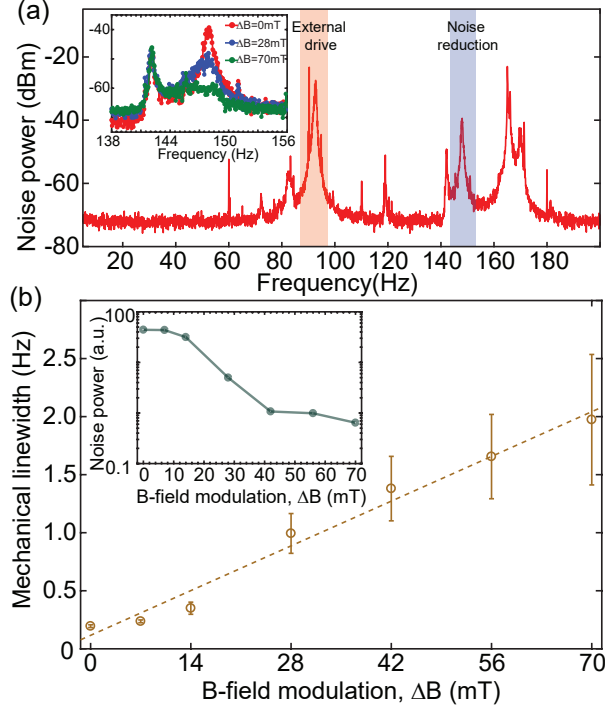


**Figure 5.16.** (a) The vibrational spectrum with heating and cooling modes indicated at  $\omega_z$  and  $\omega_{q(y,\alpha)}$ , respectively. Inset shows the cooling mode ( $\omega_{q(y,\alpha)}$ ) for different external magnetic modulation amplitudes ( $\Delta B$ ) induced by the current modulation in the coil. (b) The measured linewidth of  $\omega_{q(y,\alpha)}$  mode as a function of  $\Delta B$ . The inset shows the normalized noise power of  $\omega_{q(y,\alpha)}$  mode as a function of  $\Delta B$ . The line in the inset is a guide to the eye.

Here we also observe a similar cooling phenomenon as in Fig. 5.14. The low-Q vibrational spectrum in Fig. 5.16 (a) enables us to accurately determine the linewidth and mode temperature of  $\omega_{q(y,\alpha)}$ , which is no longer limited by the resolution bandwidth of our measurement. Fig. 5.16 (b) shows that the fitted experimental linewidth of  $\omega_{q(y,\alpha)}$  linearly increases with the magnetic field modulation amplitude ( $\Delta B$ ). The linear change was also predicted by the collective weak-pinning theory [209]. As  $\Delta B$  increases from 0 to  $70\mu T$ , the vibrational noise power of the coupled mode ( $\omega_{q(y,\alpha)}$ ) reduces by about two orders of magnitude while its linewidth increases by an order of magnitude. From Fig. 5.16 (b), we estimate  $\beta = 10 \pm 2$ . Also, using the equipartition theorem we can calculate an effective noise reduction factor of 10, in agreement with  $\beta \simeq 10$  obtained from the low-Q mechanical modes (Fig. 5.16 (a)). In experimental runs where  $\omega_{q(y,\alpha)}$  mode shows higher Q ( $> 4$  times higher), the effective

temperature reduction factor obtained is about 60 (Fig. 5.14 (a)). This again agrees with the theory described above, suggesting that  $\beta$  is inversely proportional to  $\gamma_m$ . In our experiment, we note that the mechanical vibrations of the superconducting levitated magnetic mirror are not thermal-noise limited since the seismic noise is  $>4$  orders of magnitude higher than the thermal noise in the frequency range of interest. Because of the broadband nature of the seismic noise over the frequency range of interest, the cold damping theory can still be used to model the cooling process by assuming an effective mode temperature ( $T_{eff}$ ).

The cooling is limited by off-resonant excitations and residual heating due to mode coupling to externally-excited modes. The geometry of the levitated magnetic mirror defines the strength of the inhomogeneity and mode coupling in the system, thus playing an important role in the cooling process. The magnetic mirror with diametrical magnetization used in our experiment provides the asymmetry needed to have distinct mechanical modes. This is accompanied by an inhomogeneous field arising from the oscillating magnetic mirror. While large inhomogeneity enhances the cooling process for certain modes, the low inhomogeneity of certain oscillations gives rise to ultra-high-Q resonances in the system [75]. Our experiment helps to better understand the nature of mode coupling and nonlinear dissipation and suggests a way to use such mechanisms to cool the vibrational noise at certain modes by heating or exciting other modes. Precision magnetic sensing [165], [217], coherent magnetic-optical trapping [173], [218], [219], and ground-state cooling of micro-scale magnets [203] are among the applications of superconducting levitation studied here. An in-depth theoretical understanding of off-resonance dissipation in multi-mode systems is needed to guide future experiments designed for ultra-high Q and/or low noise superconducting levitation.

### 5.13 Potential Application for Superconducting levitated HR mirror

Apart from the fundamentally interesting and new approach to reduce the vibrational noise of the superconducting levitated objects, the enhanced gravity and magnetic sensing are among the applications of utilizing the superconducting levitated HR mirror.

Previously, it has been proposed that scattering-free levitation can be achieved using intra-cavity optical forces [173]. The authors have studied such trapping mechanisms ex-

perimentally and realized that 3D trapping in this way is challenging. The addition of a superconducting trap can help stabilize the mirror in all directions while in the cavity direction the optical radiation pressure force can dominate the oscillation dynamics. The trapping in the horizontal plane can be achieved by the superconducting trap and the controlled driven dissipation or “cooling by heating” phenomenon found in this chapter enables us to reduce the vibrational noise. The optical spring effect can provide the restoring force for the oscillation, and the position of the mirror would be self-locked to the laser frequency. The inherently active locking of the cavity length arises from the self adjustment of cavity power when light is red-detuned to push/pull the mirror to the equilibrium point. Remarkably, no light is scattered in this case and the fundamental limit on  $\omega \times Q$  can be extended by  $>4$  orders of magnitude compared to the currently existing approaches. At  $10^{-6}$  mbar pressures, background-gas dissipation rate is  $<10$  mHz. A laser with fractional intensity noise  $< 10^{-5}$  provides 10s of seconds of trapping time for a mirror with  $\omega_m=500$  kHz. This high frequency can be achieved by the optical spring effect of a cavity with the finesse of 1000 and is no longer determined by the magnetic trap. Moreover, the anti-damping due to the blackbody radiation is  $<\text{mHz}$ . This can enable implementation of: 1) the first coherent levitation, 2) optical spring as the sole oscillator clamp, 3) broadband room-temperature phonon trapping and 4) large-surface optomechanics for enhanced multimode/broadband sensing. The platform studied here offers a variety of measurements with exquisite sensitivity. Below we provide more details about how such an experiment can be designed.

Fig. 5.17 shows the proposed experimental setup. Based on this experimental plan, we have built such a cavity using a fixed mirror and the levitated mirror. The cavity spectrum is shown in Fig.5.18. Such a platform enables us to study optical spring effect, scattering-free optical levitation [173], and in principle, it can enhance the sensitivity of our measurements such as the magnetic sensing [165]. The high mechanical noise of the levitated mirror, however, makes it difficult to create a stable cavity. The driven controlled dissipation results or “cooling by heating” phenomenon would pave the way for damping the mechanical noise and stabilizing the cavity. Our calculation also shows that at low mechanical noise, the optical spring effect of intra-cavity light takes over and it can create a 1D trap for the mirror ( self-stabilized and scattering-free levitation). Once the low-

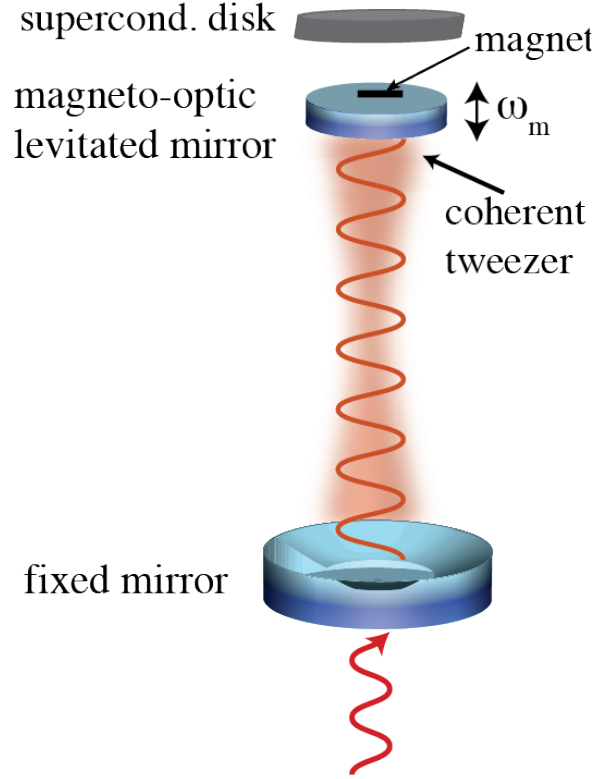


**Figure 5.17.** Schematics of coherent levitation of a mirror on an optical spring self- locked to the laser frequency. A combination of magneto-optical levitation, laser cooling and cavity restoring force creates a scattering-free tweezer for the mirror. A micro- disk mirror with magnetic coating is trapped in x-y directions using a superconducting disk while optical force of an intra-cavity field coherently traps the mirror in the  $z$  direction.

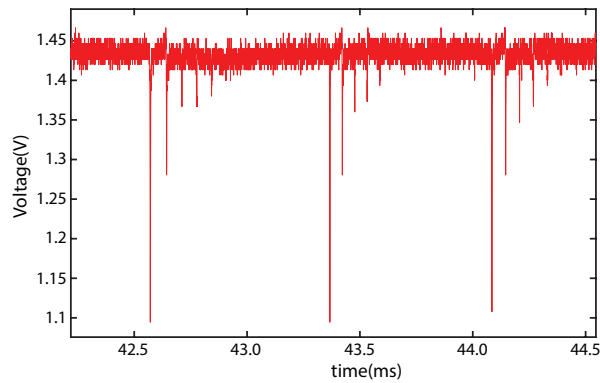


**Figure 5.18.** Cavity transmission data obtained from a levitated cavity mirror

frequency (less than 200Hz in our case) mechanical noise can be damped using the driven controlled dissipation approach discussed above, the optical radiation pressure force of the cavity may enable, in principle, coherent optical trapping of the mirror in the direction of the cavity axis. Assuming the vibration amplitude of the levitated magnetic mirror can be damped to less than 10 nm at 20Hz, the optical trapping potential of the cavity field with the finesse of 400 can exceed the kinetic energy of the mirror with a mass of 10mg. Then the levitated magnetic mirror can be optically trapped in one direction while trapping in other directions is achieved by the superconducting trap. Assuming one mechanical mode of the levitated mirror along the cavity axis has the resonant frequency of  $f = 15\text{Hz}$ , then the optical spring effect of the cavity field can increase the mirror frequency along the cavity axis from  $f = 15\text{Hz}$  to  $f > 300\text{Hz}$  where the other mechanical noise associated with the environment and the levitated mirror are absent, which enables the study of optomechanical interactions and sensing using macroscopic objects.

Other than optomechanical magnetometry and gravity sensing, the study of quantum mechanical motion of macroscopic objects is another application of the superconducting levitated cavity mirror. For example, in the vertical-cavity geometry, the coherent trapping of the mirror using the intra-cavity field enables sensing the change in the gravitational acceleration,  $g$ , by shot-noise limited measurement of the intensity of the out-coupled cavity light. Because the external forces can change the equilibrium position of the mirror and their effects can be predominantly measured by a change in the cavity power ( $P_c$ ), i.e.  $dg/g = dP_c/P_c$ , that is limited by the shot noise. Moreover, in the vertical geometry to build the cavity using the levitated mirror, the common-mode vertical vibrations of the both cavity mirrors can dramatically enhance the mechanical stability of the cavity.

## 5.14 Summary

In conclusion, we study mode coupling and dissipation mechanisms in a levitated magnetic mirror above a superconductor. We model vibrational modes of the mirror and test mode coupling between different degrees of freedom of the levitated object. We observe that the nonlinear dissipation in superconducting levitation systems could be harnessed to control

and cool certain mechanical modes. We show that via the excitation of certain modes, the nonlinear damping can suppress the thermal/mechanical vibrational noise in the orthogonal modes. In this way, a maximum cooling factor of about 60 was achieved. To the best of our knowledge, this is the first time such a cooling mechanism is reported. As such cooling does not rely on the signal-to-noise ratio of detection (as is the case for feedback cooling), the method can enable cooling certain modes independent of their detection and position in the spectrum.



## 6. SUMMARY AND FUTURE WORK

### 6.1 Current Work Summary

In the present thesis, we have systematically investigated light-matter interactions experimentally and theoretically based on the atomic and mechanical systems. We mainly focus on studying the optomechanical hybrid platform which is made of one superconducting levitated magnetic mirror. The effective light-atom and light-oscillator interfaces have been built for controlling the atomic and mechanical oscillators using light for optical memory and sensing applications.

#### 6.1.1 On-chip Integration of Er-implanted Lithium Niobate Crystal with Silicon Photonics

Implementation of scalable quantum photonic networks requires the integration of compatible photon sources and quantum memories. On-chip silicon photonic elements operating at the telecommunication wavelengths are attractive for the implementation of single-photon sources. Moreover, rare earth (RE) crystals have been used to implement solid-state quantum memories at these wavelengths. As one of the RE crystalline hosts, lithium niobate (LN),  $\text{LiNbO}_3$ , is very attractive and has recently emerged as a viable material for heterogeneous photonic system integration due to its electro-optic, nonlinear, and acousto-optic properties as well as its integration capability. Integration of sources and memories on a single platform capable of carrying multiplexing tasks is a grand challenge for future quantum communication. We take steps towards the realization of such a quantum photonic platform by directly integrating rare earth implanted lithium niobate crystals with silicon photonics and study light-atom interactions on this platform. To be more specific, we deterministically activate LN crystals by ion implantation and precise control of annealing and implantation parameters to achieve homogeneous light-atom coupling. Using a direct bonding technique, we integrate Er-implanted LN crystal with Si-SiN waveguide and micro-resonator, and study evanescent mode coupling between the emission mode of Er atoms in LN crystal and Si-SiN waveguide and cavity modes. The integration approach is scalable and enables low-cost fab-

rication and chip-to-chip integration. The platform enables scalable, telecomm compatible, versatile, and multifunctional design of future quantum photonic networks [91].

### 6.1.2 Optomechanical Frequency Comb Memory

The hybrid optomechanical systems have been considered as an advanced platform for quantum information storage and processing. In these systems, the cooperative behavior and phase-synchronization in an ensemble of mechanical oscillators enable enhanced and broadband optomechanical interactions. Typically, large inhomogeneous broadening in the mechanical frequency of mechanical oscillator ensemble limits the observation of cooperative coupling between them due to the imprecision in nanofabrication techniques. We use an optomechanical platform based on weakly coupled optomechanical arrays collectively coupled to an external laser drive to implement the coherent optical storage. By tailoring the optomechanical interactions, we show that instantaneous phase matching in a form of photon-phonon echo can result in cooperative optomechanical coupling. A novel method is proposed by using the inhomogeneous broadening to our advantage based on the concepts and techniques developed in atomic physics. The proposed method does not require precise mechanical frequency tuning, overcoming the current limitation in the nanofabrication of identical optomechanical arrays. Using numerical simulation, we demonstrate the broadband coherent optical light storage based on the collective photon-phonon dynamics. An optomechanical memory of this kind enables information storage over a wide band of wavelengths, including the telecommunications band, and importantly, can be integrated into the silicon photonic networks [41].

### 6.1.3 Superconducting Levitation of a mg-Scale Cavity Mirror

Towards understanding the boundaries of quantum theory as an outstanding question in modern physics, we work towards the implementation of “hybrid coherent” levitation on an optical spring. For the first time, we demonstrate the superconducting levitation of a cavity mirror and observe magnetic and optical forces. We achieve a magnetic field sensitivity of  $370 \text{ pT}/\sqrt{Hz}$  and observe the signatures of the coherent optical trapping via the intra-cavity

field. The work is an important experimental step in achieving the coherent optical trapping previously proposed [PRL 111, 183001 (2013)]. Compared to the recent experimental demonstration of cooling a nanosphere via coherent scattering [PRL 122, 123602 (2019)], the present work considers objects of about 10 orders of magnitude larger. The demonstration of optical resonance of the suspended cavity mirror is significant for the various reasons: 1) a stable cavity resonance can enhance the measurement sensitivity of the mirror's position in both DC and AC regimes, 2) the optical spring can be more than one order of magnitude stiffer than the superconducting trap, enabling the study of optomechanical effects, and 3) the intra-cavity optical field can potentially trap the mirror along the direction of the cavity axis through AC radiation pressure force or the optical spring effect. Three spectacular applications of the built platform include: 1) precise gravitational force sensing, 2) the first realization of micro-macro entanglement, and 3) the first test of the semi-classical theory of gravity [165].

#### **6.1.4 Driven Nonlinear Damping and Mode Coupling in a Superconducting Levitated Magnetic Mirror**

Macroscopic mechanical oscillators are attracting attention for precision sensing (e.g. LIGO) and observing quantum phenomena (e.g. ground state cooling). Observation of quantum effects in acoustic vibrations of nanostructures, and macroscopic volumes of superfluid liquid are examples where boundaries of quantum and classical mechanics can be studied. Compared with acoustic waves, the center-of-mass motion of micro and macro-scale objects provides a different toolbox for applications such as gravity sensing. Optical tweezers have been proven useful in studying the CM motion of objects ranging from a single trapped neutral atom to nanospheres. Similarly, other kinds of levitation techniques, such as superconducting levitation, enable us to isolate vibrations of levitated particles or objects and reduce clamping loss to achieve ultra-high Q mechanical oscillations. Although the phenomenon of superconducting levitation in the steady state is well known, the dynamic nature of superconducting trapping and its dissipation mechanisms are not well understood .

We levitate a millimeter-sized magnetic mirror and study the mode coupling and nonlinear dissipation mechanism of such an oscillating rigid body in vacuum conditions. For the first time, we show that the vibrational noise of the mirror can be suppressed by a factor of more than 60 via an off-resonance drive. We refer to this as the controlled driven dissipation or a “cooling-by-heating” phenomenon, which relies on the nonlinear damping inherent in the superconductor to reduce the vibrational noise of the levitated magnet. This unique controlled damping technique offers a new perspective to further study the suppression of thermal vibrational noise of levitated oscillators. Our experimental results could be viewed as an important step towards such unconventional vibrational noise suppression, and it can in principle be applied to micro-scale to macro-scale objects [197].

## 6.2 Future Work Plan

Since we are now focusing on studying the optomechanical platform based on the superconducting levitated millimeter-scale magnetic mirror in vacuum for ultrasensitive sensing applications, our future work mainly includes how to improve and enhance the sensitivity of the levitated mirror in sensing such as force, torque, inertia, and electrical field. We will take the following approaches to reduce the vibrational noise of the superconducting levitated mirror and therefore improve its sensitivities.

### 6.2.1 Reducing Vibrational Noise of Superconducting Levitated Magnetic Mirror

As we mentioned earlier, the vibrational noise of the superconducting levitated magnetic mirror in our case is limited by the seismic noise, which is 4 orders of magnitude larger than the thermal noise in the frequency range of interest (0 - 200Hz). The magnitude of seismic noise depends on the lab location and nearby noise sources around the experimental setup. In order to reduce the seismic noise, since we have already suspended the optical table, one natural way is to decouple the superconducting levitation experimental setup from the seismic vibrations by suspending the whole experimental setup including the entire vacuum chamber on a soft spring system. The noise caused by the gas collisions can be ignored in our

experiment because the magnet is levitated under high vacuum conditions ( $\sim 10^{-8}$  Torr). Other types of noise caused by eddy currents and the magnetic hysteretic should also be considered to be reduced as much as possible. Since the magnet itself and its coatings are metallic, the eddy current dissipation can not be easily ignored, but it can be significantly reduced by using uncoated magnets. The magnetic noise associated with the environment such as the magnetic field from the earth could be mitigated by using a magnetic shield around the superconducting levitation experimental setup. To reduce the hysteresis noise from the magnet, it is better to levitate the magnet which has less magnetic inhomogeneity.

### 6.2.2 Applying Passive and Active Cooling Methods to Improve Sensitivity

As a powerful tool to reduce the amplitude and the effective temperature of the mechanical oscillator, active feedback cooling takes the motion information of the mechanical oscillator to apply an external force that damps the motion of the oscillator. The quadrant detector could be used to measure and record the motions of the superconducting levitated magnetic mirror in our experiment. And then after applying a  $\pi/2$  phase shift to the recorded signal, we can feedback the signal to the current controller. A current coil can be placed nearby the levitated mirror to implement the magnetic feedback force to the mirror. By modulating the current in the current controller using the signal of the levitated mirror's motion with a  $\pi/2$  phase shift, it would create a force that opposes the motion of the levitated mirror. Therefore, the mirror's vibrational noise would be reduced, which is helpful to improve the sensitivity of the mirror for sensing applications. The active feedback cooling method has also been widely used for cooling the optically levitated nanoparticles to closely reach their quantum ground state [68], [220] and the nanowires to enhance the sensitivity for sensing applications [221].

### 6.2.3 Building a Cavity Based on Superconducting Levitated Mirror to Improve Sensitivity

It is possible that the vibration noise of the superconducting levitated mirror can be reduced to less than 10 nm at the resonant frequency of below 100Hz via suspending the whole

experimental setup, the active feedback/passive cooling as well as the controlled driving cooling method we discussed in the present thesis. For the built Fabry-Pérot cavity with the levitated mirror as the end mirror of the cavity, the optical trapping potential of the cavity field of finesse 400 can exceed the kinetic energy of the mirror with a mass of 10mg. The mirror can be optically trapped in one direction while trapping in other directions is achieved by the superconducting trap. The optical spring effect of the cavity field, can increase the mirror frequency along the cavity axis from  $f_y = 15\text{Hz}$  to  $f_y > 300\text{Hz}$  where other mechanical noise is absent enabling study of optomechanical interactions and sensing using macroscopic objects. This will make the magnetic sensitivity increase from a few hundred  $pT/\sqrt{Hz}$  without the cavity built to  $\sim fT/\sqrt{Hz}$  where the cavity is built based on the levitated mirror. Apart from optomechanical magnetometry, gravity sensing and the study of quantum mechanical motion of macroscopic objects are other applications of the levitated cavity mirror. In the vertical cavity geometry, for example, the coherent trapping of the mirror using the intra-cavity field enables sensing the change in the gravitational acceleration,  $g$ , by shot-noise limited measurement of the intensity of the out-coupled cavity light. External forces can change the equilibrium position of the mirror and their effects can be predominantly measured by a change in the cavity power ( $P_c$ ), i.e.  $dg/g = dP_c/P_c$ , that is limited by the shot noise. Moreover, in the vertical geometry, the common-mode vertical vibration of the cavity mirrors can dramatically enhance the mechanical stability of the cavity.

#### 6.2.4 Toward Precision Sensing Gravity with Levitated Mirror

LIGO as the interferometric gravitational wave detector has been reported to observe a transient gravitational-wave signal in 2016 with kilogram-scale cavity mirrors [222]. An optically trapped dielectric nanoparticle with a mass of  $\sim 10^{-15}g$  has been reported to be cooled down to its quantum ground state using laser cooling technique [68] for potential applications in sensing gravitational source masses in the future. Even though quantum experiments have been realized for small and low-mass oscillators, gravity has only been observed in relatively large-mass ( $\sim kg$ ) objects [223], [224] since the gravitational force

is minuscule. It is generally difficult to observe gravitational effects generated by small objects. Due to the development of micro-mechanical devices with unprecedented sensitivity in the recent decades [225], [226], sensing gravity between  $mm$ -size objects with  $mg$ -scale is possible in principle. The intermediate system with a mass of  $\sim mg$  for the applications of high-energy physics such as searching for dark matter and detecting gravitational waves has rarely been reported [173], [227], [228]. A small mirror with a mass of less than 1mg optically levitated by a tripod was proposed for precision gravitational field sensing [173]. Recently, an optically trapped 7mg pendulum with a displacement noise of better than  $\sim 10^{-16}m/\sqrt{Hz}$  has been shown to be able to measure the gravitational coupling between milligram-scale objects [228].

With further reducing the seismic noise and then the thermal noise, our superconducting levitated  $mg$ -scale mirror could be a novel potential platform for precision gravity sensing. The macroscopic mirror as a sensing object can provide a large interaction cross section and its low-noise trapping even close to DC could enhance the sensitivity of low-frequency measurements. The interaction and SNR of sensing can significantly be increased when two mirrors (one levitated and the other one fixed) form a cavity [173].

## REFERENCES

- [1] M. J. Yap, J. Cripe, G. L. Mansell, T. G. McRae, R. L. Ward, B. J. Slagmolen, P. Heu, D. Follman, G. D. Cole, T. Corbitt, *et al.*, “Broadband reduction of quantum radiation pressure noise via squeezed light injection,” *Nature Photonics*, vol. 14, no. 1, pp. 19–23, 2020.
- [2] M. K. Bhaskar, R. Riedinger, B. Machielse, D. S. Levonian, C. T. Nguyen, E. N. Knall, H. Park, D. Englund, M. Lončar, D. D. Sukachev, *et al.*, “Experimental demonstration of memory-enhanced quantum communication,” *Nature*, vol. 580, no. 7801, pp. 60–64, 2020.
- [3] A. Choudhary, Y. Liu, B. Morrison, K. Vu, D.-Y. Choi, P. Ma, S. Madden, D. Marpaung, and B. J. Eggleton, “High-resolution, on-chip rf photonic signal processor using brillouin gain shaping and rf interference,” *Scientific reports*, vol. 7, no. 1, pp. 1–9, 2017.
- [4] W. Liu, M. Li, R. S. Guzzon, E. J. Norberg, J. S. Parker, M. Lu, L. A. Coldren, and J. Yao, “A fully reconfigurable photonic integrated signal processor,” *Nature Photonics*, vol. 10, no. 3, pp. 190–195, 2016.
- [5] R. Wolf, Y. Jia, S. Bonaus, C. S. Werner, S. J. Herr, I. Breunig, K. Buse, and H. Zappe, “Quasi-phase-matched nonlinear optical frequency conversion in on-chip whispering galleries,” *Optica*, vol. 5, no. 7, pp. 872–875, 2018.
- [6] X. Guo, C.-L. Zou, H. Jung, and H. X. Tang, “On-chip strong coupling and efficient frequency conversion between telecom and visible optical modes,” *Physical review letters*, vol. 117, no. 12, p. 123 902, 2016.
- [7] D. M. Lukin, C. Dory, M. A. Guidry, K. Y. Yang, S. D. Mishra, R. Trivedi, M. Radulaski, S. Sun, D. Vercruysse, G. H. Ahn, *et al.*, “4h-silicon-carbide-on-insulator for integrated quantum and nonlinear photonics,” *Nature Photonics*, vol. 14, no. 5, pp. 330–334, 2020.
- [8] Y. Kurosaka, S. Iwahashi, Y. Liang, K. Sakai, E. Miyai, W. Kunishi, D. Ohnishi, and S. Noda, “On-chip beam-steering photonic-crystal lasers,” *Nature Photonics*, vol. 4, no. 7, pp. 447–450, 2010.
- [9] M. Sieger and B. Mizaikoff, *Toward on-chip mid-infrared sensors*, 2016.
- [10] Z. Cheng, C. Ríos, W. H. Pernice, C. D. Wright, and H. Bhaskaran, “On-chip photonic synapse,” *Science advances*, vol. 3, no. 9, e1700160, 2017.
- [11] M. Davanco, J. Liu, L. Sapienza, C.-Z. Zhang, J. V. D. M. Cardoso, V. Verma, R. Mirin, S. W. Nam, L. Liu, and K. Srinivasan, “Heterogeneous integration for on-chip quantum photonic circuits with single quantum dot devices,” *Nature communications*, vol. 8, no. 1, pp. 1–12, 2017.



- [12] T. Barwicz, M. R. Watts, M. A. Popović, P. T. Rakich, L. Socci, F. X. Kärtner, E. P. Ippen, and H. I. Smith, “Polarization-transparent microphotonic devices in the strong confinement limit,” *Nature Photonics*, vol. 1, no. 1, pp. 57–60, 2007.
- [13] J. Prat-Camps, C. Teo, C. Rusconi, W. Wiecek, and O. Romero-Isart, “Ultrasensitive inertial and force sensors with diamagnetically levitated magnets,” *Physical Review Applied*, vol. 8, no. 3, p. 034002, 2017.
- [14] C. Timberlake, G. Gasbarri, A. Vinante, A. Setter, and H. Ulbricht, “Acceleration sensing with magnetically levitated oscillators above a superconductor,” *Applied Physics Letters*, vol. 115, no. 22, p. 224101, 2019.
- [15] M. T. Johnsson, G. K. Brennen, and J. Twamley, “Macroscopic superpositions and gravimetry with quantum magnetomechanics,” *Scientific reports*, vol. 6, no. 1, pp. 1–13, 2016.
- [16] L. Jiang, J. M. Taylor, K. Nemoto, W. J. Munro, R. Van Meter, and M. D. Lukin, “Quantum repeater with encoding,” *Physical Review A*, vol. 79, no. 3, p. 032325, 2009.
- [17] P. Van Loock, T. Ladd, K. Sanaka, F. Yamaguchi, K. Nemoto, W. Munro, and Y. Yamamoto, “Hybrid quantum repeater using bright coherent light,” *Physical review letters*, vol. 96, no. 24, p. 240501, 2006.
- [18] A. I. Lvovsky, B. C. Sanders, and W. Tittel, “Optical quantum memory,” *Nature photonics*, vol. 3, no. 12, pp. 706–714, 2009.
- [19] D. F. Phillips, A. Fleischhauer, A. Mair, R. L. Walsworth, and M. D. Lukin, “Storage of light in atomic vapor,” *Physical review letters*, vol. 86, no. 5, p. 783, 2001.
- [20] A. L. Alexander, J. J. Longdell, M. J. Sellars, and N. B. Manson, “Photon echoes produced by switching electric fields,” *Physical review letters*, vol. 96, no. 4, p. 043602, 2006.
- [21] S. Ritter, C. Nölleke, C. Hahn, A. Reiserer, A. Neuzner, M. Uphoff, M. Mücke, E. Figueroa, J. Bochmann, and G. Rempe, “An elementary quantum network of single atoms in optical cavities,” *Nature*, vol. 484, no. 7393, pp. 195–200, 2012.
- [22] H. P. Specht, C. Nölleke, A. Reiserer, M. Uphoff, E. Figueroa, S. Ritter, and G. Rempe, “A single-atom quantum memory,” *Nature*, vol. 473, no. 7346, pp. 190–193, 2011.
- [23] C. Kurz, M. Schug, P. Eich, J. Huwer, P. Müller, and J. Eschner, “Experimental protocol for high-fidelity heralded photon-to-atom quantum state transfer,” *Nature communications*, vol. 5, no. 1, pp. 1–5, 2014.

- [24] G. Fuchs, G. Burkard, P. Klimov, and D. Awschalom, “A quantum memory intrinsic to single nitrogen–vacancy centres in diamond,” *Nature Physics*, vol. 7, no. 10, pp. 789–793, 2011.
- [25] J.-S. Tang, Z.-Q. Zhou, Y.-T. Wang, Y.-L. Li, X. Liu, Y.-L. Hua, Y. Zou, S. Wang, D.-Y. He, G. Chen, *et al.*, “Storage of multiple single-photon pulses emitted from a quantum dot in a solid-state quantum memory,” *Nature communications*, vol. 6, no. 1, pp. 1–7, 2015.
- [26] X.-H. Bao, A. Reingruber, P. Dietrich, J. Rui, A. Dück, T. Strassel, L. Li, N.-L. Liu, B. Zhao, and J.-W. Pan, “Efficient and long-lived quantum memory with cold atoms inside a ring cavity,” *Nature Physics*, vol. 8, no. 7, pp. 517–521, 2012.
- [27] Y.-W. Cho, G. Campbell, J. Everett, J. Bernu, D. Higginbottom, M. Cao, J. Geng, N. Robins, P. Lam, and B. Buchler, “Highly efficient optical quantum memory with long coherence time in cold atoms,” *Optica*, vol. 3, no. 1, pp. 100–107, 2016.
- [28] B. Sparkes, J. Bernu, M. Hosseini, J. Geng, Q. Glorieux, P. A. Altin, P. K. Lam, N. Robins, and B. Buchler, “Gradient echo memory in an ultra-high optical depth cold atomic ensemble,” *New Journal of Physics*, vol. 15, no. 8, p. 085 027, 2013.
- [29] M. Hosseini, G. Campbell, B. M. Sparkes, P. K. Lam, and B. C. Buchler, “Unconditional room-temperature quantum memory,” *Nature Physics*, vol. 7, no. 10, pp. 794–798, 2011.
- [30] T. Zhong, J. M. Kindem, J. G. Bartholomew, J. Rochman, I. Craiciu, E. Miyazono, M. Bettinelli, E. Cavalli, V. Verma, S. W. Nam, *et al.*, “Nanophotonic rare-earth quantum memory with optically controlled retrieval,” *Science*, vol. 357, no. 6358, pp. 1392–1395, 2017.
- [31] Z.-Q. Zhou, W.-B. Lin, M. Yang, C.-F. Li, and G.-C. Guo, “Realization of reliable solid-state quantum memory for photonic polarization qubit,” *Physical review letters*, vol. 108, no. 19, p. 190 505, 2012.
- [32] K. Heshami, C. Santori, B. Khanaliloo, C. Healey, V. M. Acosta, P. E. Barclay, and C. Simon, “Raman quantum memory based on an ensemble of nitrogen-vacancy centers coupled to a microcavity,” *Physical Review A*, vol. 89, no. 4, p. 040 301, 2014.
- [33] M. Afzelius, C. Simon, H. De Riedmatten, and N. Gisin, “Multimode quantum memory based on atomic frequency combs,” *Physical Review A*, vol. 79, no. 5, p. 052 329, 2009.
- [34] N. Sinclair, E. Saglamyurek, H. Mallahzadeh, J. A. Slater, M. George, R. Ricken, M. P. Hedges, D. Oblak, C. Simon, W. Sohler, *et al.*, “Spectral multiplexing for scalable quantum photonics using an atomic frequency comb quantum memory and feed-forward control,” *Physical review letters*, vol. 113, no. 5, p. 053 603, 2014.

- [35] K. Stannigel, P. Komar, S. Habraken, S. Bennett, M. D. Lukin, P. Zoller, and P. Rabl, “Optomechanical quantum information processing with photons and phonons,” *Physical review letters*, vol. 109, no. 1, p. 013 603, 2012.
- [36] D. P. Lake, M. Mitchell, D. D. Sukachev, and P. E. Barclay, “Processing light with an optically tunable mechanical memory,” *Nature communications*, vol. 12, no. 1, pp. 1–9, 2021.
- [37] R. Teh, S. Kieseewetter, M. Reid, and P. Drummond, “Simulation of an optomechanical quantum memory in the nonlinear regime,” *Physical Review A*, vol. 96, no. 1, p. 013 854, 2017.
- [38] V. Fiore, Y. Yang, M. C. Kuzyk, R. Barbour, L. Tian, and H. Wang, “Storing optical information as a mechanical excitation in a silica optomechanical resonator,” *Physical review letters*, vol. 107, no. 13, p. 133 601, 2011.
- [39] V. Fiore, C. Dong, M. C. Kuzyk, and H. Wang, “Optomechanical light storage in a silica microresonator,” *Physical Review A*, vol. 87, no. 2, p. 023 812, 2013.
- [40] R. Teh, S. Kieseewetter, P. Drummond, and M. Reid, “Creation, storage, and retrieval of an optomechanical cat state,” *Physical Review A*, vol. 98, no. 6, p. 063 814, 2018.
- [41] X. Jiang, A. Nandi, D. Pak, and M. Hosseini, “Optomechanical frequency comb memory,” *Optics letters*, vol. 43, no. 20, pp. 4973–4976, 2018.
- [42] B. Abbott, R. Abbott, R. Adhikari, P. Ajith, B. Allen, G. Allen, R. Amin, S. Anderson, W. Anderson, M. Arain, *et al.*, “Ligo: The laser interferometer gravitational-wave observatory,” *Reports on Progress in Physics*, vol. 72, no. 7, p. 076 901, 2009.
- [43] J. Kepler, *1619. de cometis libelli tres*.
- [44] A. Ashkin, “Acceleration and trapping of particles by radiation pressure,” *Physical review letters*, vol. 24, no. 4, p. 156, 1970.
- [45] M. Merklein, B. Stiller, K. Vu, S. J. Madden, and B. J. Eggleton, “A chip-integrated coherent photonic-phononic memory,” *nature Communications*, vol. 8, no. 1, pp. 1–7, 2017.
- [46] J. W. Silverstone, D. Bonneau, K. Ohira, N. Suzuki, H. Yoshida, N. Iizuka, M. Ezaki, C. M. Natarajan, M. G. Tanner, R. H. Hadfield, *et al.*, “On-chip quantum interference between silicon photon-pair sources,” *Nature Photonics*, vol. 8, no. 2, pp. 104–108, 2014.
- [47] M. Zhang, L.-T. Feng, Z.-Y. Zhou, Y. Chen, H. Wu, M. Li, S.-M. Gao, G.-P. Guo, G.-C. Guo, D.-X. Dai, *et al.*, “Generation of multiphoton quantum states on silicon,” *Light: Science & Applications*, vol. 8, no. 1, pp. 1–7, 2019.

- [48] X. Lu, Q. Li, D. A. Westly, G. Moille, A. Singh, V. Anant, and K. Srinivasan, “Chip-integrated visible–telecom entangled photon pair source for quantum communication,” *Nature physics*, vol. 15, no. 4, pp. 373–381, 2019.
- [49] X. Zhang, B. A. Bell, A. Mahendra, C. Xiong, P. H. Leong, and B. J. Eggleton, “Integrated silicon nitride time-bin entanglement circuits,” *Optics letters*, vol. 43, no. 15, pp. 3469–3472, 2018.
- [50] L. Vivien and L. Pavesi, *Handbook of silicon photonics*. Taylor & Francis, 2016.
- [51] H. Jin, F. Liu, P. Xu, J. Xia, M. Zhong, Y. Yuan, J. Zhou, Y. Gong, W. Wang, and S. Zhu, “On-chip generation and manipulation of entangled photons based on reconfigurable lithium-niobate waveguide circuits,” *Physical review letters*, vol. 113, no. 10, p. 103 601, 2014.
- [52] E. Saglamyurek, N. Sinclair, J. Jin, J. A. Slater, D. Oblak, F. Bussieres, M. George, R. Ricken, W. Sohler, and W. Tittel, “Broadband waveguide quantum memory for entangled photons,” *Nature*, vol. 469, no. 7331, pp. 512–515, 2011.
- [53] D. Pak, H. An, A. Nandi, X. Jiang, Y. Xuan, and M. Hosseini, “Ytterbium-implanted photonic resonators based on thin film lithium niobate,” *Journal of Applied Physics*, vol. 128, no. 8, p. 084 302, 2020.
- [54] S. Wang, L. Yang, R. Cheng, Y. Xu, M. Shen, R. L. Cone, C. W. Thiel, and H. X. Tang, “Incorporation of erbium ions into thin-film lithium niobate integrated photonics,” *Applied Physics Letters*, vol. 116, no. 15, p. 151 103, 2020.
- [55] J. Wang, A. Santamato, P. Jiang, D. Bonneau, E. Engin, J. W. Silverstone, M. Lerner, J. Beetz, M. Kamp, S. Höfling, *et al.*, “Gallium arsenide (gaas) quantum photonic waveguide circuits,” *Optics Communications*, vol. 327, pp. 49–55, 2014.
- [56] C. Abellan, W. Amaya, D. Domenech, P. Muñoz, J. Capmany, S. Longhi, M. W. Mitchell, and V. Pruneri, “Quantum entropy source on an inp photonic integrated circuit for random number generation,” *Optica*, vol. 3, no. 9, pp. 989–994, 2016.
- [57] P. Sibson, C. Erven, M. Godfrey, S. Miki, T. Yamashita, M. Fujiwara, M. Sasaki, H. Terai, M. G. Tanner, C. M. Natarajan, *et al.*, “Chip-based quantum key distribution,” *Nature communications*, vol. 8, no. 1, pp. 1–6, 2017.
- [58] M. Kues, C. Reimer, P. Roztock, L. R. Cortés, S. Sciara, B. Wetzels, Y. Zhang, A. Cino, S. T. Chu, B. E. Little, *et al.*, “On-chip generation of high-dimensional entangled quantum states and their coherent control,” *Nature*, vol. 546, no. 7660, pp. 622–626, 2017.

- [59] C. Reimer, M. Kues, P. Roztock, B. Wetz, F. Grazioso, B. E. Little, S. T. Chu, T. Johnston, Y. Bromberg, L. Caspani, *et al.*, “Generation of multiphoton entangled quantum states by means of integrated frequency combs,” *Science*, vol. 351, no. 6278, pp. 1176–1180, 2016.
- [60] C. L. Degen, F. Reinhard, and P. Cappellaro, “Quantum sensing,” *Reviews of modern physics*, vol. 89, no. 3, p. 035 002, 2017.
- [61] T. Wolf, P. Neumann, K. Nakamura, H. Sumiya, T. Ohshima, J. Isoya, and J. Wrachtrup, “Subpicotesla diamond magnetometry,” *Physical Review X*, vol. 5, no. 4, p. 041 001, 2015.
- [62] M. Metcalfe, “Applications of cavity optomechanics,” *Applied Physics Reviews*, vol. 1, no. 3, p. 031 105, 2014.
- [63] T. Liu, F. Pagliano, R. van Veldhoven, V. Pogoretskiy, Y. Jiao, and A. Fiore, “Integrated nano-optomechanical displacement sensor with ultrawide optical bandwidth,” *Nature communications*, vol. 11, no. 1, pp. 1–7, 2020.
- [64] C. Reinhardt, T. Müller, A. Bourassa, and J. C. Sankey, “Ultralow-noise sin trampoline resonators for sensing and optomechanics,” *Physical Review X*, vol. 6, no. 2, p. 021 001, 2016.
- [65] A. D. O’Connell, M. Hofheinz, M. Ansmann, R. C. Bialczak, M. Lenander, E. Lucero, M. Neeley, D. Sank, H. Wang, M. Weides, *et al.*, “Quantum ground state and single-phonon control of a mechanical resonator,” *Nature*, vol. 464, no. 7289, pp. 697–703, 2010.
- [66] J. Guo, R. Norte, and S. Gröblacher, “Feedback cooling of a room temperature mechanical oscillator close to its motional ground state,” *Physical review letters*, vol. 123, no. 22, p. 223 602, 2019.
- [67] D. E. Chang, C. Regal, S. Papp, D. Wilson, J. Ye, O. Painter, H. J. Kimble, and P. Zoller, “Cavity opto-mechanics using an optically levitated nanosphere,” *Proceedings of the National Academy of Sciences*, vol. 107, no. 3, pp. 1005–1010, 2010.
- [68] U. Delić, M. Reisenbauer, K. Dare, D. Grass, V. Vuletić, N. Kiesel, and M. Aspelmeyer, “Cooling of a levitated nanoparticle to the motional quantum ground state,” *Science*, vol. 367, no. 6480, pp. 892–895, 2020.
- [69] A. Arvanitaki and A. A. Geraci, “Detecting high-frequency gravitational waves with optically levitated sensors,” *Physical review letters*, vol. 110, no. 7, p. 071 105, 2013.
- [70] A. Vinante, A. Pontin, M. Rashid, M. Toroš, P. Barker, and H. Ulbricht, “Testing collapse models with levitated nanoparticles: Detection challenge,” *Physical Review A*, vol. 100, no. 1, p. 012 119, 2019.

- [71] P. Huillery, T. Delord, L. Nicolas, M. Van Den Bossche, M. Perdriat, and G. Hetet, “Spin mechanics with levitating ferromagnetic particles,” *Physical Review B*, vol. 101, no. 13, p. 134 415, 2020.
- [72] W. Paul, “Electromagnetic traps for charged and neutral particles,” *Reviews of modern physics*, vol. 62, no. 3, p. 531, 1990.
- [73] O. Romero-Isart, L. Clemente, C. Navau, A. Sanchez, and J. Cirac, “Quantum magnetomechanics with levitating superconducting microspheres,” *Physical review letters*, vol. 109, no. 14, p. 147 205, 2012.
- [74] M. Cirio, G. Brennen, and J. Twamley, “Quantum magnetomechanics: Ultrahigh-q-levitated mechanical oscillators,” *Physical review letters*, vol. 109, no. 14, p. 147 206, 2012.
- [75] A. Vinante, P. Falferi, G. Gasbarri, A. Setter, C. Timberlake, and H. Ulbricht, “Ultralow mechanical damping with meissner-levitated ferromagnetic microparticles,” *Physical Review Applied*, vol. 13, no. 6, p. 064 027, 2020.
- [76] J. Gieseler, A. Kabcenell, E. Rosenfeld, J. Schaefer, A. Safira, M. J. Schuetz, C. Gonzalez-Ballester, C. C. Rusconi, O. Romero-Isart, and M. D. Lukin, “Single-spin magnetomechanics with levitated micromagnets,” *Physical review letters*, vol. 124, no. 16, p. 163 604, 2020.
- [77] D. F. J. Kimball, A. O. Sushkov, and D. Budker, “Precessing ferromagnetic needle magnetometer,” *Physical review letters*, vol. 116, no. 19, p. 190 801, 2016.
- [78] Y. Band, Y. Avishai, and A. Shnirman, “Dynamics of a magnetic needle magnetometer: Sensitivity to landau-lifshitz-gilbert damping,” *Physical review letters*, vol. 121, no. 16, p. 160 801, 2018.
- [79] S. Beresnev, V. Chernyak, and G. Fomyagin, “Motion of a spherical particle in a rarefied gas. part 2. drag and thermal polarization,” *Journal of Fluid Mechanics*, vol. 219, pp. 405–421, 1990.
- [80] Z. Ze-Bing, L. Jun, Y. Qin, Z. Yuan-Zhong, and N. Yu-Xin, “Seismic noise effect on equivalence principle test using free-fall interferometry,” *Chinese Physics Letters*, vol. 18, no. 1, p. 10, 2001.
- [81] A. A. Kordyuk, “Magnetic levitation for hard superconductors,” *Journal of Applied Physics*, vol. 83, no. 1, pp. 610–612, 1998.
- [82] J. R. Hull and A. Cansiz, “Vertical and lateral forces between a permanent magnet and a high-temperature superconductor,” *Journal of Applied Physics*, vol. 86, no. 11, pp. 6396–6404, 1999.

- [83] T. Sugiura, T. Aoyagi, H. Ura, and M. Yoshizawa, “Parametrically excited horizontal and rolling motion of a levitated body above a high- $T_c$ /superconductor,” *IEEE transactions on applied superconductivity*, vol. 13, no. 2, pp. 2247–2250, 2003.
- [84] L. Wang, Z. Deng, Y. Li, and H. Li, “Vertical–lateral coupling force relation of the high-temperature superconducting magnetic levitation system,” *IEEE Transactions on Applied Superconductivity*, vol. 31, no. 1, pp. 1–6, 2020.
- [85] F. Moon, M. Yanoviak, and R. Ware, “Hysteretic levitation forces in superconducting ceramics,” *Applied Physics Letters*, vol. 52, no. 18, pp. 1534–1536, 1988.
- [86] T. Hikihara and F. C. Moon, “Levitation drift of a magnet supported by a high- $T_c$  superconductor under vibration,” *Physica C: Superconductivity*, vol. 250, no. 1-2, pp. 121–127, 1995.
- [87] C. P. Bean, “Magnetization of high-field superconductors,” *Reviews of modern physics*, vol. 36, no. 1, p. 31, 1964.
- [88] J. Druge, C. Jean, O. Laurent, M.-A. Méasson, and I. Favero, “Damping and non-linearity of a levitating magnet in rotation above a superconductor,” *New Journal of Physics*, vol. 16, no. 7, p. 075 011, 2014.
- [89] T. Matsushita *et al.*, *Flux pinning in superconductors*. Springer, 2007, vol. 164.
- [90] F. Irie and K. Yamafuji, “Theory of flux motion in non-ideal type-II superconductors,” *Journal of the Physical Society of Japan*, vol. 23, no. 2, pp. 255–268, 1967.
- [91] X. Jiang, D. Pak, A. Nandi, Y. Xuan, and M. Hosseini, “Rare earth-implanted lithium niobate: Properties and on-chip integration,” *Applied Physics Letters*, vol. 115, no. 7, p. 071 104, 2019.
- [92] M. Kues, C. Reimer, J. M. Lukens, W. J. Munro, A. M. Weiner, D. J. Moss, and R. Morandotti, “Quantum optical microcombs,” *Nature Photonics*, vol. 13, no. 3, pp. 170–179, 2019.
- [93] B. Lauritzen, J. Minář, H. De Riedmatten, M. Afzelius, N. Sangouard, C. Simon, and N. Gisin, “Telecommunication-wavelength solid-state memory at the single photon level,” *Physical review letters*, vol. 104, no. 8, p. 080 502, 2010.
- [94] M. Rančić, M. P. Hedges, R. L. Ahlefeldt, and M. J. Sellars, “Coherence time of over a second in a telecom-compatible quantum memory storage material,” *Nature Physics*, vol. 14, no. 1, pp. 50–54, 2018.

- [95] C. Simon, H. De Riedmatten, M. Afzelius, N. Sangouard, H. Zbinden, and N. Gisin, “Quantum repeaters with photon pair sources and multimode memories,” *Physical review letters*, vol. 98, no. 19, p. 190 503, 2007.
- [96] J. H. Wesenberg, K. Mølmer, L. Rippe, and S. Kröll, “Scalable designs for quantum computing with rare-earth-ion-doped crystals,” *Physical Review A*, vol. 75, no. 1, p. 012 304, 2007.
- [97] C. Thiel, T. Böttger, and R. Cone, “Rare-earth-doped materials for applications in quantum information storage and signal processing,” *Journal of luminescence*, vol. 131, no. 3, pp. 353–361, 2011.
- [98] N. Gisin and R. Thew, “Quantum communication,” *Nature photonics*, vol. 1, no. 3, pp. 165–171, 2007.
- [99] M. Zhong, M. P. Hedges, R. L. Ahlefeldt, J. G. Bartholomew, S. E. Beavan, S. M. Wittig, J. J. Longdell, and M. J. Sellars, “Optically addressable nuclear spins in a solid with a six-hour coherence time,” *Nature*, vol. 517, no. 7533, pp. 177–180, 2015.
- [100] M. P. Hedges, J. J. Longdell, Y. Li, and M. J. Sellars, “Efficient quantum memory for light,” *Nature*, vol. 465, no. 7301, pp. 1052–1056, 2010.
- [101] T. Zhong, J. M. Kindem, J. Rochman, and A. Faraon, “Interfacing broadband photonic qubits to on-chip cavity-protected rare-earth ensembles,” *Nature communications*, vol. 8, no. 1, pp. 1–7, 2017.
- [102] E. Saglamyurek, M. G. Puigibert, Q. Zhou, L. Giner, F. Marsili, V. B. Verma, S. W. Nam, L. Oesterling, D. Nippa, D. Oblak, *et al.*, “A multiplexed light-matter interface for fibre-based quantum networks,” *Nature communications*, vol. 7, no. 1, pp. 1–7, 2016.
- [103] O. Collins, S. Jenkins, A. Kuzmich, and T. Kennedy, “Multiplexed memory-insensitive quantum repeaters,” *Physical review letters*, vol. 98, no. 6, p. 060 502, 2007.
- [104] A. Dibos, M. Raha, C. Phenicie, and J. D. Thompson, “Atomic source of single photons in the telecom band,” *Physical review letters*, vol. 120, no. 24, p. 243 601, 2018.
- [105] G. Poberaj, H. Hu, W. Sohler, and P. Guenter, “Lithium niobate on insulator (lnoi) for micro-photonic devices,” *Laser & photonics reviews*, vol. 6, no. 4, pp. 488–503, 2012.
- [106] P. Rabiei, J. Ma, S. Khan, J. Chiles, and S. Fathpour, “Heterogeneous lithium niobate photonics on silicon substrates,” *Optics express*, vol. 21, no. 21, pp. 25 573–25 581, 2013.
- [107] C. Wang, M. Zhang, B. Stern, M. Lipson, and M. Lončar, “Nanophotonic lithium niobate electro-optic modulators,” *Optics express*, vol. 26, no. 2, pp. 1547–1555, 2018.



- [108] C. Thiel, Y. Sun, R. Macfarlane, T. Böttger, and R. Cone, “Rare-earth-doped linbo3 and ktiopo4 (ktp) for waveguide quantum memories,” *Journal of Physics B: Atomic, Molecular and Optical Physics*, vol. 45, no. 12, p. 124 013, 2012.
- [109] N. Sinclair, K. Heshami, C. Deshmukh, D. Oblak, C. Simon, and W. Tittel, “Proposal and proof-of-principle demonstration of non-destructive detection of photonic qubits using a tm: Linbo 3 waveguide,” *Nature communications*, vol. 7, no. 1, pp. 1–6, 2016.
- [110] T. Kornher, K. Xia, R. Kolesov, N. Kukharchyk, R. Reuter, P. Siyushev, R. Stöhr, M. Schreck, H.-W. Becker, B. Villa, *et al.*, “Production yield of rare-earth ions implanted into an optical crystal,” *Applied Physics Letters*, vol. 108, no. 5, p. 053 108, 2016.
- [111] K. Sweeney and L. Halliburton, “Oxygen vacancies in lithium niobate,” *Applied physics letters*, vol. 43, no. 4, pp. 336–338, 1983.
- [112] J. Ketchum, K. Sweeney, L. Halliburton, and A. Armington, “Vacuum annealing effects in lithium niobate,” *Physics Letters A*, vol. 94, no. 9, pp. 450–453, 1983.
- [113] Y. Xuan, Y. Liu, L. T. Varghese, A. J. Metcalf, X. Xue, P.-H. Wang, K. Han, J. A. Jaramillo-Villegas, A. Al Noman, C. Wang, *et al.*, “High-q silicon nitride microresonators exhibiting low-power frequency comb initiation,” *Optica*, vol. 3, no. 11, pp. 1171–1180, 2016.
- [114] J. Wang, Y. Xuan, C. Lee, B. Niu, L. Liu, G. N. Liu, and M. Qi, “Low-loss and misalignment-tolerant fiber-to-chip edge coupler based on double-tip inverse tapers,” in *2016 Optical Fiber Communications Conference and Exhibition (OFC)*, IEEE, 2016, pp. 1–3.
- [115] A. Namba, M. Sugimoto, T. Ogura, Y. Tomita, and K. Eda, “Direct bonding of piezo-electric crystal onto silicon,” *Applied physics letters*, vol. 67, no. 22, pp. 3275–3276, 1995.
- [116] D. Tulli, D. Janner, and V. Pruneri, “Room temperature direct bonding of linbo3 crystal layers and its application to high-voltage optical sensing,” *Journal of Micromechanics and Microengineering*, vol. 21, no. 8, p. 085 025, 2011.
- [117] A. Arnaud, D. Forsyth, T. Sun, Z. Zhang, and K. Grattan, “Strain and temperature effects on erbium-doped fiber for decay-time based sensing,” *Review of Scientific Instruments*, vol. 71, no. 1, pp. 104–108, 2000.
- [118] S. A. Wade, D. I. Forsyth, K. T. Grattan, and Q. Guofu, “Fiber optic sensor for dual measurement of temperature and strain using a combined fluorescence lifetime decay and fiber bragg grating technique,” *Review of Scientific Instruments*, vol. 72, no. 8, pp. 3186–3190, 2001.
- [119] M. Howlader, T. Suga, and M. Kim, “Room temperature bonding of silicon and lithium niobate,” *Applied physics letters*, vol. 89, no. 3, p. 031 914, 2006.

- [120] D. Gill, L. McCaughan, and J. Wright, “Spectroscopic site determinations in erbium-doped lithium niobate,” *Physical Review B*, vol. 53, no. 5, p. 2334, 1996.
- [121] N. M. Arslanov and S. A. Moiseev, “Optimal periodic frequency combs for high-efficiency optical quantum memory based on rare-earth ion crystals,” *Quantum Electronics*, vol. 47, no. 9, p. 783, 2017.
- [122] A. Nandi, X. Jiang, D. Pak, D. Perry, K. Han, E. S. Bielejec, Y. Xuan, and M. Hosseini, “Controlling light emission by engineering atomic geometries in silicon photonics,” *Optics letters*, vol. 45, no. 7, pp. 1631–1634, 2020.
- [123] M. M. Minnegaliev, E. I. Baibekov, K. I. Gerasimov, S. A. Moiseev, M. A. Smirnov, and R. Urmancheev, “Photon echo of an ultranarrow optical transition of  $167\text{Er}^{3+}$  in  $7\text{LiYF}_4$  crystals,” *Quantum Electronics*, vol. 47, no. 9, p. 778, 2017.
- [124] A. Naik, O. Buu, M. LaHaye, A. Armour, A. Clerk, M. Blencowe, and K. Schwab, “Cooling a nanomechanical resonator with quantum back-action,” *Nature*, vol. 443, no. 7108, pp. 193–196, 2006.
- [125] A. H. Safavi-Naeini, S. Gröblacher, J. T. Hill, J. Chan, M. Aspelmeyer, and O. Painter, “Squeezed light from a silicon micromechanical resonator,” *Nature*, vol. 500, no. 7461, pp. 185–189, 2013.
- [126] R. Riedinger, A. Wallucks, I. Marinković, C. Löschnauer, M. Aspelmeyer, S. Hong, and S. Gröblacher, “Remote quantum entanglement between two micromechanical oscillators,” *Nature*, vol. 556, no. 7702, pp. 473–477, 2018.
- [127] V. Giovannetti, S. Mancini, and P. Tombesi, “Radiation pressure induced einstein-podolsky-rosen paradox,” *EPL (Europhysics Letters)*, vol. 54, no. 5, p. 559, 2001.
- [128] G. Heinrich, M. Ludwig, J. Qian, B. Kubala, and F. Marquardt, “Collective dynamics in optomechanical arrays,” *Physical review letters*, vol. 107, no. 4, p. 043 603, 2011.
- [129] D. Chang, A. H. Safavi-Naeini, M. Hafezi, and O. Painter, “Slowing and stopping light using an optomechanical crystal array,” *New Journal of Physics*, vol. 13, no. 2, p. 023 003, 2011.
- [130] A. H. Safavi-Naeini and O. Painter, “Design of optomechanical cavities and waveguides on a simultaneous bandgap phononic-photonic crystal slab,” *Optics express*, vol. 18, no. 14, pp. 14 926–14 943, 2010.
- [131] E. Gavartin, P. Verlot, and T. J. Kippenberg, “A hybrid on-chip optomechanical transducer for ultrasensitive force measurements,” *Nature nanotechnology*, vol. 7, no. 8, pp. 509–514, 2012.

- [132] A. G. Krause, M. Winger, T. D. Blasius, Q. Lin, and O. Painter, “A high-resolution microchip optomechanical accelerometer,” *Nature Photonics*, vol. 6, no. 11, pp. 768–772, 2012.
- [133] S. Nimmrichter, K. Hornberger, and K. Hammerer, “Optomechanical sensing of spontaneous wave-function collapse,” *Physical review letters*, vol. 113, no. 2, p. 020 405, 2014.
- [134] M. Ludwig and F. Marquardt, “Quantum many-body dynamics in optomechanical arrays,” *Physical review letters*, vol. 111, no. 7, p. 073 603, 2013.
- [135] A. Xuereb, C. Genes, G. Pupillo, M. Paternostro, and A. Dantan, “Reconfigurable long-range phonon dynamics in optomechanical arrays,” *Physical review letters*, vol. 112, no. 13, p. 133 604, 2014.
- [136] L.-L. Wan, X.-Y. Lü, J.-H. Gao, and Y. Wu, “Controllable photon and phonon localization in optomechanical lieb lattices,” *Optics express*, vol. 25, no. 15, pp. 17 364–17 374, 2017.
- [137] J. Chan, T. M. Alegre, A. H. Safavi-Naeini, J. T. Hill, A. Krause, S. Gröblacher, M. Aspelmeyer, and O. Painter, “Laser cooling of a nanomechanical oscillator into its quantum ground state,” *Nature*, vol. 478, no. 7367, pp. 89–92, 2011.
- [138] S. Weis, R. Rivière, S. Deléglise, E. Gavartin, O. Arcizet, A. Schliesser, and T. J. Kippenberg, “Optomechanically induced transparency,” *Science*, vol. 330, no. 6010, pp. 1520–1523, 2010.
- [139] F. Monifi, J. Zhang, Ş. K. Özdemir, B. Peng, Y.-x. Liu, F. Bo, F. Nori, and L. Yang, “Optomechanically induced stochastic resonance and chaos transfer between optical fields,” *nature photonics*, vol. 10, no. 6, pp. 399–405, 2016.
- [140] A. H. Safavi-Naeini, T. M. Alegre, J. Chan, M. Eichenfield, M. Winger, Q. Lin, J. T. Hill, D. E. Chang, and O. Painter, “Electromagnetically induced transparency and slow light with optomechanics,” *Nature*, vol. 472, no. 7341, pp. 69–73, 2011.
- [141] S. Mancini and P. Tombesi, “Quantum noise reduction by radiation pressure,” *Physical Review A*, vol. 49, no. 5, p. 4055, 1994.
- [142] C. Fabre, M. Pinard, S. Bourzeix, A. Heidmann, E. Giacobino, and S. Reynaud, “Quantum-noise reduction using a cavity with a movable mirror,” *Physical Review A*, vol. 49, no. 2, p. 1337, 1994.
- [143] D. W. Brooks, T. Botter, S. Schreppler, T. P. Purdy, N. Brahms, and D. M. Stamper-Kurn, “Non-classical light generated by quantum-noise-driven cavity optomechanics,” *Nature*, vol. 488, no. 7412, pp. 476–480, 2012.

- [144] E. Gil-Santos, C. Baker, A. Lemaître, S. Ducci, C. Gomez, G. Leo, and I. Favero, “Scalable high-precision tuning of photonic resonators by resonant cavity-enhanced photo-electrochemical etching,” *Nature communications*, vol. 8, no. 1, pp. 1–7, 2017.
- [145] S.-B. Shim, M. Imboden, and P. Mohanty, “Synchronized oscillation in coupled nanomechanical oscillators,” *science*, vol. 316, no. 5821, pp. 95–99, 2007.
- [146] M. Zhang, G. S. Wiederhecker, S. Manipatruni, A. Barnard, P. McEuen, and M. Lipson, “Synchronization of micromechanical oscillators using light,” *Physical review letters*, vol. 109, no. 23, p. 233 906, 2012.
- [147] A. H. Safavi-Naeini, J. T. Hill, S. Meenehan, J. Chan, S. Gröblacher, and O. Painter, “Two-dimensional phononic-photonic band gap optomechanical crystal cavity,” *Physical Review Letters*, vol. 112, no. 15, p. 153 603, 2014.
- [148] J. A. Acebrón, L. L. Bonilla, C. J. P. Vicente, F. Ritort, and R. Spigler, “The kuramoto model: A simple paradigm for synchronization phenomena,” *Reviews of modern physics*, vol. 77, no. 1, p. 137, 2005.
- [149] E. Amitai, N. Lörch, A. Nunnenkamp, S. Walter, and C. Bruder, “Synchronization of an optomechanical system to an external drive,” *Physical Review A*, vol. 95, no. 5, p. 053 858, 2017.
- [150] M. Zhang, S. Shah, J. Cardenas, and M. Lipson, “Synchronization and phase noise reduction in micromechanical oscillator arrays coupled through light,” *Physical review letters*, vol. 115, no. 16, p. 163 902, 2015.
- [151] E. Moiseev and S. Moiseev, “All-optical photon echo on a chip,” *Laser Physics Letters*, vol. 14, no. 1, p. 015 202, 2016.
- [152] M. Hosseini, B. M. Sparkes, G. Hétet, J. J. Longdell, P. K. Lam, and B. C. Buchler, “Coherent optical pulse sequencer for quantum applications,” *Nature*, vol. 461, no. 7261, pp. 241–245, 2009.
- [153] H. Trommsdorff, A. Corval, and L. Von Laue, “Spectral hole burning: Spontaneous and photoinduced tunneling reactions in low temperature solids,” *Pure and applied chemistry*, vol. 67, no. 1, pp. 191–198, 1995.
- [154] E. Saglamyurek, J. Jin, V. B. Verma, M. D. Shaw, F. Marsili, S. W. Nam, D. Oblak, and W. Tittel, “Quantum storage of entangled telecom-wavelength photons in an erbium-doped optical fibre,” *Nature Photonics*, vol. 9, no. 2, pp. 83–87, 2015.

- [155] C. Clausen, I. Usmani, F. Bussieres, N. Sangouard, M. Afzelius, H. de Riedmatten, and N. Gisin, “Quantum storage of photonic entanglement in a crystal,” *Nature*, vol. 469, no. 7331, pp. 508–511, 2011.
- [156] T. Li and F.-G. Deng, “Heralded high-efficiency quantum repeater with atomic ensembles assisted by faithful single-photon transmission,” *Scientific reports*, vol. 5, no. 1, pp. 1–14, 2015.
- [157] G. Campbell, A. Ordog, and A. Lvovsky, “Multimode electromagnetically induced transparency on a single atomic line,” *New Journal of Physics*, vol. 11, no. 10, p. 103 021, 2009.
- [158] M. Schmidt, M. Ludwig, and F. Marquardt, “Optomechanical circuits for nanomechanical continuous variable quantum state processing,” *New Journal of Physics*, vol. 14, no. 12, p. 125 005, 2012.
- [159] C. Gardiner, P. Zoller, and P. Zoller, *Quantum noise: a handbook of Markovian and non-Markovian quantum stochastic methods with applications to quantum optics*. Springer Science & Business Media, 2004.
- [160] M. Afzelius and C. Simon, “Impedance-matched cavity quantum memory,” *Physical Review A*, vol. 82, no. 2, p. 022 310, 2010.
- [161] G. Collecute and P. D. Drummond, “Xmds: Extensible multi-dimensional simulator,” *Computer physics communications*, vol. 142, no. 1-3, pp. 219–223, 2001.
- [162] M. Eichenfield, R. Camacho, J. Chan, K. J. Vahala, and O. Painter, “A picogram-and nanometre-scale photonic-crystal optomechanical cavity,” *nature*, vol. 459, no. 7246, pp. 550–555, 2009.
- [163] T. Purdy, K. Grutter, K. Srinivasan, and J. Taylor, “Quantum correlations from a room-temperature optomechanical cavity,” *Science*, vol. 356, no. 6344, pp. 1265–1268, 2017.
- [164] M. Li, W. Pernice, and H. Tang, “Ultrahigh-frequency nano-optomechanical resonators in slot waveguide ring cavities,” *Applied Physics Letters*, vol. 97, no. 18, p. 183 110, 2010.
- [165] X. Jiang, J. Rudge, and M. Hosseini, “Superconducting levitation of a mg-scale cavity mirror,” *Applied Physics Letters*, vol. 116, no. 24, p. 244 103, 2020.
- [166] M. Aspelmeyer, T. J. Kippenberg, and F. Marquardt, “Cavity optomechanics,” *Reviews of Modern Physics*, vol. 86, no. 4, p. 1391, 2014.
- [167] M. Rashid, M. Toroš, A. Setter, and H. Ulbricht, “Precession motion in levitated optomechanics,” *Physical review letters*, vol. 121, no. 25, p. 253 601, 2018.

- [168] J. Ahn, Z. Xu, J. Bang, P. Ju, X. Gao, and T. Li, “Ultrasensitive torque detection with an optically levitated nanorotor,” *Nature nanotechnology*, vol. 15, no. 2, pp. 89–93, 2020.
- [169] L. P. Neukirch, E. Von Haartman, J. M. Rosenholm, and A. N. Vamivakas, “Multi-dimensional single-spin nano-optomechanics with a levitated nanodiamond,” *Nature Photonics*, vol. 9, no. 10, pp. 653–657, 2015.
- [170] A. Noguchi, Y. Shikano, K. Toyoda, and S. Urabe, “Aharonov–bohm effect in the tunnelling of a quantum rotor in a linear paul trap,” *Nature communications*, vol. 5, no. 1, pp. 1–6, 2014.
- [171] T. Ostermayr, J. Gebhard, D. Haffa, D. Kiefer, C. Kreuzer, K. Allinger, C. Bömer, J. Braenzel, M. Schnürer, I. Cermak, *et al.*, “A transportable paul-trap for levitation and accurate positioning of micron-scale particles in vacuum for laser-plasma experiments,” *Review of Scientific Instruments*, vol. 89, no. 1, p. 013302, 2018.
- [172] T. Wang, S. Lourette, S. R. O’Kelley, M. Kayci, Y. Band, D. F. J. Kimball, A. O. Sushkov, and D. Budker, “Dynamics of a ferromagnetic particle levitated over a superconductor,” *Physical Review Applied*, vol. 11, no. 4, p. 044041, 2019.
- [173] G. Guccione, M. Hosseini, S. Adlong, M. Johnsson, J. Hope, B. Buchler, and P. K. Lam, “Scattering-free optical levitation of a cavity mirror,” *Physical review letters*, vol. 111, no. 18, p. 183001, 2013.
- [174] H. Pino, J. Prat-Camps, K. Sinha, B. P. Venkatesh, and O. Romero-Isart, “On-chip quantum interference of a superconducting microsphere,” *Quantum Science and Technology*, vol. 3, no. 2, p. 025001, 2018.
- [175] J. Gieseler, L. Novotny, and R. Quidant, “Thermal nonlinearities in a nanomechanical oscillator,” *Nature physics*, vol. 9, no. 12, pp. 806–810, 2013.
- [176] A. Cansiz, “Correlation between free oscillation frequency and stiffness in high temperature superconducting bearings,” *Physica C: Superconductivity*, vol. 390, no. 4, pp. 356–362, 2003.
- [177] S. Ran, “Gravity probe b: Exploring einstein’s universe with gyroscopes,” *NASA*, p. 26, 2004.
- [178] J. Kitching, “Chip-scale atomic devices,” *Applied Physics Reviews*, vol. 5, no. 3, p. 031302, 2018.
- [179] S. Seltzer and M. Romalis, “Unshielded three-axis vector operation of a spin-exchange-relaxation-free atomic magnetometer,” *Applied physics letters*, vol. 85, no. 20, pp. 4804–4806, 2004.

- [180] F. Niekiet, J. Su, M. T. Bodduluri, T. Lisec, L. Blohm, I. Pieper, B. Wagner, and F. Lofink, “Highly sensitive mems magnetic field sensors with integrated powder-based permanent magnets,” *Sensors and Actuators A: Physical*, vol. 297, p. 111 560, 2019.
- [181] J. F. Barry, J. M. Schloss, E. Bauch, M. J. Turner, C. A. Hart, L. M. Pham, and R. L. Walsworth, “Sensitivity optimization for nv-diamond magnetometry,” *Reviews of Modern Physics*, vol. 92, no. 1, p. 015 004, 2020.
- [182] C. Zhang, H. Yuan, N. Zhang, L. Xu, J. Zhang, B. Li, and J. Fang, “Vector magnetometer based on synchronous manipulation of nitrogen-vacancy centers in all crystal directions,” *Journal of Physics D: Applied Physics*, vol. 51, no. 15, p. 155 102, 2018.
- [183] T. Corbitt, D. Ottaway, E. Innerhofer, J. Pelc, and N. Mavalvala, “Measurement of radiation-pressure-induced optomechanical dynamics in a suspended fabry-perot cavity,” *Physical Review A*, vol. 74, no. 2, p. 021 802, 2006.
- [184] B. S. Sheard, M. B. Gray, C. M. Mow-Lowry, D. E. McClelland, and S. E. Whitcomb, “Observation and characterization of an optical spring,” *Physical Review A*, vol. 69, no. 5, p. 051 801, 2004.
- [185] D. E. Chang, K. Ni, O. Painter, and H. J. Kimble, “Ultrahigh-q mechanical oscillators through optical trapping,” *New Journal of Physics*, vol. 14, no. 4, p. 045 002, 2012.
- [186] C. Bekker, R. Kalra, C. Baker, and W. P. Bowen, “Injection locking of an electro-optomechanical device,” *Optica*, vol. 4, no. 10, pp. 1196–1204, 2017.
- [187] T. Corbitt, Y. Chen, E. Innerhofer, H. Müller-Ebhardt, D. Ottaway, H. Rehbein, D. Sigg, S. Whitcomb, C. Wipf, and N. Mavalvala, “An all-optical trap for a gram-scale mirror,” *Physical review letters*, vol. 98, no. 15, p. 150 802, 2007.
- [188] C. Yu, J. Janousek, E. Sheridan, D. L. McAuslan, H. Rubinsztein-Dunlop, P. K. Lam, Y. Zhang, and W. P. Bowen, “Optomechanical magnetometry with a macroscopic resonator,” *Physical Review Applied*, vol. 5, no. 4, p. 044 007, 2016.
- [189] B.-B. Li, G. Brawley, H. Greenall, S. Forstner, E. Sheridan, H. Rubinsztein-Dunlop, and W. P. Bowen, “Ultrabroadband and sensitive cavity optomechanical magnetometry,” *Photonics Research*, vol. 8, no. 7, pp. 1064–1071, 2020.
- [190] B.-B. Li, J. Bilek, U. B. Hoff, L. S. Madsen, S. Forstner, V. Prakash, C. Schäfermeier, T. Gehring, W. P. Bowen, and U. L. Andersen, “Quantum enhanced optomechanical magnetometry,” *Optica*, vol. 5, no. 7, pp. 850–856, 2018.

- [191] C. Gan, C. Savage, and S. Scully, “Optomechanical tests of a schrödinger-newton equation for gravitational quantum mechanics,” *Physical Review D*, vol. 93, no. 12, p. 124 049, 2016.
- [192] H. Yang, H. Miao, D.-S. Lee, B. Helou, and Y. Chen, “Macroscopic quantum mechanics in a classical spacetime,” *Physical review letters*, vol. 110, no. 17, p. 170 401, 2013.
- [193] H. Miao, S. Danilishin, T. Corbitt, and Y. Chen, “Standard quantum limit for probing mechanical energy quantization,” *Physical review letters*, vol. 103, no. 10, p. 100 402, 2009.
- [194] B. Abbott, R. Abbott, R. Adhikari, P. Ajith, B. Allen, G. Allen, R. Amin, S. Anderson, W. Anderson, M. Arain, *et al.*, “Observation of a kilogram-scale oscillator near its quantum ground state,” *New Journal of Physics*, vol. 11, no. 7, p. 073 032, 2009.
- [195] A. D. Rider, D. C. Moore, C. P. Blakemore, M. Louis, M. Lu, and G. Gratta, “Search for screened interactions associated with dark energy below the 100  $\mu$  m length scale,” *Physical review letters*, vol. 117, no. 10, p. 101 101, 2016.
- [196] C. P. Blakemore, A. D. Rider, S. Roy, A. Fieguth, A. Kawasaki, N. Priel, and G. Gratta, “Precision mass and density measurement of individual optically levitated microspheres,” *Physical Review Applied*, vol. 12, no. 2, p. 024 037, 2019.
- [197] X. Jiang and M. Hosseini, “Driven nonlinear damping and mode coupling in a superconducting levitated magnet,” *Physical Review Research*, vol. 4, no. 1, p. 013 132, 2022.
- [198] C. Gonzalez-Ballester, M. Aspelmeyer, L. Novotny, R. Quidant, and O. Romero-Isart, “Levitodynamics: Levitation and control of microscopic objects in vacuum,” *Science*, vol. 374, no. 6564, eabg3027, 2021.
- [199] G. S. MacCabe, H. Ren, J. Luo, J. D. Cohen, H. Zhou, A. Sipahigil, M. Mirhosseini, and O. Painter, “Nano-acoustic resonator with ultralong phonon lifetime,” *Science*, vol. 370, no. 6518, pp. 840–843, 2020.
- [200] A. Shkarin, A. Kashkanova, C. Brown, S. Garcia, K. Ott, J. Reichel, and J. Harris, “Quantum optomechanics in a liquid,” *Physical review letters*, vol. 122, no. 15, p. 153 601, 2019.
- [201] A. M. Kaufman, B. J. Lester, and C. A. Regal, “Cooling a single atom in an optical tweezer to its quantum ground state,” *Physical Review X*, vol. 2, no. 4, p. 041 014, 2012.
- [202] J. Hu, A. Urvoy, Z. Vendeiro, V. Crépel, W. Chen, and V. Vuletić, “Creation of a bose-condensed gas of 87rb by laser cooling,” *Science*, vol. 358, no. 6366, pp. 1078–1080, 2017.



- [203] K. Streltsov, J. S. Pedernales, and M. B. Plenio, “Ground-state cooling of levitated magnets in low-frequency traps,” *Physical Review Letters*, vol. 126, no. 19, p. 193 602, 2021.
- [204] T. Sugiura, T. Inoue, and H. Ura, “Nonlinear vibration of a coupled high- $t_c$  superconducting levitation system,” *Physica C: Superconductivity*, vol. 412, pp. 778–783, 2004.
- [205] L. M. Manojlović, “Quadrant photodetector sensitivity,” *Applied optics*, vol. 50, no. 20, pp. 3461–3469, 2011.
- [206] A. Peruzzo, J. McClean, P. Shadbolt, M.-H. Yung, X.-Q. Zhou, P. J. Love, A. Aspuru-Guzik, and J. L. O’Brien, “A variational eigenvalue solver on a photonic quantum processor,” *Nature communications*, vol. 5, no. 1, pp. 1–7, 2014.
- [207] T.-F. Lu *et al.*, “Analytical expression of the magnetic field created by a permanent magnet with diametrical magnetization,” *Progress In Electromagnetics Research C*, vol. 87, 2018.
- [208] C. Timberlake, A. Vinante, F. Shankar, A. Lapi, and H. Ulbricht, “Probing modified gravity with magnetically levitated resonators,” *Physical Review D*, vol. 104, no. 10, p. L101101, 2021.
- [209] D. B. Liarte, D. Hall, P. N. Koufalis, A. Miyazaki, A. Senanian, M. Liepe, and J. P. Sethna, “Vortex dynamics and losses due to pinning: Dissipation from trapped magnetic flux in resonant superconducting radio-frequency cavities,” *Physical Review Applied*, vol. 10, no. 5, p. 054 057, 2018.
- [210] T. Li, S. Kheifets, and M. G. Raizen, “Millikelvin cooling of an optically trapped microsphere in vacuum,” *Nature Physics*, vol. 7, no. 7, pp. 527–530, 2011.
- [211] A. Vinante, M. Bionotto, M. Bonaldi, M. Cerdonio, L. Conti, P. Falferi, N. Liguori, S. Longo, R. Mezzena, A. Ortolan, *et al.*, “Feedback cooling of the normal modes of a massive electromechanical system to submillikelvin temperature,” *Physical review letters*, vol. 101, no. 3, p. 033 601, 2008.
- [212] G. Guccione *et al.*, “Optomechanical enhancements for applications in metrology,” 2017.
- [213] V. Sokolovsky, V. Meerovich, M. Spektor, G. A. Levin, and I. Vajda, “Losses in superconductors under non-sinusoidal currents and magnetic fields,” *IEEE transactions on applied superconductivity*, vol. 19, no. 3, pp. 3344–3347, 2009.
- [214] M. Pinard, P.-F. Cohadon, T. Briant, and A. Heidmann, “Full mechanical characterization of a cold damped mirror,” *Physical Review A*, vol. 63, no. 1, p. 013 808, 2000.

- [215] F. Tebbenjohanns, M. L. Mattana, M. Rossi, M. Frimmer, and L. Novotny, “Quantum control of a nanoparticle optically levitated in cryogenic free space,” *arXiv preprint arXiv:2103.03853*, 2021.
- [216] J. Gieseler and J. Millen, “Levitated nanoparticles for microscopic thermodynamics—a review,” *Entropy*, vol. 20, no. 5, p. 326, 2018.
- [217] J. R. Maze, P. L. Stanwix, J. S. Hodges, S. Hong, J. M. Taylor, P. Cappellaro, L. Jiang, M. G. Dutt, E. Togan, A. Zibrov, *et al.*, “Nanoscale magnetic sensing with an individual electronic spin in diamond,” *Nature*, vol. 455, no. 7213, pp. 644–647, 2008.
- [218] B. L. Brown, A. J. Dicks, and I. A. Walmsley, “Coherent control of ultracold molecule dynamics in a magneto-optical trap by use of chirped femtosecond laser pulses,” *Physical review letters*, vol. 96, no. 17, p. 173 002, 2006.
- [219] H. Williams, L. Caldwell, N. Fitch, S. Truppe, J. Rodewald, E. Hinds, B. Sauer, and M. Tarbutt, “Magnetic trapping and coherent control of laser-cooled molecules,” *Physical review letters*, vol. 120, no. 16, p. 163 201, 2018.
- [220] J. Gieseler, B. Deutsch, R. Quidant, and L. Novotny, “Subkelvin parametric feedback cooling of a laser-trapped nanoparticle,” *Physical review letters*, vol. 109, no. 10, p. 103 603, 2012.
- [221] M. Hosseini, G. Guccione, H. J. Slatyer, B. C. Buchler, and P. K. Lam, “Multimode laser cooling and ultra-high sensitivity force sensing with nanowires,” *Nature communications*, vol. 5, no. 1, pp. 1–6, 2014.
- [222] B. P. Abbott, R. Abbott, T. Abbott, M. Abernathy, F. Acernese, K. Ackley, C. Adams, T. Adams, P. Addesso, R. Adhikari, *et al.*, “Observation of gravitational waves from a binary black hole merger,” *Physical review letters*, vol. 116, no. 6, p. 061 102, 2016.
- [223] J. Schmöle, M. Dragosits, H. Hepach, and M. Aspelmeyer, “A micromechanical proof-of-principle experiment for measuring the gravitational force of milligram masses,” *Classical and Quantum Gravity*, vol. 33, no. 12, p. 125 031, 2016.
- [224] R. C. Ritter, C. E. Goldblum, W.-T. Ni, G. T. Gillies, and C. C. Speake, “Experimental test of equivalence principle with polarized masses,” *Physical Review D*, vol. 42, no. 4, p. 977, 1990.
- [225] S. Kolkowitz, A. C. B. Jayich, Q. P. Unterreithmeier, S. D. Bennett, P. Rabl, J. Harris, and M. D. Lukin, “Coherent sensing of a mechanical resonator with a single-spin qubit,” *Science*, vol. 335, no. 6076, pp. 1603–1606, 2012.

- [226] T. P. Purdy, R. W. Peterson, and C. Regal, “Observation of radiation pressure shot noise on a macroscopic object,” *Science*, vol. 339, no. 6121, pp. 801–804, 2013.
- [227] A. A. Geraci, C. Bradley, D. Gao, J. Weinstein, and A. Derevianko, “Searching for ultralight dark matter with optical cavities,” *Physical review letters*, vol. 123, no. 3, p. 031 304, 2019.
- [228] N. Matsumoto, S. B. Cataño-Lopez, M. Sugawara, S. Suzuki, N. Abe, K. Komori, Y. Michimura, Y. Aso, and K. Edamatsu, “Demonstration of displacement sensing of a mg-scale pendulum for mm-and mg-scale gravity measurements,” *Physical review letters*, vol. 122, no. 7, p. 071 101, 2019.

## PUBLICATIONS

### Journal publications

1. **X. Jiang**, and M. Hosseini, “Driven nonlinear damping and mode coupling in a superconducting levitated magnet .”, Physical Review Research 4.1 (2022): 013132.
2. **X. Jiang**, J. Rudge, and M. Hosseini, “Superconducting levitation of a mg-scale cavity mirror.”, Applied Physics Letters 116.24 (2020): 244103.
3. **X. Jiang**, D. Pak, A. Nandi, Y. Xuan, and M. Hosseini, “Rare earth-implanted lithium niobate: Properties and on-chip integration.”, Applied Physics Letters 115.7 (2019): 071104.
4. **X. Jiang**, A. Nandi, D. Pak, and M. Hosseini, “Optomechanical frequency comb memory.”, Optics letters 43.20 (2018): 4973-4976.
5. A. Nandi, **X. Jiang**, D. Pak, D. Perry, K. Han, E. Bielejec, Y. Xuan, and M. Hosseini, “Controlling light emission by engineering atomic geometries in silicon photonics.”, Optics Letters 45.7 (2020): 1631-1.
6. D. Pak, H. An, A Nandi, **X. Jiang**, Y Xuan, M. Hosseini, “Ytterbium-implanted photonic resonators based on this thin film lithium niobate.”, Journal of Applied Physics, 128. 8 (2020): 084302.

### Conference proceedings

1. P. Dongmin, A. Haechan, **X. Jiang**, A. Nandi, Y. Xuan, M. Hosseini. ”Ytterbium implanted lithium niobate ring resonators on insulator: Fabrication and Characterization.” 2020 IEEE Photonics Conference (IPC). IEEE.
2. P. Dongmin, A. Nandi, **X. Jiang**, D. Perry, E. Bielejec, Y. Xuan, M. Hosseini. ”Integration of rare earth ions and photonic resonators for quantum application.” CLEO: QELS-Fundamental Science. Optical Society of America, 2020.